Physical, Chemical, & Biomolecular Sciences Center

Research Briefs

2004

Sandia National Laboratories
Albuquerque, New Mexico

A Multiprogram Laboratory

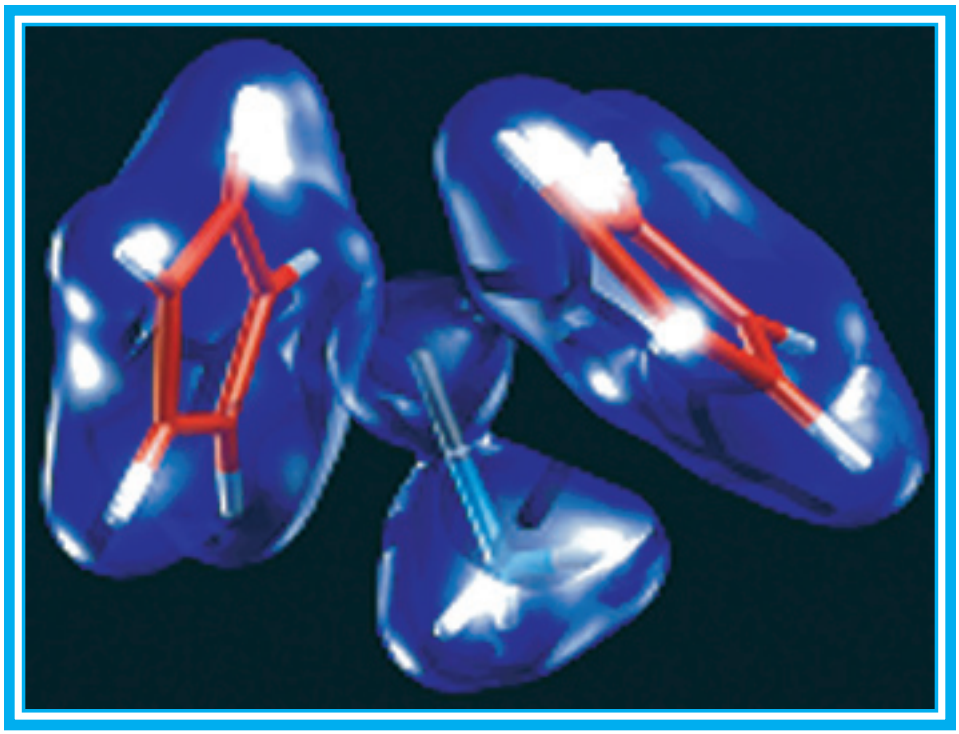

Research Briefs for the Physical, Chemical, & Biomolecular Sciences Center is published by Sandia National Laboratories, a multiprogram laboratory operated by Sandia Corporation, a Lockheed Martin Company, for the United States National Nuclear Security Administration and the Department of Energy under Contract DE-AC04-94AL85000.

Additional complimentary copies are available by contacting:

Julia M. Phillips
Physical, Chemical, & Biomolecular Sciences Center, 1100
Sandia National Laboratories
Albuquerque, NM 87185-1427

Phone: (505) 844-1071
Fax: (505) 844-6098
E-mail: jmphill@sandia.gov
url: http://www.sandia.gov/1100/index.htm

Research Briefs

Editors
J. M. Phillips
J. A. Nichelason

Production
M. Sheila Wilson

Cover Page: "Reversible Complex Formation between Ammonia and Magnesocene as Revealed by Density Functional Theory." See pages 44 & 45 for further details.

Message from the Director

The Physical, Chemical, & Biomolecular Sciences Center provides new scientific knowledge in support of Sandia's mission areas–nuclear weapons, energy and infrastructure assurance, nonproliferation and assessments, military technology and applications, and homeland security. We provide science-based solutions for the mission needs of our parent agency, the National Nuclear Security Administration (NNSA), particularly in areas where we have unique expertise. Of equal importance, we also perform focused long-term research in areas that are most likely to have impact on future Sandia missions and national security, particularly in the physical, chemical, and biological sciences that will enable future microsystems. To this end, we focus on six technical thrusts: optical sciences, nanosciences, compound semiconductors, biotechnology, collective hierarchical systems, and science-based solutions for NNSA mission needs. This volume highlights representative research in all of these areas of emphasis.

The activities of the Physical, Chemical, & Biomolecular Sciences Center are supported by a diverse set of funding sources that reflect the broad impact of our work, both scientifically and programmatically. The research described in this volume illustrates the importance of a strong science base in the physical, chemical, & biomolecular sciences for the success of the Department of Energy's missions. Throughout this work, we have benefited immeasurably from our partnerships with colleagues across the labs, in universities, and in industry. We gratefully acknowledge their collaboration.

We appreciate your interest in our work and welcome your comments and inquiries.

Julia M. Phillips
Director

Table of Contents

Science for National Security Needs

Ares Ultraviolet Laser Induced Fluorescence (UV LIF) Standoff System Development and Testing 6

Radiation Effects Microscopy for First-Pass Success of an Application Specific Integrated Circuit (ASIC) 8

Plasma-Surface Interactions 10

The Influence of Lead Stoichiometry on the Phase Behavior of PZT 95/5 12

Dynamic Mechanical Properties of Alumina-Filled Encapsulants 14

The Very Large Dielectric Constant of $CaCu_3Ti_4O_{12}$: An Inhomogeneous Semiconductor 16

Defects in Compound Semiconductors

Nitrogen Vacancy Diffusion and Trapping in Mg-doped Wurtzite GaN 20

Determination of Minority Carrier (Hole) Transport Properties in GaN-based LEDs 22

Reduced Dislocation Densities in High Aluminum AlGaN Alloys for Deep Ultra-Violet Light Emitting Diodes 24

Reduction of Deep Level Emission in AlGaN-based Deep Ultraviolet Emitters 26

The Interaction of Defects and H in Proton-irradiated GaN(Mg,H) 28

Configurational Defect Bistability in Semiconductors: The MFe Center in InP 30

Terahertz Radiation Science & Technology

Expanding the Operating Range of Terahertz Quantum-Cascade Lasers 34

Millimeter Wave Mixing Using Plasmon and Bolometric Response in a Double-quantum-well Field-effect Transistor 36

Applications for Terahertz Time-domain Spectroscopy 38

Science for Solid State Lighting

Cantilever Epitaxy of GaN Receives R&D100 Award 42

Table of Contents

Interaction of Magnesocene ($MgCp_2$) and Ammonia (NH_3) Explains "Memory Effects" during p-Type Doping of Group-III Nitrides 44

Tunable Broad White Light Emission from Single Size Semiconductor Quantum Dots 46

Mechanics of Materials & Systems

Mechanical Dissipation in Disordered Materials: Micro-scale to Nano-scale 50

Island Coalescence Stress: Solving a 30-Year-Old Scientific Debate 52

Shear in Granular Couette Cells 54

Nanoscale Studies of Surfaces

Implications of Spectroscopic Measurements of an Ultrathin Water Layer 58

Scanning Probe Studies of Water Nucleation and Growth on Aluminum Oxide 60

Switchable Monolayers for Microfluidic Systems 62

Bridging the Nano-Micro Length Scale in Surface Science 64

Biomolecular Materials

A Thermostable Kinesin Motor Protein for Hybrid Nanoscale Systems 68

Nanoparticle Transport Using Motor Proteins 70

BioLaser INCEPTOR for Rapid Detection and Differential Analysis of Anthrax Endospore Simulants 72

Antibody Trapping on Switchable Films 74

New Properties of Nanomaterials

Photocatalytic Nanotubes 78

Fe Nanoclusters: Novel Solution Synthesis and Enhanced Magnetic Properties 80

Nanoporous-carbon: A Revolutionary New Material for Chemical Microsensors 82

Ferromagnetic Domains Induced by Dipolar Coupling? 84

Quantum Phenomena

Tunneling in Double Quantum Wire Devices 88

Hysteresis in Double Quantum Well Structure: Evidence for a Wigner Crystal 90

Dipolar Centers in Quantum Paraelectrics: Mn and Fe in $KTaO_3$ 92

Recent Awards and Prizes 96

Government Advisory Boards and Professional Societies 104

Resources and Capabilities 110

Physical & Chemical Sciences Center FY04 Budget 117

Science for National Security Needs

Ares Ultraviolet Laser Induced Fluorescence (UV LIF) Standoff System Development and Testing

by ***R. L. Schmitt, K. L. Schroder, M. W. Smith, L. J. Krumel, P. J. Hargis, Jr., I. R. Shokair, T. A. Ashlock, J. W. Daniels, J. R. Klarkowski, M. S. Johnson, C. M . Boney, P. J. Claassen, G. I. Magee, M. L. Pedroncelli, J. T. Spooner, and A. R. Lang***

Motivation—Due to the increasing threat of bio-terrorism, we developed a remote sensing system to provide advanced warning of biological weapons threats. Our goal was to design a lidar that was relatively small, inexpensive, and rapidly deployable, specifically suited for homeland security applications.

Accomplishment—We have designed, built and tested a UV laser induced fluorescence (LIF) remote sensing system for the detection of biological aerosols at standoff ranges from 0.5 km to 5.0 km. This lidar system was constructed using commercial off-the-shelf components wherever possible, and the optical and electronic subsystems are modular and small enough to be deployed in a passenger van.

A schematic diagram of the Ares UV LIF lidar system is shown in Fig. 1. A flashlamp-pumped, frequency-tripled, Q-switched Nd:YAG laser provides ~10-ns-wide excitation pulses at 355 nm. Backscattered and fluorescent light collected by an 18.75-cm-diameter Maksutov telescope is collimated and directed to a long-pass dichroic beamsplitter which reflects light with wavelengths shorter than ~360 nm, effectively separating the elastically backscattered laser light from the LIF light. The elastically scattered light is focused onto a photomultiplier tube (PMT) where it is detected and subsequently digitized to provide a record of the aerosol backscatter intensity as a function of range with 1.5 m resolution. Laser induced fluorescence collected by the telescope passes through the long-pass filter and is focused onto the entrance pinhole of an imaging spectrometer. The LIF spectrum is detected by a gated, intensified charge coupled device (ICCD).

The UV LIF lidar system is mounted in a 2-axis gimbal that allows scanning ±45º in azimuth and ±20º in elevation. Figure 2 is a photograph of the Ares system mounted in a van ready for deployment. In operation, the lidar is scanned in azimuth over the desired field-of-regard while the aerosol backscatter signal from the PMT is monitored for evidence of aerosol clouds. When an aerosol cloud is detected, the lidar is automatically pointed at the cloud, and range-gated LIF spectra are recorded using the spectrometer/ICCD. After a nominal 10-second data collection, the LIF spectra are analyzed using Classical Least Squares routines to determine whether or not the cloud contains biological aerosols. The spectrally resolved LIF signal contains valuable information about the spectral shape which is key in discriminating biological from non-biological aerosols.

The Ares lidar system has been successfully operated in a variety of field tests including a DoD-sponsored Product Qualification Test (PQT) at Dugway Proving Ground in Utah which tested its performance as a standoff bio sensor.

Significance—Ares has demonstrated the efficacy of using temporally and spectrally resolved LIF in a practical remote sensing instrument to detect and discriminate threat biological aerosols. As a result of successful field testing, Sandia has signed a Cooperative Research & Development Agreement (CRADA) with Smiths Detection, Edgewood to transfer this technology to industry.

Sponsors for various phases of this work include: National Nuclear Security Administration/NA-22

Contact: Randy Schmitt; Lasers, Optics, & Remote Sensing, Dept. 1128
Phone: (505) 844-9519, Fax: (505) 844-5459, E-mail: schmitt@sandia.gov

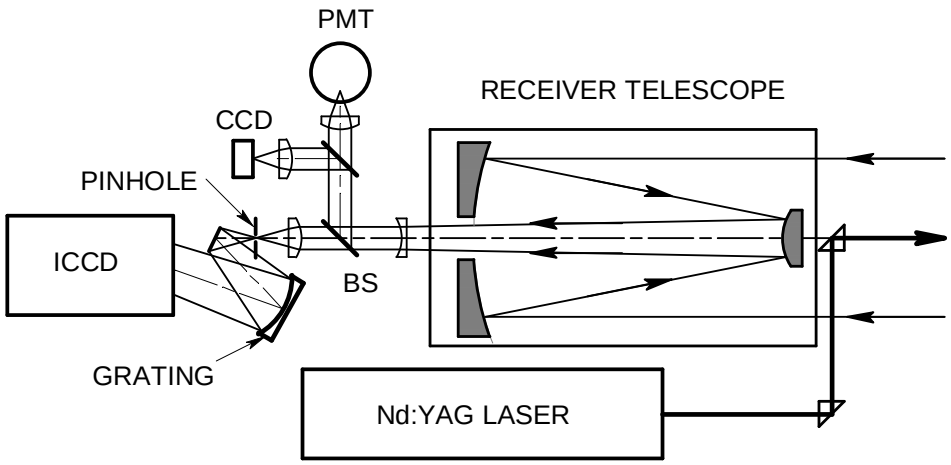

Figure 1. Schematic of the optical system for the Ares UV LIF lidar system.

Figure 2. Photograph of the Ares UV LIF system mounted in a van ready for deployment.

Radiation Effects Microscopy for First-Pass Success of an Application Specific Integrated Circuit (ASIC)

by G.Vizkelethy, B. L. Doyle, P. E. Dodd, M. R. Shaneyfelt, J. R. Schwank

Motivation—Most IC manufacturers – among them Sandia National Laboratories (Sandia) – rely on a standard cell library within a certain technology, which consists of a number of component circuits that can be used to implement various functions in that particular technology. The final product, be it a CPU or memory or other device, will be radiation hard if the components from the cell library are radiation hard. Usually these components are not individually tested but are designed to be radiation hard, either through the inherent circuit design or through process modifications (and often a combination of the two). Unfortunately, there are occasions when a component is found to be radiation sensitive in a complex circuit. A broad beam heavy ion test of an Application Specific Integrated Circuit (ASIC) recently showed an unexpectedly low single event upset (SEU) threshold (Fig. 1). To simulate the circuit response with a TCAD code is practically impossible because of the complexity of the IC; calculations would have to be performed for all of the standard cell circuits comprising the IC. In this case the Sandia nuclear microprobe was used to pinpoint the radiation-sensitive components.

Accomplishment—SEU images were recorded of the regions of the circuit where the designers suspected more sensitivity to radiation. These measurements showed that a certain flip-flop structure that contained latches was responsible for the upsets. Unfortunately, because of the complexity of the circuit it was not possible to directly access the internal nodes of these structures. Therefore, the next step was to design test circuits that modeled the sensitive components, in this case a number of the latch standard cells used in the library. A schematic diagram of one of these test circuits is shown in Fig. 2a. The structure contains transmission gates, and the TCAD (Davinci) calculations showed that the nodes at these transmission gates might be sensitive to heavy ion hits. Figure 2b shows the single event transient (SET) and ion beam induced charge (IBIC) maps overlaid on the GDS II map of the circuits. From this overlay we could clearly identify that the TCAD prediction was correct: the transmission nodes were sensitive to radiation. Removing the resistors from the circuits eliminated the SETs due to the ion hits at the transmission gate nodes. The irony in this is that the resistors were originally put in the circuit to make it more radiation hard. Unfortunately, although the resistors do increase hardness to certain strike locations, they decrease hardness to ion hits at the transmission gates. In addition to the sensitivity predicted by the TCAD code we found that the circuit was also sensitive to hits at the clock inverters, which had not been modeled. This sensitivity is still under investigation.

Significance—Components of the above cell library will be used in the technology used to make radiation hardened Pentium at Sandia. The use of the nuclear microprobe allowed us to pinpoint the radiation sensitive elements in this library, which led to the hardening of these components. This work helped the Microelectronics Development Laboratory (MDL) significantly accelerate the design and manufacturing process of the radiation hardened Pentium processor.

Sponsors for various phases of this work include: Nuclear Weapons/Readiness in Technical Base & Facilities

Contact: Gyorgy Vizkelethy, Radiation-Solid Interactions, Dept. 1111
Phone: (505) 284-3120, Fax: (505) 844-7775, E-mail: gvizkel@sandia.gov

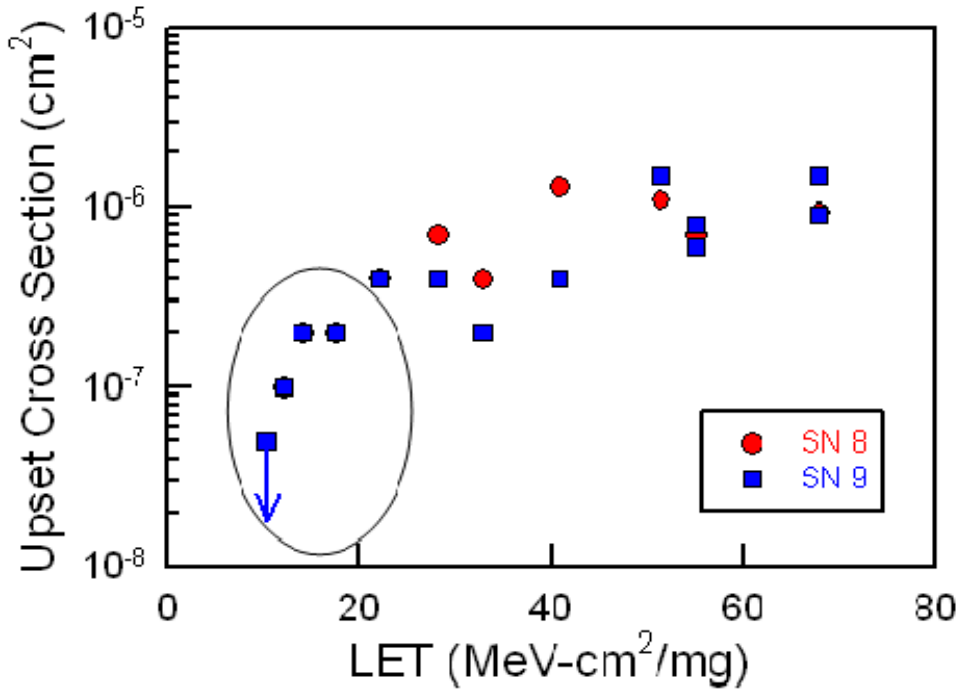

Figure 1. SEU cross section of an Application Specific Integrated Circuit (ASIC).

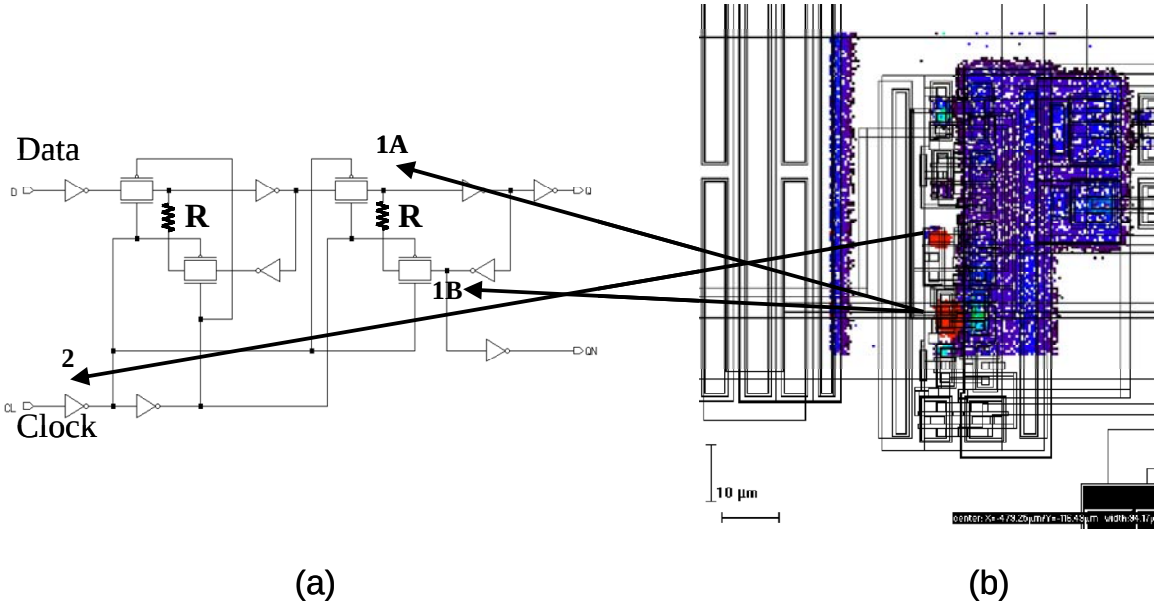

Figure 2. (a) Schematic layout of the latch test structure. (b) SET (red) and IBIC (blue) images overplayed on the GDS II map of the latch structures. 1A and 1B show the transmission nodes where the circuit was sensitive to ion hits. This sensitivity disappeared after removing the **R** resistors, but the circuit is still sensitive to ion hits at location 2, at the clock inverter.

Plasma-Surface Interactions

by E. V. Barnat and G. A. Hebner

Motivation—Plasmas are used for a range of applications such as lighting, microelectronics material processing, surface treatment, cleaning, and arc-based ion sources. These diverse plasma systems all contact a surface. The boundary layer between the bulk plasma and the surface is a sheath layer characterized by large gradients in electric field and space charge. These fields energize charged particles influencing plasma excitation and ionization. Excited species extracted from the plasma subsequently moderate processes that occur on the surface. Byproducts of these surface-based reactions injected into the plasma influence both the distribution of species in the plasma as well as the distribution of electric fields in the sheath.

While there has long been a belief that surfaces can modify the plasma characteristics, a lack of flexible diagnostic tools capable of directly characterizing the interaction between the surface and the plasma impeded the development of a first principles understanding of the critical interaction parameters. Without such characterization, we cannot begin to understand or suggest engineering changes to the surfaces that result in the desired plasma properties.

Accomplishment—We have developed and applied a flexible, non-pertubative, laser-based technique to measure the spatial distribution and temporal evolution of the electrical field in an argon plasma sheath. Changes in sheath structure due to topology and composition of the bounding surface have been characterized for a range of technologically relevant conditions. Figure 1 contains snapshots of the measured field distribution above a metal-dielectric interface at several phases of the radio frequency drive voltage. As the electrode voltage evolves from the maximum [Fig. 1(a)] to the minimum, the sheath electric field decreases and the spatial distribution changes. This provides a measure of the dynamic behavior of the charge in the sheath. Temporal resolution of the technique is currently limited by the pulse width of the laser (~ 5 ns).

The role of surface topology and composition is shown in Figs. 1 and 2. In Fig. 1, the field above the metallic surface is greater than above the dielectric (Teflon) surface, partially due to surface charging of the dielectric material. In Fig. 2a, the step junction shows a complicated sheath structure with field enhancements and depletions depending on location. These field gradients will lead to changes in the ion energy and direction, which can modify ion-surface interactions. Figure 2b shows the impact of two different metals on the sheath structure, likely due to material dependent secondary electron emission coefficients.

Significance—Our *in-situ* measurements are the first to characterize the dependence of the sheath properties on surface topology and composition and will lead to an improved understanding of the significant role that surfaces play in determining the desired plasma and surface properties. In addition, the measurements of spatial and temporal electric field distributions in the plasma can be used to test the validity of assumptions employed in various plasma models. Calibration of field induce Stark shifts in other atomic and molecular species can be made to extend this technique beyond argon.

Sponsors for various phases of this work include: DOE Office of Basic Energy Sciences and Nuclear Weapons/Science & Technology

Contact: Ed Barnat; Lasers, Optics, & Remote Sensing, Dept. 1128
Phone: (505) 284-9828, Fax: (505) 844-5459, E-mail: evbarna@sandia.gov

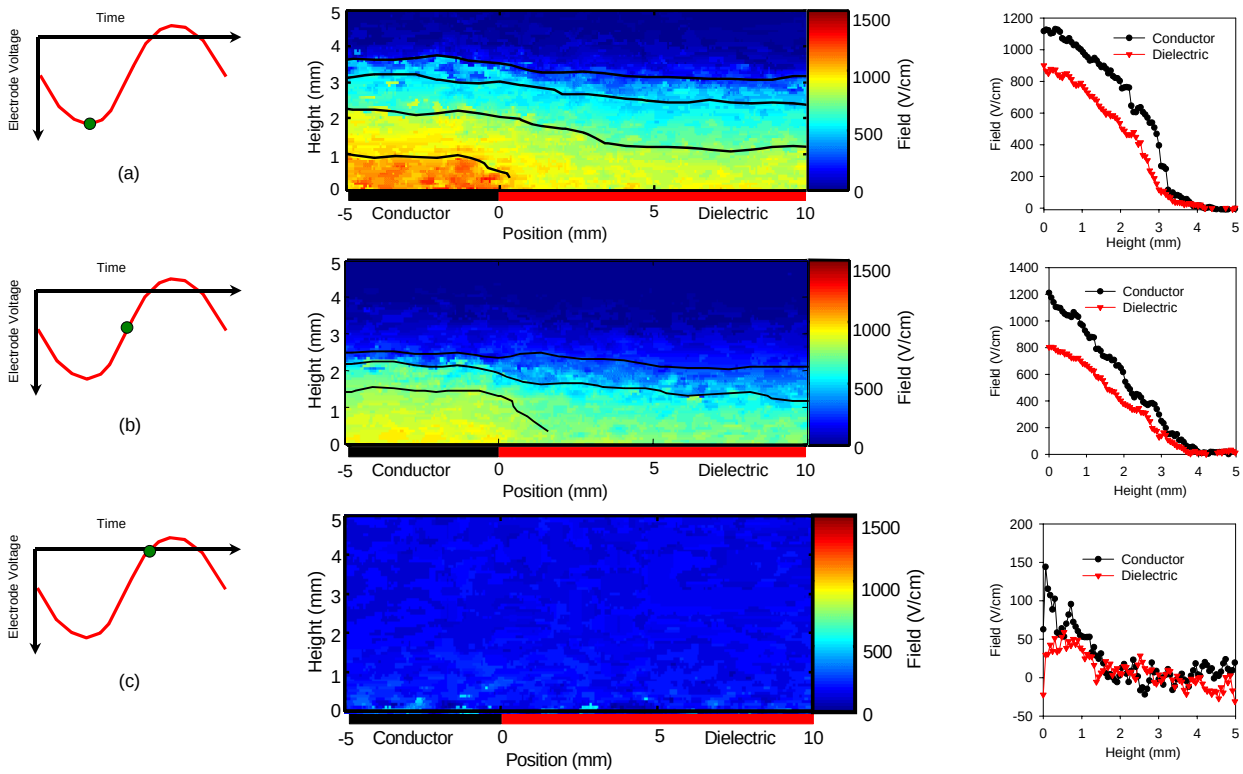

Figure 1: Measured field distribution above a metal-dielectric electrode for three times during the rf phase (a) maximum voltage across the sheath, (b) reduced voltage across the sheath, and (c) minimum voltage across the sheath. Spatially averaged profile of the fields above both surfaces is plotted to the right of each map.

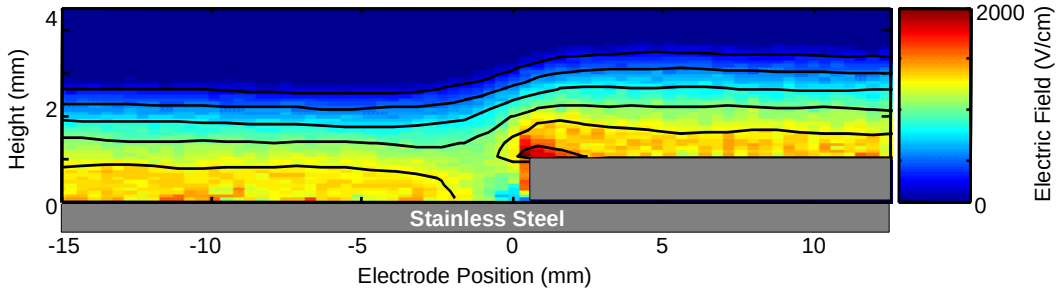

(a) Field distribution above a metal-step (junction)

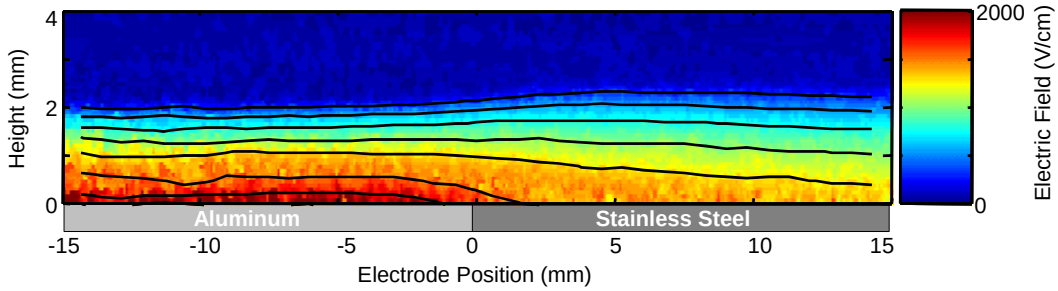

(b) Field distribution above a metal-metal junction

Figure 2: Measured distribution of electric fields above (a) a stepped electrode and (b) above dissimilar metal electrodes. Both the structure and composition of the electrode are observed to influence the distribution of fields in the sheath.

The Influence of Lead Stoichiometry on the Phase Behavior of PZT 95/5

by E. L. Venturini, Pin Yang, and G. A. Samara

Motivation—The ferroelectric (FE) ceramic $Pb(Zr_{0.95}Ti_{0.05})O_3$ or PZT 95/5 is the energy-storage element in explosively-driven power supplies. In the power supply, a shock wave drives the PZT 95/5 through a phase transition from the polarized FE state with bound electrical charge to an antiferroelectric (AFE) state with no bound charge. We are investigating the effects of temperature and varying Pb concentration on this FE/AFE transition using dielectric measurements under hydrostatic pressure. Pb volatility is a serious issue during the high-temperature processing of this ceramic, and a detailed knowledge of Pb stoichiometry effects on the physical properties is necessary.

Accomplishment—PZT 95/5 has five distinct structural phases in a pressure-temperature (P-T) phase diagram. The paraelectric, cubic phase is stable above ~500 K for pressures between 1 bar and several kbar. During cooling at 1 bar, the material transforms to a high-temperature, rhombohedral FE structure near 500 K, designated $F_{R(HT)}$. Upon further cooling, a lower temperature, rhombohedral FE structure appears near 320 K, designated $F_{R(LT)}$. With increasing pressure at temperatures below 320 K, the $F_{R(LT)}$ phase transforms to an orthorhombic AFE structure designated A_O. At higher temperatures and pressures above ~3 kbar, the stable AFE phase has a tetragonal structure designated A_T. The $F_{R(LT)} \rightarrow A_O$ transformation is the basis for the power supply and, hence, changes with lead stoichiometry are of great interest.

Fig. 1 compares the real dielectric constant ε'(P) at 300 K, normalized to its value at 1 bar, versus increasing P for four PZT 95/5 ceramic disks with different Pb concentrations. The sharp drop in ε' marks the $F_{R(LT)} \rightarrow A_O$ transformation P (which is accompanied by charge release in the device) for a particular Pb content. The sharpness of the transition reflects the high quality of the chem prep ceramic samples. The data show a huge decrease in the transformation P with increasing Pb concentration.

The FE/AFE boundary can be determined from isothermal ε'(P) data as shown in Fig. 1 or from ε'(T) and loss ε"(T) data versus decreasing T at constant P. Fig. 2 shows the FE/AFE boundary on a P-T partial phase diagram for the four PZT 95/5 ceramics. Increasing Pb content results in a substantial decrease in the FE/AFE transition pressure between 220 and 320 K. The solid symbols in Fig. 2 reflect transitions determined from ε"(T) data, while the corresponding open symbols indicate ε'(P) measurements. The lines in Fig. 2 are a guide to the eye.

There is substantial P and T hysteresis in the FE/AFE transition (not shown). A phase boundary for the reverse $A_O \rightarrow F_{R(LT)}$ transition was determined from ε' versus increasing T at constant P and ε' versus decreasing P at constant T. Although not as dramatic, increasing Pb content shifts this reverse transition to lower P and higher T.

Significance—Detailed characterization and understanding of the properties of chem prep PZT 95/5 are necessary for improved design and reliable performance in applications. Clearly, the strong dependence of the FE/AFE transition pressure on Pb content imposes severe constraints on the processing protocol where Pb volatility must be compensated. Further, these studies augment a data base to test the numerical modeling. Our results will be important for calibrating and improving the simulations.

Sponsors for various phases of this work include: Nuclear Weapons/Science & Technology

Contact: Eugene L. Venturini; Nanostructure & Semiconductor Physics, Dept. 1112
Phone: (505) 844-7055, Fax: (505) 844-1197, E-mail: elventu@sandia.gov

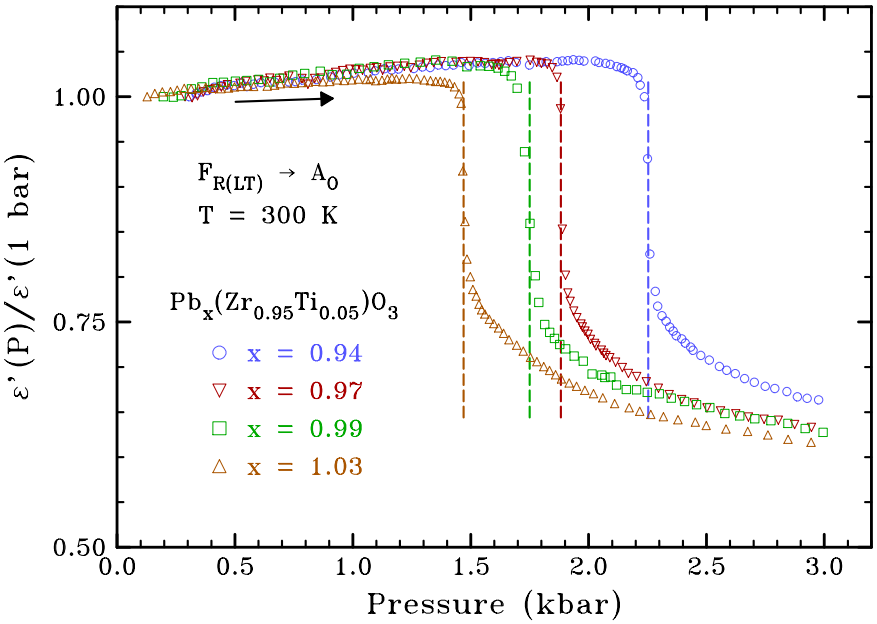

Figure 1. FE/AFE transition pressure at 300 K decreases with increasing Pb.

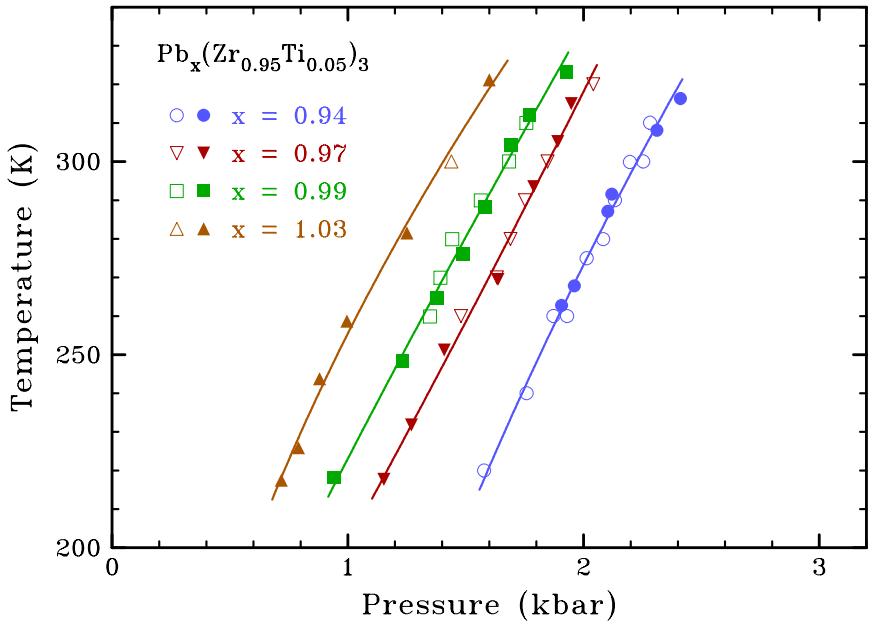

Figure 2. FE/AFE transition pressure decreases with increasing Pb over a range of temperatures.

Dynamic Mechanical Properties of Alumina-Filled Encapsulants

by ***R. E. Setchell, S. T. Montgomery, M. U. Anderson, and D. E. Cox***

Motivation—The shock loading history experienced by a ferroelectric element in an explosively driven power supply is strongly influenced by the shock compression and release properties of the surrounding alumina-filled epoxy (ALOX) encapsulant. In past years we examined these properties in a baseline ALOX containing 43% by volume alumina particles distributed within an epoxy matrix (Fig. 1). Gas gun experiments showed a complex behavior characterized by extended shock profiles and unusually high release-wave velocities. Recent changes in the availability of encapsulant materials have prompted additional studies to examine the effects of modifying the baseline composition. Under current consideration are changes in the total alumina volume fraction, the alumina particle size and morphology, and the epoxy constituents.

Accomplishment—To obtain useful insights into compositional effects on dynamic behavior using a minimum number of gas gun experiments, two types of experimental configurations were chosen (Fig. 2). The first is a conventional uniaxial-strain configuration, which provides a Hugoniot state, a compressive wave profile, and a release-wave velocity. The second type generates a multidimensional diverging, attenuating, wave structure similar to that generated in an explosively driven power supply. This configuration provides a transmitted wave profile, a wave transit time, and a measure of wave curvature. An experiment of each type was conducted with each composition of interest while keeping sample dimensions and impact velocities constant. Figure 3 shows shock and release profiles recorded in uniaxial-strain experiments using samples having different volume fractions of the baseline alumina. These experiments determined the extent to which the average wave velocity, the final Hugoniot state, and the release-wave velocity decreased with decreasing alumina content. Figure 4 shows the wave profiles recorded in corresponding multi-dimensional experiments. Each profile reflects the velocity history that results from axial and lateral release waves overtaking and attenuating an initially stronger compressive wave. A consistent trend with alumina content is no longer apparent, with the strongest wave corresponding to the lowest alumina content. This indicates that lower release velocities can have a stronger effect than reduced Hugoniot properties as alumina content is reduced. In addition to the results shown in Figs. 3 and 4, we have examined compositions having a constant alumina volume fraction but either a different particle morphology or a different epoxy matrix.

Significance—The uniaxial-strain experiments show how basic shock properties change with compositional variations, but the multi-dimensional experiments show effects that reflect a combination of changing properties. A similar combination of compression and release behavior occurs during explosively generated wave propagation, and will govern the stress history experienced by a ferroelectric element. The results shown in Fig. 4, which indicate that a material with lower alumina content could be preferable to the baseline material, suggest that early studies of ALOX properties were insufficient to determine an optimum baseline composition. Our studies of dynamic mechanical properties, together with concurrent studies of other properties, are providing new insights into optimization.

Sponsors for various phases of this work include: Nuclear Weapons/Science & Technology, Advanced Design & Production Technologies/IPPD, and Neutron Generator Development

Contact: Robert E. Setchell; Radiation-Solid Interactions, Dept. 1111
Phone: (505) 844-3847, Fax: (505) 844-4045, E-mail: resetch@sandia.gov

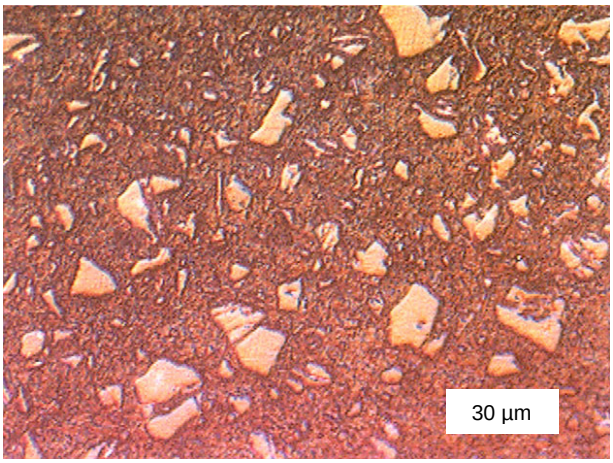

Figure 1. Microscope image of a polished sample surface (baseline ALOX).

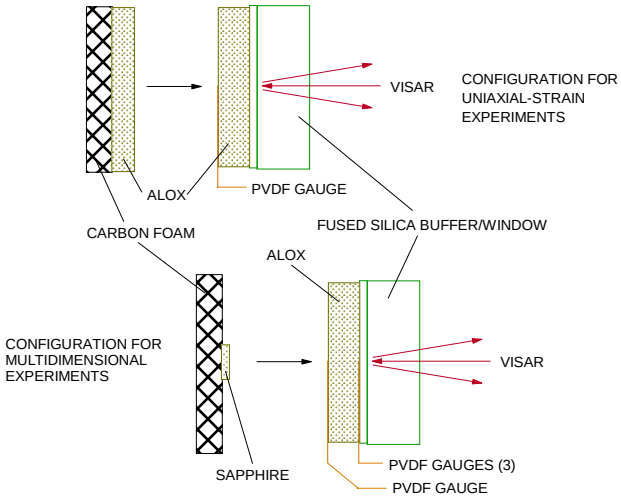

Figure 2. Configurations used for uniaxial-strain shock and release experiments (top) and multidimensional loading experiments (bottom).

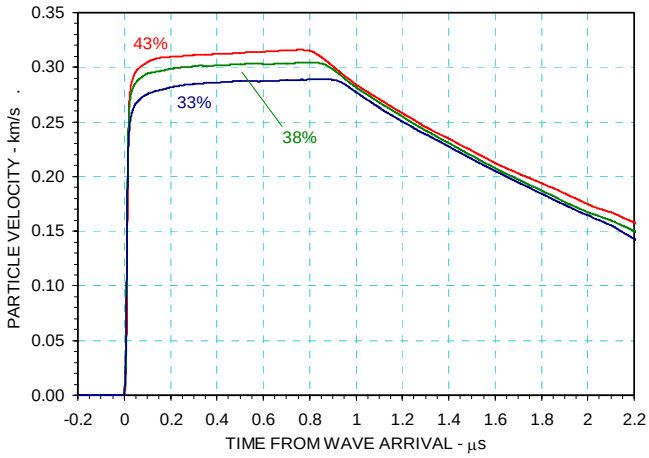

Figure 3. Shock and release wave profiles recorded in uniaxial-strain experiments using ALOX samples with different amounts of alumina. A fixed impact velocity of 0.74 km/s was used in all cases.

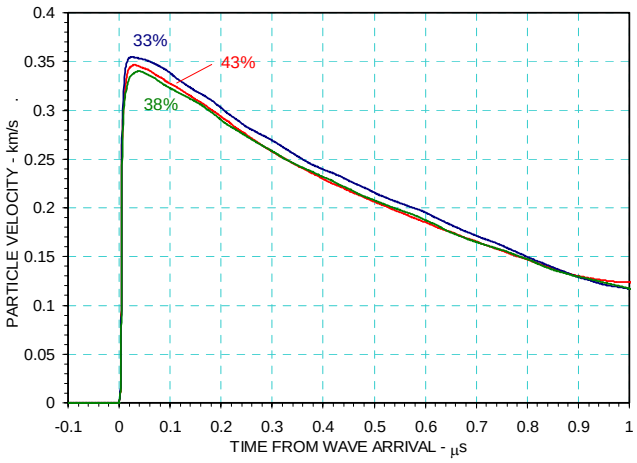

Figure 4. Wave profiles recorded in multi-dimensional loading experiments. A fixed impact velocity of 1.14 km/s was used in all cases.

The Very Large Dielectric Constant of $CaCu_3Ti_4O_{12}$: An Inhomogeneous Semiconductor

by ***R. K. Grubbs, E. L. Venturini, P. Clem, J. J. Richardson, B. A. Tuttle and G. A. Samara***

Motivation—The unusual dielectric properties of $CaCu_3Ti_4O_{12}$ (CCTO) have been of much recent scientific and technical interest. The material has a distorted, complex cubic perovskite (ABO_3)-like structure and exhibits a very large (>10,000) and nearly temperature (T)-independent apparent static dielectric constant, ε', for ceramic samples in the range 200-300K. Such large ε' values make CCTO an attractive material for ultra high energy density capacitors. Below ~ 200K ε' exhibits relaxational behavior, ultimately dropping to a value of ~100 at the lowest T with the crystal structure remaining cubic and centrosymmetric down to at least 35K. While dipole relaxation models associated with the complex crystal structure of CCTO have been suggested to explain this dielectric response, it is now generally agreed that the observed behavior is not intrinsic. However, more complete understanding of the physics is still needed.

Accomplishment—We have investigated the influences of temperature, pressure, and Nb and Fe doping on the dielectric properties of CCTO. The results have revealed new features and have shed much light on the physics of this material. Highlights of the work are as follows: The unusual dielectric relaxation response of CCTO (Fig. 1) is indeed extrinsic and can be understood essentially quantitatively in terms a capacitive barrier-layer model, as for an inhomogeneous semiconductor, consisting of semiconducting grains and insulating grain boundaries. The energetics and kinetics of the main (low T) relaxation process were determined. Two thermally activated regimes related to different conduction processes in the CCTO grains control the dynamics. It is suggested that these two regimes result from the emission of electrons from two energy levels associated with the processing-induced oxygen vacancy. A higher T relaxation process was also discovered that is determined by grain boundary conduction. Both Nb and Fe doping lead to lower ε' in the temperature insensitive region and to lower dielectric loss, but Fe doping leads to the more dramatic effects (Fig. 2). In particular 3 at. % Fe makes CCTO an intrinsic very low loss dielectric and removes the anomalous $\varepsilon'(\omega,T)$ response. It is suggested that the intrinsic behavior is due to carrier compensation in the grains, the Fe-produced holes from Fe^{3+} substituting for Ti^{4+} compensating the conduction electrons attributed to oxygen vacancies. The intrinsic nature of the response for the 3 at.% Fe sample allowed determination of the intrinsic value of ε' ($\approx$75 at low T) and its temperature dependence. This large ε' (compared to that of normal dielectrics where $\varepsilon' \leq 10$) and its decrease with increasing T (unlike normal dielectrics) are largely determined by a low-lying, long wavelength, soft TO phonon – a ferroelectric-like mode. A dielectric anomaly associated with the onset of antiferromagnetic order is observed below the 24 K Neel temperature, providing evidence of coupling between the polarization and sublattice magnetization (Fig. 3).

Significance—We have recently observed very large and nearly T-independent ε' over substantial T ranges and relaxational responses, similar to those for CCTO in studies on doped single crystal perovskites, suggesting that these properties may be general for complex oxides. Thus understanding the physics and controlling the dielectric loss of such materials are essential and could have high payoff in the technology of high energy density capacitors.

Sponsors for various phases of this work include: Laboratory Directed Research & Development and DOE Office of Basic Energy Sciences

Contact: George A. Samara; Semiconductor & Optical Sciences, Dept. 1120
Phone: (505) 844-6653, Fax: (505) 844-4045, E-mail: gasamar@sandia.gov

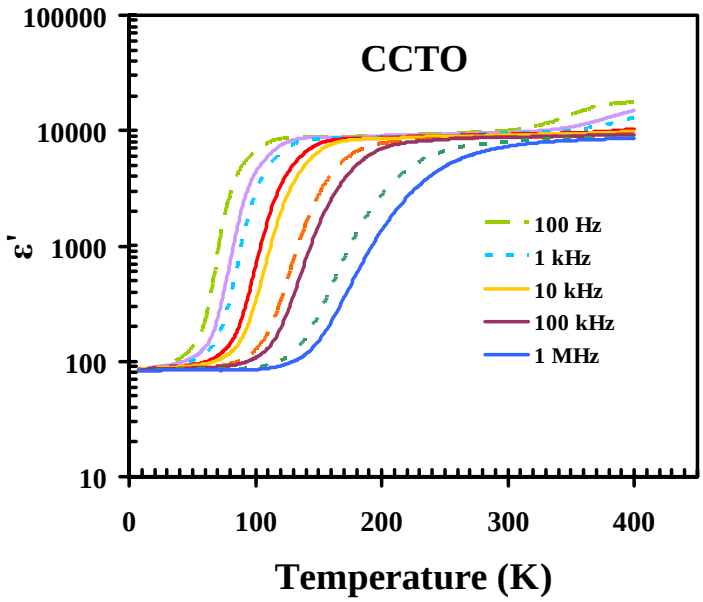

Figure 1. Dielectric response of CCTO as a function of temperature for various frequencies from 100 Hz to 1 MHz. Notice the large, temperature insensitive, plateau value of ε′ and the large frequency dispersion at lower temperatures.

Figure 2. Effect of doping on the dielectric response of CCTO at 10 kHz. As doping levels are increased the CCTO dielectric response decreases. Doping CCTO at a concentration of 3 at. % Fe makes the response of CCTO more characteristic of an intrinsic effect.

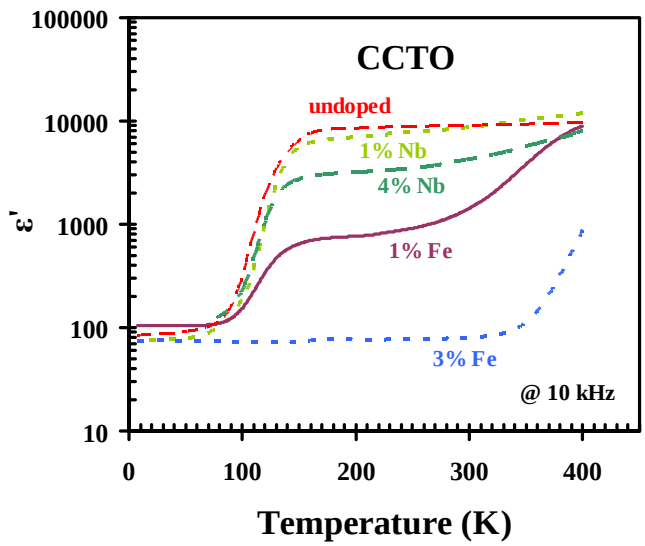

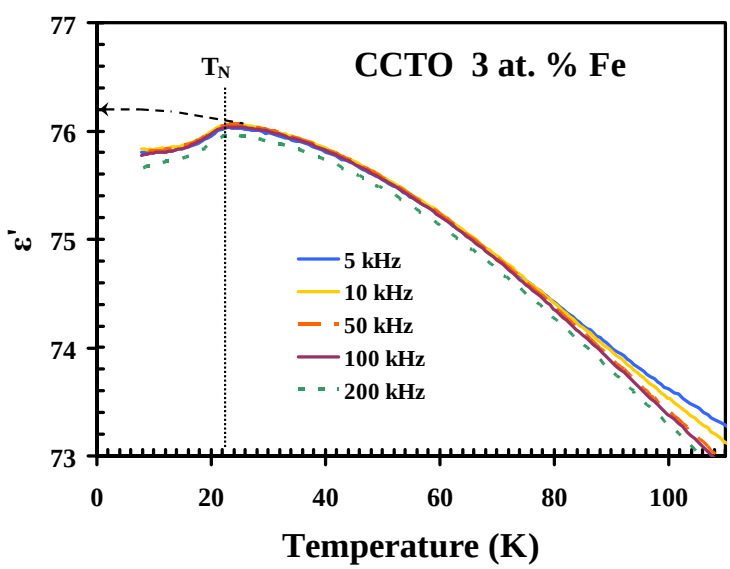

Figure 3. Low temperature dielectric behavior of 3 at. % Fe doped CCTO for various frequencies. An intrinsic dielectric constant of 76.2 is extrapolated at T = 0K. Notice the change in the dielectric response at the Neel Temperature, T_N = 23K, indicating antiferromagnetic ordering.

Defects in Compound Semiconductors

Nitrogen Vacancy Diffusion and Trapping in Mg-doped Wurtzite GaN

by A. F. Wright and T. R. Mattsson

Motivation—The development of group-III nitride light-emitting diodes and laser diodes was enabled by the discovery that Mg acceptors in wurtzite GaN grown via metalorganic chemical vapor deposition (MOCVD) can be activated using a thermal anneal treatment. Following this discovery, it was established that the anneal removes H, which incorporates during growth and passivates the Mg acceptors. Although the dominance of H passivation in MOCVD Mg-doped GaN is not disputed, recent experimental results indicate that the N vacancy (V_N) may play a similar, albeit secondary role in passivating Mg acceptors. Motivated by these results, we have examined aspects of V_N behavior in Mg-doped GaN using density-functional theory (DFT). The goal of these examinations was to gain a deeper understanding of this defect and thereby aid in the development of more efficient group-III nitride light-emitting devices.

Accomplishments—We have used DFT to investigate V_N diffusion in wurtzite GaN and complexes of V_N with an Mg acceptor. The DFT calculations made use of recent enhancements in DFT techniques, which have been demonstrated to improve the accuracy of DFT results. These enhancements include the generalized-gradient approximation for exchange and correlation, the treatment of the Mg 2*p* and Ga 3*d* as valence electrons, thereby allowing them to participate in the formation of bonds, and the nudged-elastic-band and dimer methods which are used to identify V_N diffusion paths and the associated transition states.

Two V_N diffusion paths were identified: a *perpendicular* path producing V_N movement strictly perpendicular to the wurtzite *c* axis and a *diagonal* path producing V_N movement both perpendicular and parallel to the *c* axis. The V_N charge state was found to strongly influence the diffusion activation energies, which range from 2.49 eV for the +3 charge state to 3.55 eV for the +1 charge state along the perpendicular path, and from 2.65 eV in the +3 charge state to 3.96 eV in the +1 charge state along the diagonal path. The sequence of atomic configurations involved in V_N diffusion along the diagonal path is shown in Fig. 1 for the case of the +3 charge state. The transition state is shown in Fig. 1b and is characterized by an N atom bonded to two Ga atoms instead of four as in bulk GaN.

Two types of MgV_N complexes were identified: a *parallel* configuration with V_N located next to Mg and along the *c* axis from it, and a *perpendicular* configuration with V_N located next to Mg and perpendicular to the *c* axis from it. The dissociation energies of these complexes were found to range from 0.29 to 0.58 eV, depending on the configuration and charge state. The local-energy-minimum configurations of MgV_N in the +2 charge state are shown in Fig. 2. The dissociation energy of the perpendicular configuration, 0.58 eV, is comparable to the dissociation energy of the MgH complex in GaN.

Significance—The DFT results suggest that V_N should be present in Mg-doped MOCVD GaN and difficult to remove with thermal anneal treatments. Furthermore, the charge states of V_N and MgV_N are predicted to change during thermal anneal treatments due to the ensuing shift in the Fermi level as H is removed from the material. The consequences of these DFT results are being explored at Sandia via experimental and diffusion-reaction modeling studies.

Sponsor of this work is: DOE Office of Basic Energy Sciences and Laboratory Directed Research and Development

Contact: Alan F. Wright; Nanostructure & Semiconductor Physics, Dept. 1112
Phone: (505) 845-0445, Fax: (505) 844-1197, E-mail: afwrigh@sandia.gov

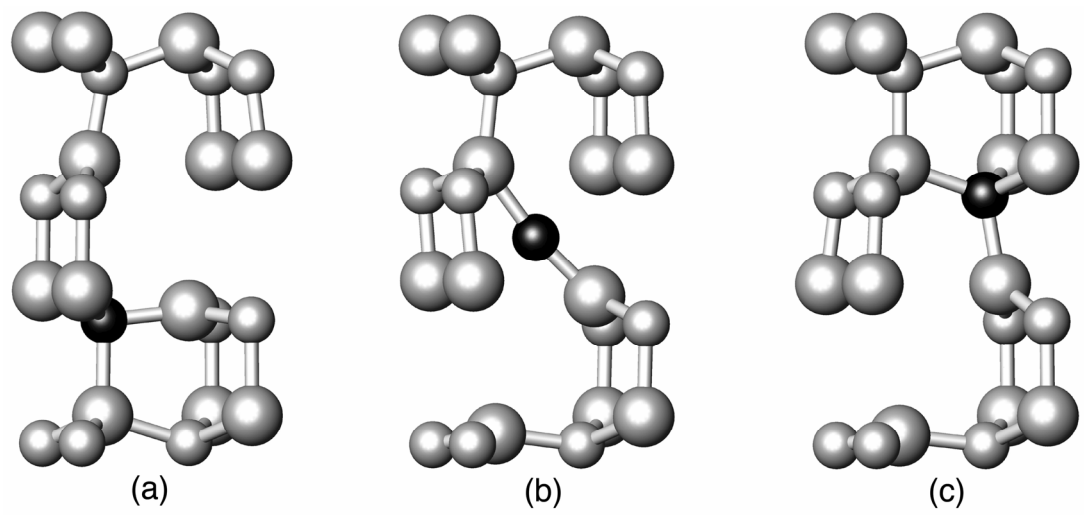

Figure 1. Diagonal diffusion path for V in the +3 charge state. (a) and (c) are local-energy-minimum configurations and (b) is the energy saddle-point configuration. Large, light colored spheres denote Ga atoms, small, light colored spheres denote N atoms, and the small, dark colored sphere denotes the N atom that changes place with V along the diffusion path. The views are orthographic with the view direction rotated ≈10° from [1, -1, 0, 0].

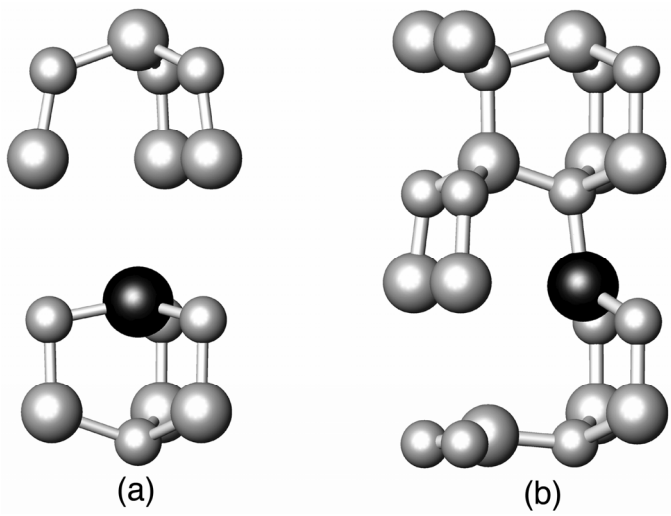

Figure 2. Local-energy-minimum configurations for MgV in the +2 charge state. (a) shows the parallel configuration and (b) shows the perpendicular configuration. Large, light colored spheres denote Ga atoms, small, light colored spheres denote N atoms, and large, dark colored spheres denote Mg atoms. The views are orthographic with the view direction rotated ≈ 10° from [1,-1,0,0].

Determination of Minority Carrier (Hole) Transport Properties in GaN-based LEDs

by ***Steven R. Kurtz and Robert J. Kaplar***

Motivation—Bipolar devices are required in most optoelectronic and electronic applications of wide bandgap, GaN-based materials. At Sandia, one of our main thrusts is the development of bright light-emitting diodes (LEDs) and lasers at UV, blue, or green wavelengths. These devices would find wide-scale utilization, ranging from solid-state white lighting, displays, and data storage (blue and green) to bio-agent sensors (UV).

Transport of massive holes ($m^*_h \approx 1.8\ m_e$) in nitride-based bipolar devices, such as LEDs, is a critical factor determining performance. Conventional majority-carrier Hall mobility measurements overlook the influence of a large density of defects, and minority-carrier transport needs to be investigated directly. Towards this end, we have modified techniques and models which were initially proposed 50 years ago. Our combined optical and electrical transient study provides the first picture of minority carrier diffusion in nitride devices.

Accomplishment—To determine the transport properties of massive, minority-carrier holes in GaN, we have implemented a new technique that combines the measurement of electrical and optical transient responses of an LED to a forward-to-reverse bias voltage pulse. Using this method, we have observed hole transport in a p^+-n single quantum well (SQW) InGaN/GaN LED, where the SQW was positioned in the n-region. The device was grown on sapphire using metal-organic chemical vapor deposition. Hole transport results may depend strongly on growth substrate and conditions. SQW LED emission occurred at a wavelength of 400 nm.

Transient responses of the LED were induced using a transmission-line technique (see inset Fig. 1a). We observed that both the electrical current (Fig. 1a) and optical emission transients (Fig. 1b) displayed two-step decays, a signature of diffusive behavior. A classic solution to the time-dependent diffusion equation describes transient forward-to-reverse bias dynamics of the minority carrier distribution. (shown in Fig. 2). This model produced a self-consistent description of both optical and electrical data and accurately determined the GaN minority-carrier hole lifetime ($\approx$ 760 ns), diffusion length ($\approx$ 590 nm), and mobility ($\approx 0.2\ cm^2/Vs$), which is more than an order of magnitude lower than typically reported values of majority-carrier hole mobility. Further, temperature-dependent measurements of the hole mobility indicated that it is thermally activated ($E_\mu \approx 50$ meV). The magnitude and temperature dependence of the mobility imply that minority hole transport is trap-modulated, and the lifetime is suggestive of slow recombination processes occurring through deep levels.

Significance—Experimental techniques and models have been developed to provide the first characterization of minority carrier diffusion in bipolar GaN devices. In future studies we hope to understand the mechanisms controlling hole injection and transport. These methods should lead to improved performance of GaN devices and provide guidance for device design and optimization.

Sponsors for various phases of this work include: DOE Office of Basic Energy Sciences, Laboratory Directed Research & Development, and Defense Advanced Research Projects Agency

Contact: Steven R. Kurtz; Semiconductor Material & Device Sciences, Dept. 1123
Phone: (505) 844-9637, Fax: (505) 844-3211, E-mail: srkurtz@sandia.gov

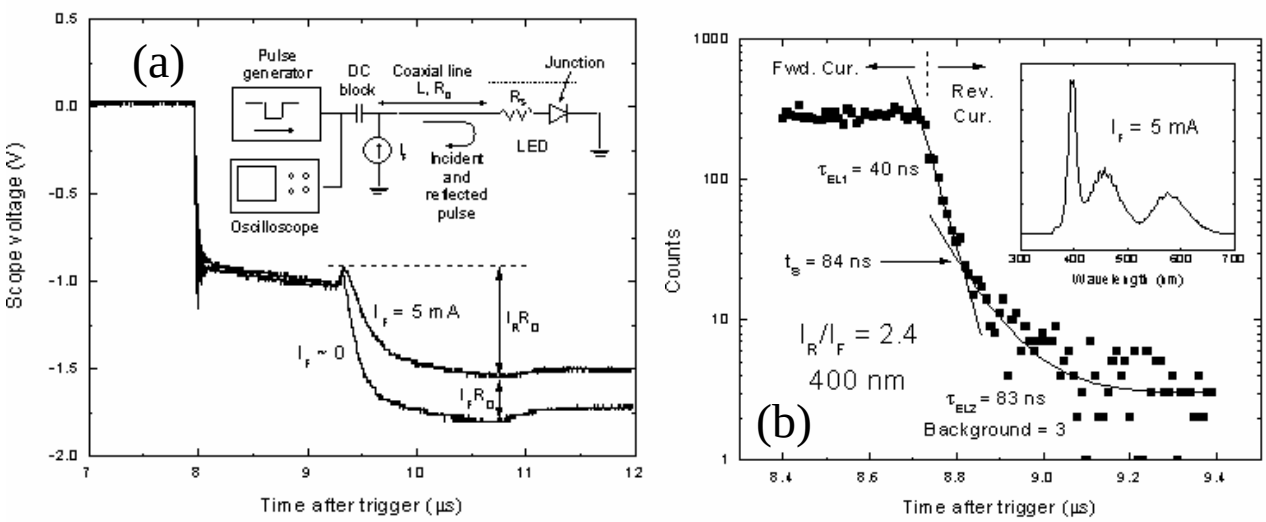

Figure 1. (a) Step-recovery oscilloscope traces showing the current transient of the SQW LED with high (I_F = 5 mA) and low ($I_F \approx 0$) forward current [inset (a): Pulse recovery experiment]. (b) Transient emission of the SQW LED under bias/pulse conditions identical to those used for the high-current experiment of (a) [Inset (b): 300 K LED emission spectrum at I_F = 5 mA].

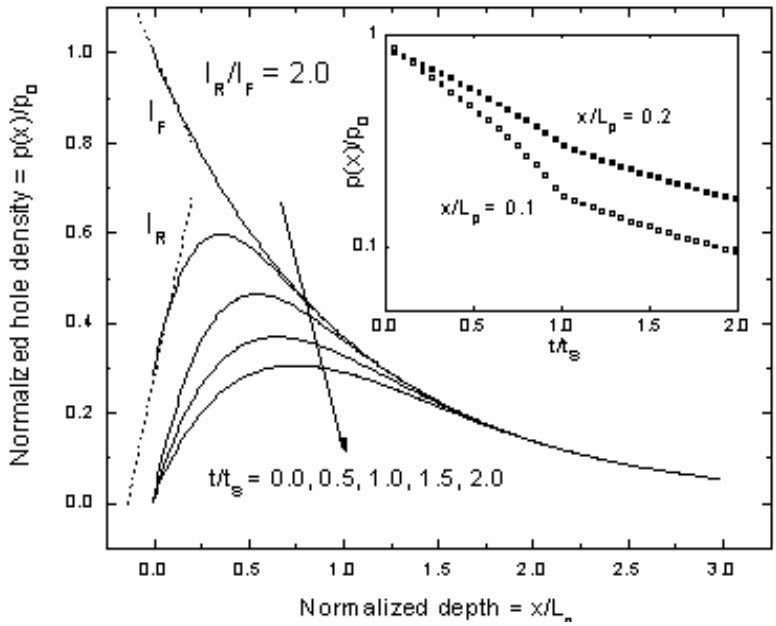

Figure 2. Minority-carrier hole distribution in the n-type side of the SQW LED for various times, obtained by solving the diffusion equation. Inset: Temporal decay of the hole density for two positions in the distribution.

Reduced Dislocation Densities in High Aluminum AlGaN Alloys for Deep Ultra-Violet Light Emitting Diodes

by ***A. A. Allerman, M. H. Crawford, A. J. Fischer, K. H. A. Bogart, S. R. Lee, D. D. Koleske, D. M. Follstaedt, N. A. Missert, and P. P. Provencio***

Motivation—Solid-state light sources emitting at wavelengths between 200nm and 300nm would enable technological advances in many areas such as fluorescence-based biological agent detection, non-line-of-sight (NLOS) communi- cations, water purification, and industrial processing. Over the past year, we have demonstrated light emitting diodes (LEDs) based on alloys of AlGaN in prototype systems for NLOS communications and bio-agent detection. These LEDs are based on the growth of AlN-AlGaN (50-90% Al) buffer layers on sapphire substrates and are transparent to the LED emission. These materials typically have dislocations densities that are 10-100 times higher than the dislocation density of GaN buffer layers on sapphire used in commercial blue (460nm) LEDs. We are investigating ways to lower the dislocation density of these high Al containing materials by controlling the nucleation process on the sapphire substrate.

Accomplishment—Since non-conducting sapphire substrates are used, LED performance in the deep-UV is dependent on achieving good lateral current transport in high Al composition AlGaN alloys. Recent advances in the nucleation of the underling AlN buffer on sapphire have resulted in a 5-10x reduction in dislocation density of the overgrown AlGaN films used in deep UV-LEDs. This has resulted in both an improvement in electron mobility (Fig. 1) as well as an increase in n-type doping efficiency using SiH_4. We have demonstrated n-type conduction in films to 90% Al due to reduced carrier compensation that we have observed in films with higher dislocation density. Figure 2 shows the sheet resistance of LEDs as a function of dislocation density as measured by x-ray diffraction using a technique described in the *Physical and Chemical Sciences Center Research Briefs 2003*, p. 22. The sheet resistances have been normalized to a thickness of 1µm to allow comparisons between devices with different thicknesses of Si-doped AlGaN. While the Si-AlGaN layer in the LEDs were grown under different conditions, or had different compositions or underlying buffer layers, the resistance is found to be largely correlated to the density of dislocations that have an edge component, and to a lesser extent, dislocations that have a screw component. Realizing a lower dislocation density improves n-type conductivity at higher Al compositions by both improving the electron mobility and increasing the range of electron concentrations that can be achieved. While many factors influence LED performance such as device structure and processing, it is not surprising that the best LEDs we have measured at any wavelength are those where the density of dislocations with an edge component is less than $3x10^{10}cm^{-2}$. To date, LEDs have only been tested on films where the dislocation density exceeded $1x10^{10}cm^{-2}$.

Significance—The reduction of dislocation density in AlGaN films is expected to improve the LED performance by several mechanisms. An increase in optical power due to reduced ohmic heating with the improved electron transport is expected. Also, an increase in internal quantum efficiency due to lower non-radiative recombination rates typically associated with lower dislocation density should be observed. These improvements will help to move deep UV-LEDs out of prototype units and into fieldable systems.

Sponsors for various phases of this work include: Defense Advanced Research Projects Agency, Laboratory Directed Research and Development, and Nuclear Weapons/Science & Technology

Contact: Andrew A. Allerman; Advanced Materials Sciences, Dept. 1126
Phone: (505) 845-3697, Fax: (505) 844-3211, E-mail: aaaller@sandia.gov

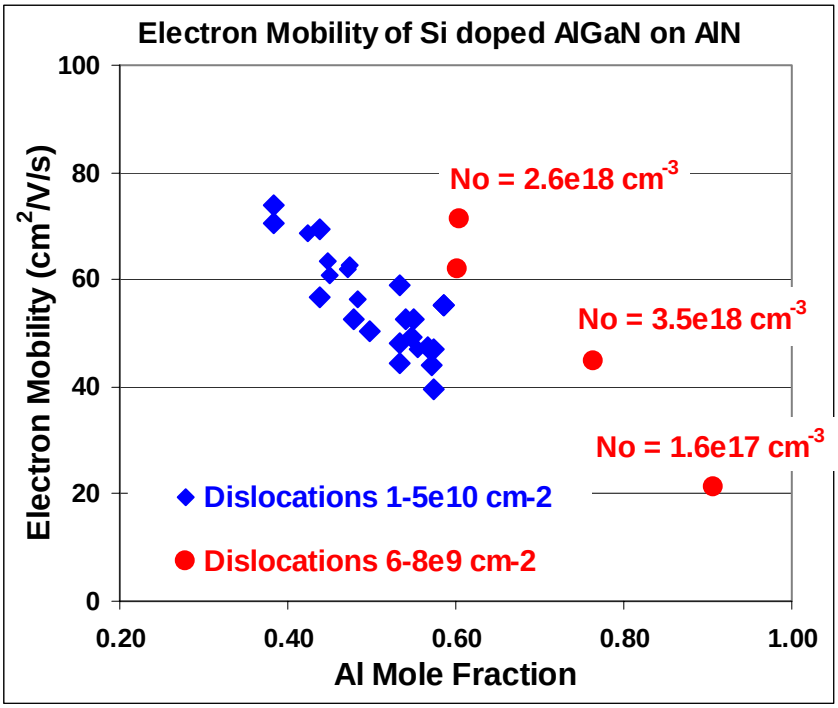

Figure 1. Electron mobility determined from Hall measurements of Si doped AlGaN alloys as a function of Al composition and dislocation density is shown. An increase in mobility and SiH_4 doping efficiency is observed in alloys where the density of dislocations with an edge component is less than $1x10^{10}cm^{-2}$. The electron concentration (No) of selected samples is shown.

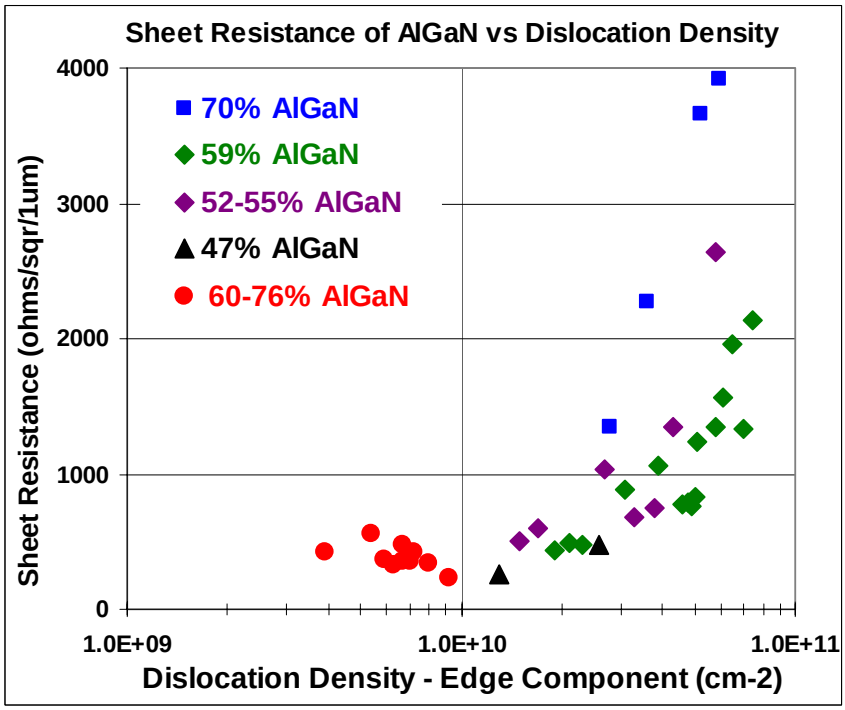

Figure 2. The normalized sheet resistance of the Si-doped AlGaN layer used in various LEDs as a function of dislocation density of dislocations with an edge component.

Reduction of Deep Level Emission in AlGaN-based Deep Ultraviolet Emitters

by M. H. Crawford, A. A. Allerman, A. J. Fischer, K. H. A. Bogart, S. R. Lee, R. J. Kaplar, and S. R. Kurtz

Motivation—Solid-state deep ultraviolet (UV) light emitting diodes (LEDs) are sought as excitation sources for fluorescence-based bio-sensing applications. Potential performance advantages over traditional lamp-based or laser-based systems include compactness, wavelength tailorability, cost effectiveness, and robustness. Recently developed deep UV (270-290 nm) LEDs based on AlGaN-alloys show promise to achieve these performance advantages but are limited by the presence of significant sub-bandgap, deep level emission bands in the electroluminescence spectrum. These emission bands overlap with relevant fluorescence bands and reduce the ability to achieve high detection sensitivity in bio-fluorescence measurements.

Accomplishment—Previous reports have shown that emission from deep level states of AlGaN multi-quantum well LEDs exists in at least two broad bands, one centered in the UV at approximately 330 nm and another band centered in the near-UV/blue (400-450 nm) region of the spectrum. The 330 nm band in particular can represent a significant portion of the total LED emission, with recent reports of a peak emission intensity that is only 10-100 times weaker than the quantum well emission band. We have demonstrated significant reduction in emission from 330 nm-band deep level transitions through optimization of the heterostructure design and growth conditions of AlGaN multi-quantum well LEDs grown by metal-organic vapor phase epitaxy. Our studies revealed that a potential limitation to both device efficiency and spectral purity was the lack of sufficient carrier confinement in the LED structure. In particular, electron leakage out of the quantum well region and subsequent recombination through deep level states in the p-type AlGaN layer of the structure was identified as a likely candidate for the sub-bandgap emission in the 330 nm region. To minimize this emission, we implemented a high bandgap $Al_xGa_{1-x}N$ (x~0.70) electron block layer on the p-side of the structure, as shown in Fig. 1. A key challenge of this approach is to minimize the detrimental barrier to hole injection while simultaneously reducing electron leakage. Optimization of the Al-composition profile, thickness and overall materials growth conditions of the electron block layer resulted in greater than 10X reduction in 330 nm band emission while maintaining or increasing the quantum well emission efficiency. A semi-log plot of electroluminescence spectra from a 300 µm x 300 µm AlGaN flip-chip LED structure is shown in Fig. 2a. The spectra are normalized to the quantum well emission band (274 nm) and shown as a function of injected current to reveal the saturation of deep level emission with increasing current. At 100 mA, the spectrum shows a 330 nm band that has a peak intensity approximately 700X lower than the main quantum well emission, representing a notable advance in the spectral purity of AlGaN-based LEDs. These LEDs were operated at 8.3V with an output power of 0.77 mW at 100 mA DC.

Significance—The demonstration of near-milliwatt level solid-state sources in the 270-290 nm region with reduced deep level emission has accelerated their implementation into prototype biosensing systems. The compactness and wavelength tailorability of these sources will enable next-generation biosensing systems with enhanced capabilities for addressing problems of great interest to national security.

Sponsors for various phases of this work include: Defense Advanced Research Projects Agency

Contact: Mary H. Crawford; Semiconductor Material & Device Sciences, Dept. 1123
Phone: (505) 284-9380, Fax: (505) 844-3211, E-mail: mhcrawf@sandia.gov

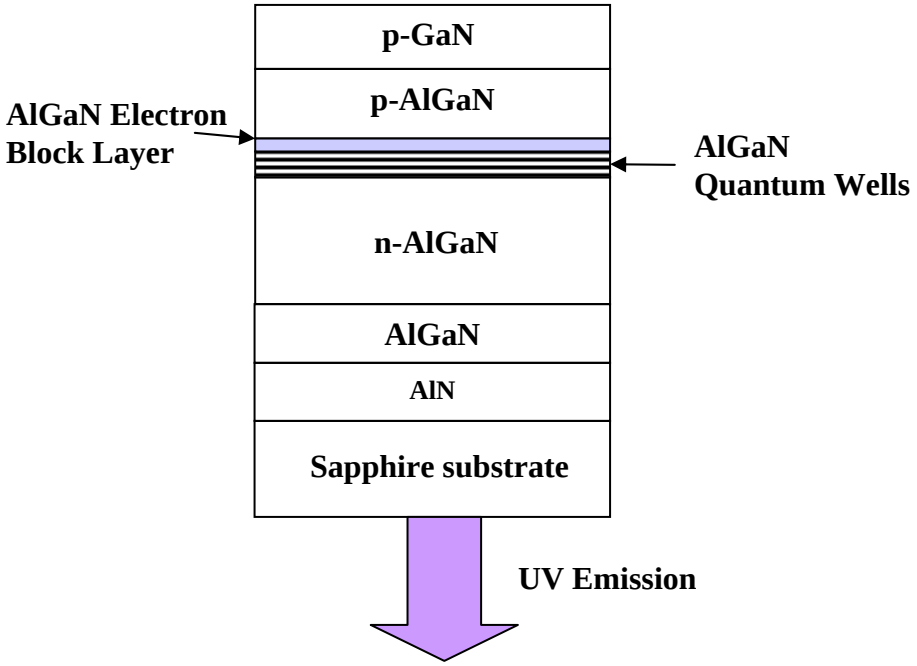

Figure 1. Schematic of AlGaN-based deep UV LED structure, showing the primary n-type and p-type AlGaN layers, the quantum well active region and the AlGaN electron block layer.

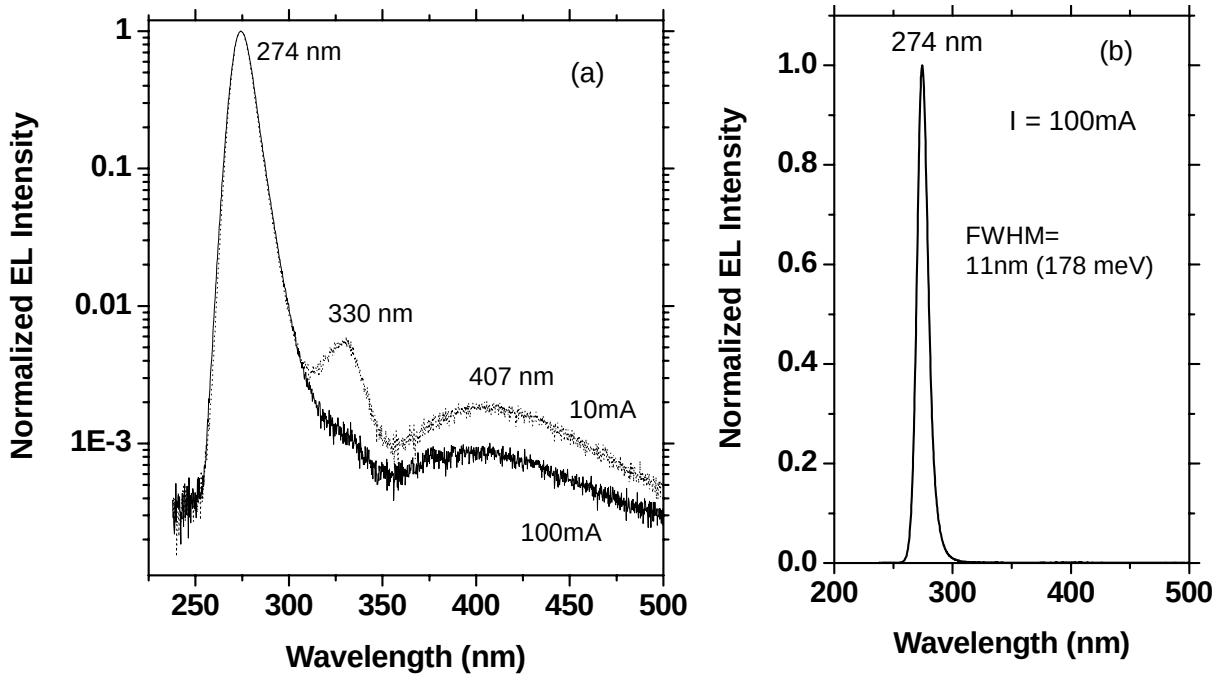

Figure 2. (a) Semi-log plot of normalized electroluminescence spectra from an AlGaN multi-quantum well LED at 10 mA and 100mA DC injection current. The primary quantum well emission is at 274 nm, and the deep level bands are at 330 nm and 407 nm. (b) Linear plot of electroluminescence at 100mA.

The Interaction of Defects and H in Proton-irradiated GaN(Mg,H)

by C. H. Seager and S. M. Myers

Motivation—P-type GaN is an increasingly important material because it is the hole-injecting layer in a variety of GaN and AlGaN-based light-emitting diodes (LEDs). The interactions of grown-in hydrogen with magnesium acceptors and the self compensation of acceptors by native defects are both important issues which must be understood before the full potential of this semiconductor can be realized. Local vibrational modes (LVMs), visible with fourier transform infrared spectroscopy (FTIR), can be studied to learn more about native defects that are otherwise difficult to probe.

Accomplishment—In order to study defects whose low equilibrium densities make detection difficult, magnesium-doped, p-type GaN containing H was irradiated with MeV protons at room temperature and then annealed at a succession of increasing temperatures, with the behavior of defects and H in the material being followed through infrared absorption spectroscopy, nuclear-reaction analysis (NRA) of the H, and photoluminescence. In the as-grown condition H from the MOCVD growth environment complexes with Mg acceptors, creating a distinctive LVM at 3122 cm^{-1} (Fig.1). The isotopic variant of this same mode at 2319 cm^{-1} is visible when hydrogen is removed from the material with a 900°C anneal and replaced with deuterium (Fig. 2). After implantation with protons which are energetic enough to pass all the way through the GaN film, the LVM spectra evolve as both as-grown and deuterium exchanged samples are heated in a sequence of one-hour vacuum anneals (Figs. 1 and 2). Beginning at 300°C the MgH(D) LVM is replaced with new H and D-related modes at 3134 and 2328 cm^{-1}. At annealing temperatures of 500°C and above these new modes begin to disappear and the original MgH(D) LVM is partially restored. Finally, above 700°C, all LVMs disappear, and at 800°C NRA data indicate that H(D) has left the material completely. Figure 3 shows the temperature dependence of the MgD mode and the "new mode" at 2328 cm^{-1}. It also shows the evolution of a new green luminescence peak which is only seen in these proton-irradiated and thermally annealed samples. Because theoretical studies indicate that Ga interstitials should be highly mobile at room temperature, we believe that Ga interstitial-vacancy Frenkel pairs should anneal out after the 300°C thermal treatment. This leaves N vacancies and interstitials as the defects which are most likely to produce the effects seen in Figs. 1-3. Because the frequency differences between the MgH(D) LVMs and the new modes are small, it is likely that the atomic configurations of the new defects are only slightly different from the known arrangement of the MgH(D) complex. This is consistent with the movement of an N interstitial to a site adjacent to the original complex. The complete disappearance of all H(D) related modes (Fig. 3) well before H has left the material suggests that H can find another trap in the GaN. Theory suggests that this "LVM-invisible" trap is the N vacancy, since its predicted LVM should be at wavelengths where the GaN substrate is strongly absorbing.

Significance—This work identifies a new native-defect-related structure in GaN. It has also provided insights into possible H trapping in GaN which has N vacancies introduced during the film growth process. Other Sandia research has also shown evidence for this effect.

Sponsors for various phases of this work include: DOE Office of Basic Energy Sciences and Laboratory Directed Research & Development

Contact: Carleton H. Seager; Radiation-Solid Interactions, Dept. 1111
Phone: (505) 844-9168, Fax: (505) 844-1197, E-mail: chseage@sandia.gov

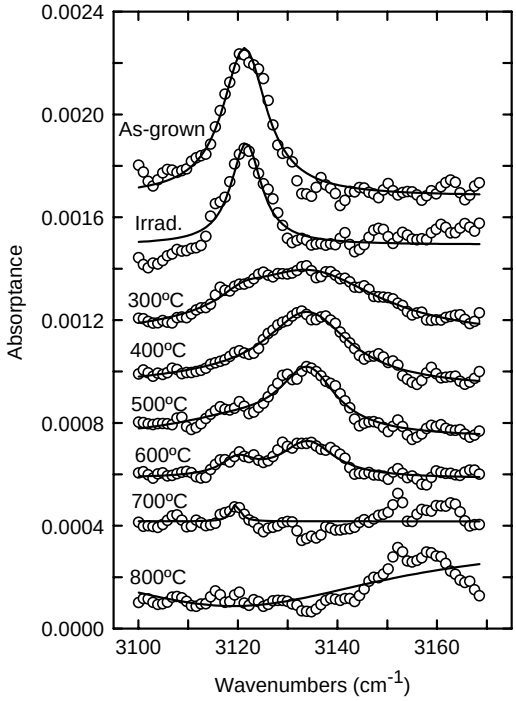

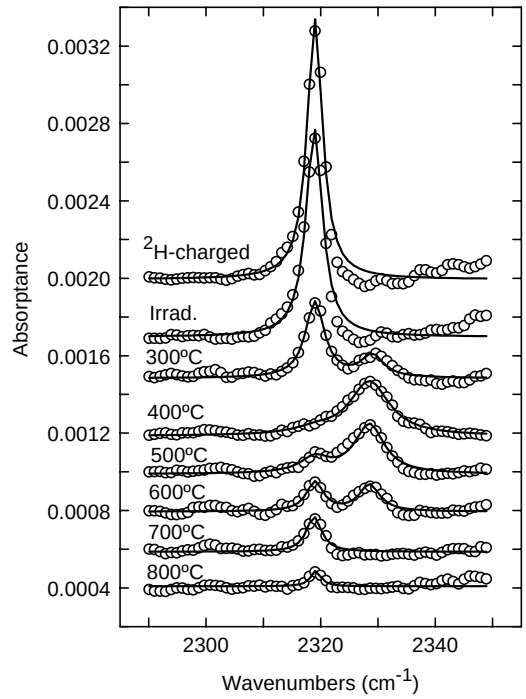

Figure 1 (left) and **Figure 2** (right). Sequential IR absorption spectra from specimens containing grown-in ^{1}H (Fig. 1) or ^{2}H exchanged for ^{1}H after growth (Fig. 2). The samples were irradiated at room temperature with 1-MeV protons and then subjected to a series of 1-hour vacuum anneals. The irradiation dose was 1.65×10^{16} cm^{-2}. The curves represent Lorentzian fits used to evaluate absorption strengths.

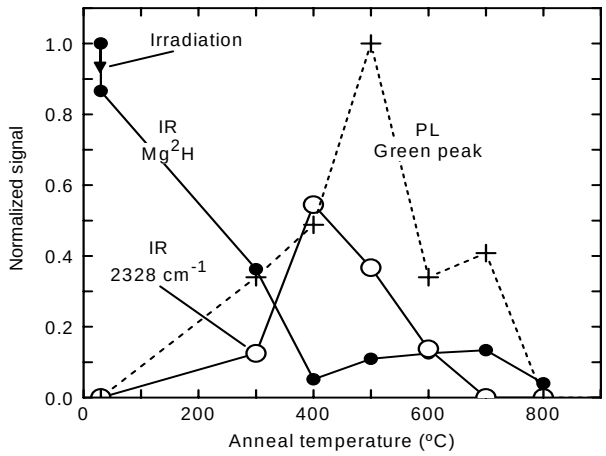

Figure 3. Normalized amplitudes of the IR absorption and green photoluminescence versus anneal temperature for a ^{2}H-charged specimen that was irradiated and then vacuum annealed.

Configurational Defect Bistability in Semiconductors: The MFe Center in InP

*by G. A. Samara**

Motivation—One of the more interesting and important developments in the study of lattice defects and their associated deep electronic levels in covalent semiconductors has been the discovery that an ever-increasing number of important defects exhibit configurtional bistability (or multistability). Configurationally bistable defects are defects which, for the same charge state, can exist in two different configurations with distinct electronic and optical properties. Reversible transformations between the two configurations can be induced by thermal, electrical or optical means, and the configuration, which is observed experimenttally, is dependent on the thermal, electronic and optical history of the sample. The MFe-center in Fe-doped n-InP is such a configurationally bistable defect. Although its properties have been characterized at 1 bar in considerable detail, much remains to be learned about the atomic structure of its two configurations and the nature of the transformations between them. In the present work we show that measurements under pressure shed much new light on the physics of this center.

Accomplishment—The MFe center, which is formed during high temperature p^+ doping (Zn^{2+} or Cd^{2+}) to form p^+/n junctions on Fe-doped InP, was first studied by Levinson, et al., (J. Electron Mats. 14a, 1133, 1985). When occupied by electrons, it can be reversibly placed in either of two configurations, A or B. A is obtained by cooling the junction with no applied bias, i.e., in the presence of electrons, whereas B is obtained by cooling under reverse bias, i.e., in the absence of electrons, followed by zero biasing to fill the traps. The signatures of the two configurations in thermally-scanned capacitance (TSCAP) and deep level transient spectroscopy (DLTS) are shown in Figs. 1 and 2. The emission from B has two steps, B1 and B2, each involving the emission of one electron. We find that hydrostatic pressure has drastic influence on the energetics and kinetics of the various processes associated with the MFe center. The energies and their pressure dependences as well as the activation volumes (ΔV^*) for these processes were determined. In the absence of barriers to electron capture, or for small barriers, ΔV^* can be interpreted as the breathing mode relaxation associated with electron emission or capture. At ≥ 8 kbar only the A configuration exists (Figs. 1 and 2) regardless of bias conditions during cooling because at these pressures the B→A transition energy becomes the smallest energy of the problem (Fig. 3). These pressure results have allowed us to critically test a proposed atomic model for the MFe center. In this model the A configuration is taken to be the Fe anti-site/In vacancy complex, $Fe_{In}\bullet V_{In}$, and the A→B transition involves a nearest-neighbor hop of a P atom resulting in the complex $Fe_{In}\bullet V_P\bullet P_{In}$ for the B configuration (Fig. 4). The B1 emission is attributed to the (=/-) transition of Fe_{In} and the B2 emission is the (0/+) transition of V_P. The results in the Table are found to be consistent with the predictions of the model and with first-principles calculations for the appropriate defects in InP.

Significance—Configurational bistability is undoubtedly a manifestation of strong electron-lattice interactions and accompanying large lattice relaxations. By pressure we can continuously tune the strength of these interactions and thereby modify the balance of forces that determine the stability and nature of the different configurations. The present results attest to the value of the pressure variable.

*In collaboration with C.E. Barnes, Jet Propulsion Laboratory
Sponsors for various phases of this work include: Nuclear Weapons/Science & Technology

Contact: G. A. Samara, Physics & Chemistry of Materials, Dept. 1130
Phone: (505) 844-6653, Fax: (505) 844-4045, E-mail: gasamar@sandia.gov

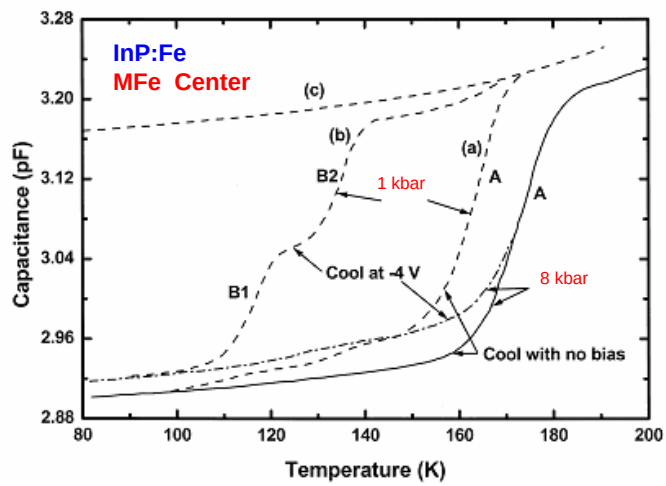

Figure 1. Thermally-Stimulated Capacitance (TSCAP) spectra for the A and B configurations of the MFe center in InP at 1 bar and 8 kbar.

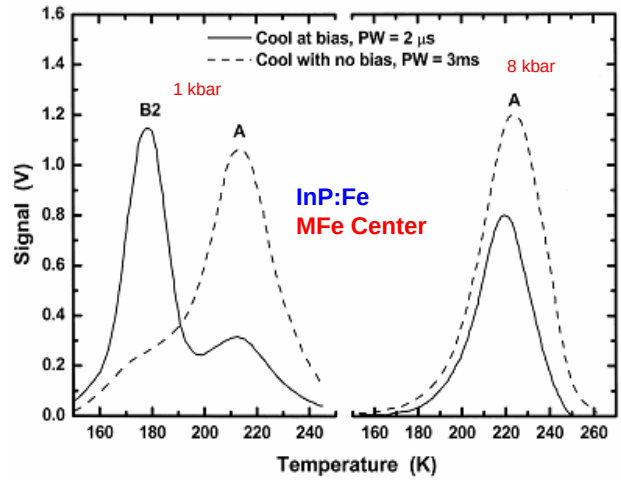

Figure 2. DLTS spectra for the A and B configurations of the MFe center in InP at 1 bar and 8 kbar. The B1 transition is not seen for the conditions of this experiment.

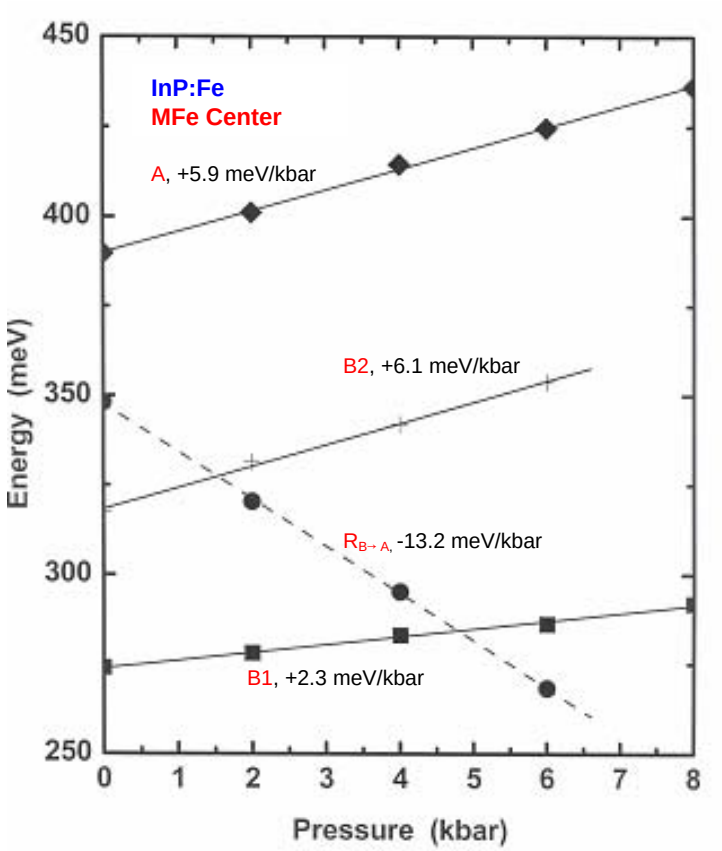

Figure 3. Pressure dependences of the measured electron emission enthalpies, ΔH_n, for the A, B1 and B2 deep levels of the MFe center in InP and of the enthalpy (or activation energy) for the $B \rightarrow A$ transformation.

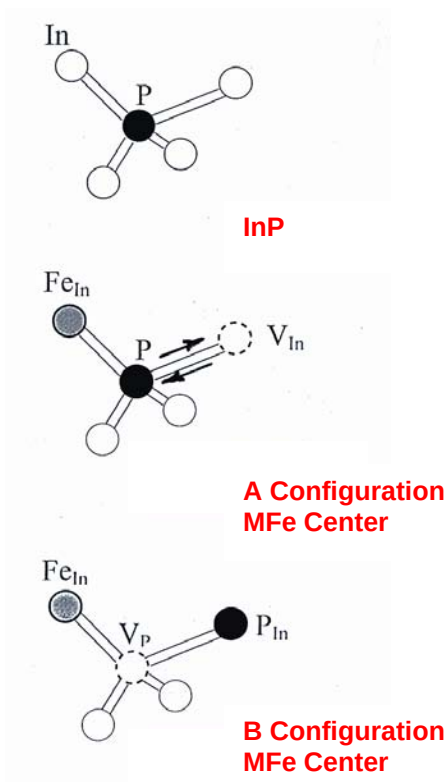

Figure 4. Atomic configurations of InP and of the A and B configurations of the MFe center according to the model described in the text.

Terahertz Radiation Science & Technology

Expanding the Operating Range of Terahertz Quantum-Cascade Lasers

by ***J. L. Reno***

Motivation—Terahertz (1-10 THz, or 4-40 meV, or 30-300 μm) frequencies are among the most underdeveloped portions of the electromagnetic spectrum. This is surprising since they are promising for spectroscopy in chemistry and biology, detection of trace gas for military and security applications, astrophysics, plasma diagnostics and end-point detection in dry etching processes, and remote atmospheric sensing and monitoring. In addition to diagnostic and sensing applications, they are of interest for imaging, noninvasive inspection of semiconductor wafers, high-bandwidth free-space communications, and ultrahigh-speed signal processing. This underdevelopment is primarily due to the lack of coherent solid-state THz sources that can provide high radiation intensities (greater than one mW) and continuous-wave (CW) operation.

Semiconductor quantum wells are human-made quantum-mechanical systems in which the energy levels can be designed and fabricated to be any value. Consequently, unipolar lasers based on intersubband transitions (electrons that make lasing transitions between subband levels within the conduction band) were proposed for long-wavelength sources as early as the 1970s (Kazarinov & Suris, 1971). However, because of the great challenge in epitaxial material growth and the unfavorable fast nonradiative relaxation rate, it took more than two decades to realize this proposal experimentally. Electrically pumped unipolar intersubband-transition lasers [also called quantum-cascade lasers (QCL)] at ~4-μm wavelength were first developed at Bell Laboratories in 1994 (Faist, *et al.*, 1994). Since then, the frequency characteristics have been extended from mid-infrared frequencies to the terahertz range.

Accomplishment—In collaboration with the group at MIT led by Qing Hu, we have continued to expand the operating range of QCLs at THz frequencies. The structures are all grown by molecular beam epitaxy on a semi-insulating GaAs substrate with 150 to 225 cascaded modules. The devices are then fabricated into ridge structures with a metal-metal waveguide. Both the range of operating temperatures and the frequency range have been expanded. We have used fast LO-phonon scattering to depopulate the lower radiative level (Xu, *et al.*, 1997; Williams, *et al.*, 1999), and double-sided metal waveguides for THz mode confinement (Xu, 1998). We have expanded the temperature range to the point where THz QCLs now operate in CW mode up to 97K and in pulsed mode up to 137K. The spectra of such a laser are shown in Fig. 1. We have achieved lasing from about 4THz down to 2.1THz. The spectra of a laser operating at 2.1THz are shown in Fig. 2.

Significance—To use QCLs as compact, coherent THz sources in applications, the operating temperature must continue to be raised and the frequency range expanded. We have extended both these ranges for lasing in resonant phonon terahertz QCLs by improving device design and reducing waveguide losses. New laser designs are being investigated along with improvements in metallic wafer bonding and heat sinking to further expand the useful range for THZ QCLs and to allow for robust CW operation.

Sponsors for various phases of this work include: Nuclear Weapons/Science & Technology

Contact: John Reno; Semiconductor Material & Device Sciences, Dept. 1123
Phone: (505) 844-9677, Fax: (505) 844-3211, E-mail: jlreno@sandia.gov

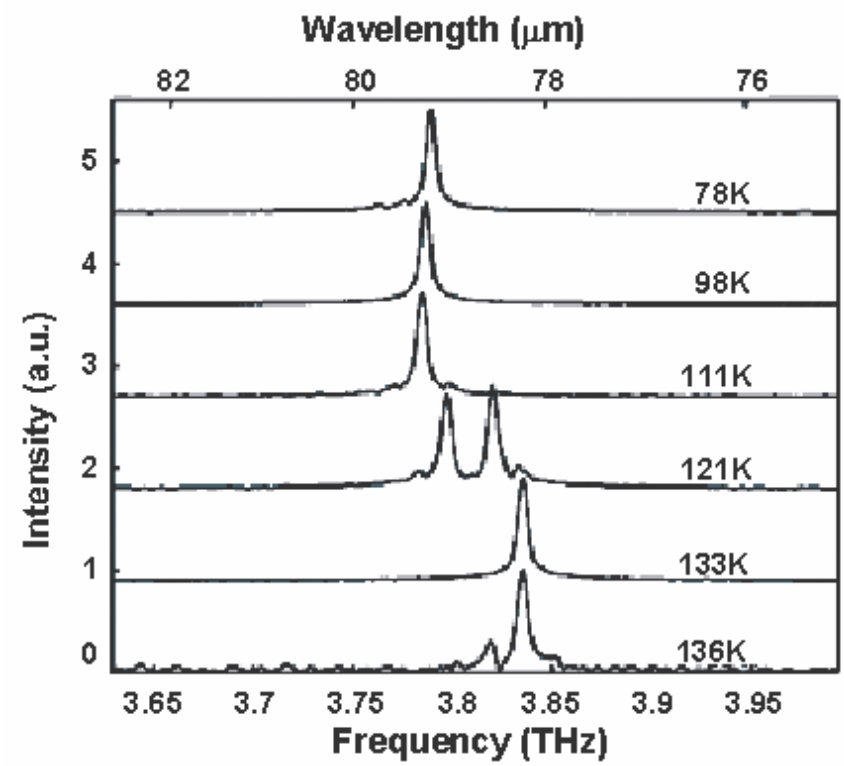

Figure 1. Laser emission spectra taken during pulsed operation at various heat sink temperatures. The linewidth is limited by the spectrometer resolution.

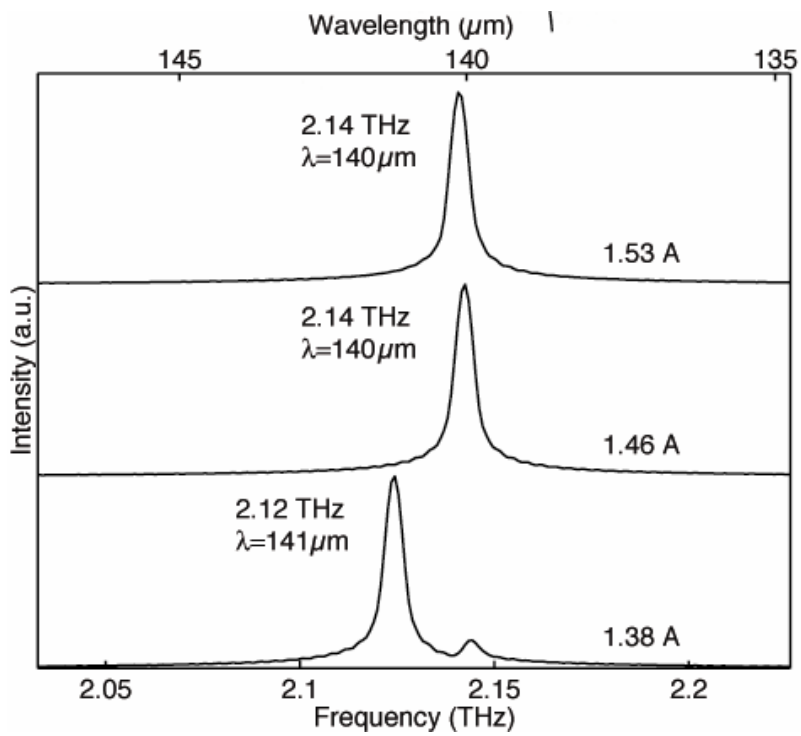

Figure 2. Laser emission spectra taken during pulsed operation at various operating currents. The linewidth is limited by the spectrometer resolution.

Millimeter Wave Mixing Using Plasmon and Bolometric Response in a Double-quantum-well Field-effect Transistor

by Mark Lee, Michael C. Wanke, and John L. Reno

Motivation—Coherent charge density oscillations (plasmons) in a high-mobility two-dimensional electron gas (2DEG) can be exploited to circumvent physical limits on maximum operating frequency in conventional electron-drift transistors. This speed increase arises from the fact that 2DEG plasmons have velocities ten times faster than electron drift. Typical 2DEG densities from 10^{10} to 10^{12} cm^{-2} yield plasmon frequencies in the 100 GHz to 1 THz range, making plasmon devices attractive for THz applications. The ability to electrically tune the density and hence the plasmon resonance via a gate voltage in a field effect transistor (FET) offers highly desirable new functionalities, such as "spectrometer-on-a-chip" capability.

Accomplishment—We have conducted the first experimental measurements on heterodyne mixing in a plasmon-based device. The mixer is a grating-gated GaAs-AlGaAs double quantum well (DQW) FET designed to have plasmon resonances from 100 to 200 GHz. Mixing is found to have two distinct regimes dependent on gate bias. Close to pinch-off the device exhibits a broadband response which is well-described as a bolometer. The conducting regime shows a gate-tunable plasmon resonance that has more complicated nonlinear behavior than a bolometer. The difference frequency (IF) or signal bandwidth can be fairly wide, > 2 GHz.

Figure 1 shows the detection responsivity vs. gate bias V_g at 94, 135, and 145 GHz. Two response regimes are evident. Above pinch-off, a resonant response to 145 GHz is at $V_g = -2.11$ V, the signature of a plasmon excitation. At more negative gate bias a partial resonance peak in response to 135 GHz is at $V_g \approx -2.25$ V. No resonance at 94 GHz is seen. At $V_g < -2.4$ V, all responsivity curves show a large rise that goes up to almost 50 V/W independent of frequency. The plasmon and pinch-off regimes have distinct mixing characteristics. Figure 2 shows spectra of the IF power for an 87 MHz difference frequency between two sources near 145 GHz. Figure 2(a) is with $V_g = -2.11$ V, the 145 GHz plasmon. A complicated series of harmonics of the IF is seen. Figure 2(b) is with the same parameters except $V_g = -2.42$ V, near pinch-off. Figure 2(b) consists almost solely of the fundamental IF with only a very small 2 IF distortion. It is clear that the IF generation mechanisms for the plasmon and pinch-off responses are fundamentally different.

Likewise, the IF bandwidth for plasmon mixing is distinctly different from the pinch-off response. Figure 3 shows the conversion gain η as a function of the IF. Figure 3(a) is taken at $V_g = -2.11$ V, on the 145 GHz plasmon. Here the IF bandwidth exceeds the 2 GHz instrumental limit. Figure 3(b) is again the same parameters except with $V_g = -2.42$ V, near pinch-off. Here the IF bandwidth can be fit to a Lorentzian with bandwidth of 620 MHz.

Significance—Development of electronics for very high frequency applications significantly above 100 GHz presents a basic challenge to solid-state physics because electron transit and scattering times are too slow to follow such rapidly oscillating fields. We have shown definitively that plasmon excitations in a high-mobility 2DEG heterostructure have great potential as the basis for fast, wide signal bandwidth, frequency-agile electronics in the 100 GHz to 1 THz frequency range.

Sponsors for various phases of this work include: Laboratory Directed Research & Development, Defense Advanced Research Projects Agency, and Other Federal Agency Work for Others

Contact: Mark Lee; Semiconductor Material & Device Sciences, Dept. 1123
Phone: (505) 844-5462, Fax: (505) 844-4045, E-mail: mlee1@sandia.gov

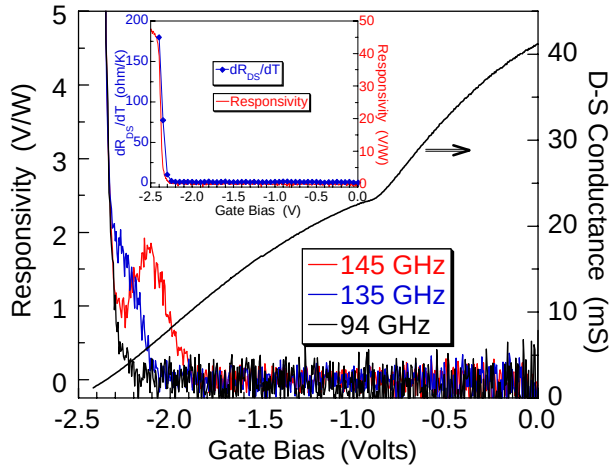

Figure 1. Drain-source conductance and responsivity in response to 94, 135, and 145 GHz as a function of V_g. Inset: 94 GHz responsivity and temperature slope of the drain-source resistance.

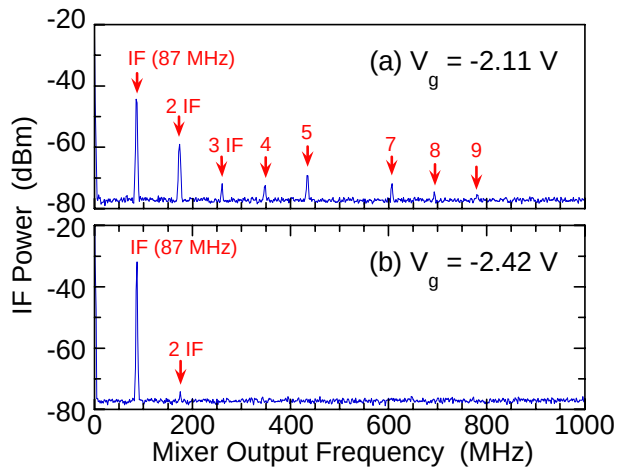

Figure 2. Spectrum of the IF an 87 MHz difference frequency between two sources near 145 GHz. In (a) V_g is held at the 145 GHz plasmon, while in (b) V_g is held in the pinch-off response.

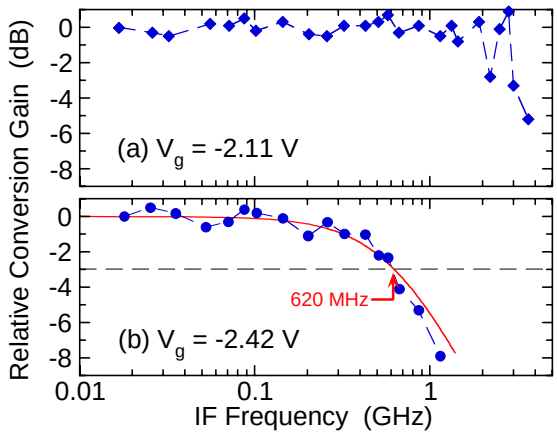

Figure 3. Mixer conversion gain bandwidth. In (a) V_g is held at the 145 GHz plasmon while in (b) V_g is held in the broadband pinch-off response. The red curve in (b) is a fit using a Lorentzian.

Applications for Terahertz Time-domain Spectroscopy

by ***R. Foltynowicz***

Motivation—Terahertz (THz) spectroscopy is emerging as a powerful technique to identify and characterize molecular species. Due to recent advances in femtosecond lasers and optical materials, the THz radiation band from 0.1 to 10THz is now routinely accessible. Spectroscopically, this is a new and unexplored portion of the spectrum that is rich in unique molecular information. As such, progress in this area requires fundamental measurements to determine molecular constants and extensive development of source and detector technologies. The fundamental work is closely tied to applications, which include sensing bio-chem agents, explosives, and byproducts of weapons of mass destruction (WMD) production. Our research interest lies in establishing a THz spectroscopy capability at Sandia to do fundamental spectroscopic characterizations of materials and to determine the feasibility of proposed THz applications that would be in the interest of our national security.

Accomplishment—We have built the first THz time-domain spectrometer at Sandia. Figure 1 shows a diagram of the experimental setup. THz generation is produced by optical rectification of an 800nm femtosecond laser pulse in a <110> ZnTe crystal. This process generates a broadband THz pulse with ~1ps period. The THz beam is detected via electro-optic sampling, which exploits induced polarization changes of the probe beam due to the THz interaction within a ZnTe crystal sensor. The polarization changes are proportional to the strength of the THz electric field; hence we measure the electric field strength of the THz radiation as a function of delay time. Currently, the detector bandwidth is 0.52 to 2.6THz with a spectral resolution of 1GHz (0.03 cm^{-1}). The spectral bandwidth is limited by laser power and crystal thickness. In the near future, we will integrate a regenerative amplifier with the THz spectrometer to produce high-energy THz pulses that will cover the entire THz bandwidth from 0.1 to 10THz.

Utilizing this spectrometer we measured the absorption spectrum of atmospheric water vapor shown in Fig. 2. If we are to conduct any type of molecular sensing through the atmosphere, it is important to know our background absorption. The measured data shows water resonances together with the transmission windows. In addition, we have observed and measured new water transitions. The majority of our measured lines match very well with published literature and NASA's JPL database. These same techniques and experimental configuration can be used to measure the absorption spectrum of a wide range of gases.

Significance—It is important to fully understand atmospheric water vapor resonance and non-resonance absorption behaviors if we want to do any type of remote or local sensing of molecules. Our results provide a map of the background absorption from the atmosphere as well as transmission windows. Having this information allows us to concentrate our molecular identification in the transmission windows. Next, we intend to measure spectral signatures of bio-chem, explosives, and WMD production byproducts and determine if any resonances lie in the atmospheric transmission window. Finally, we can prove the feasibility of molecular sensing through the atmosphere by determining if the line densities in the atmospheric windows are dense and specific enough to identify the molecule.

Sponsors for various phases of this work include: Nuclear Weapons/Science & Technology, Laboratory Directed Research & Development, and Work For Others

Contact: Robert Foltynowicz; Lasers, Optics, & Remote Sensing, Dept. 1128
Phone: (505) 844-8148, Fax: (505) 844-5459, E-mail: rjfolty@sandia.gov

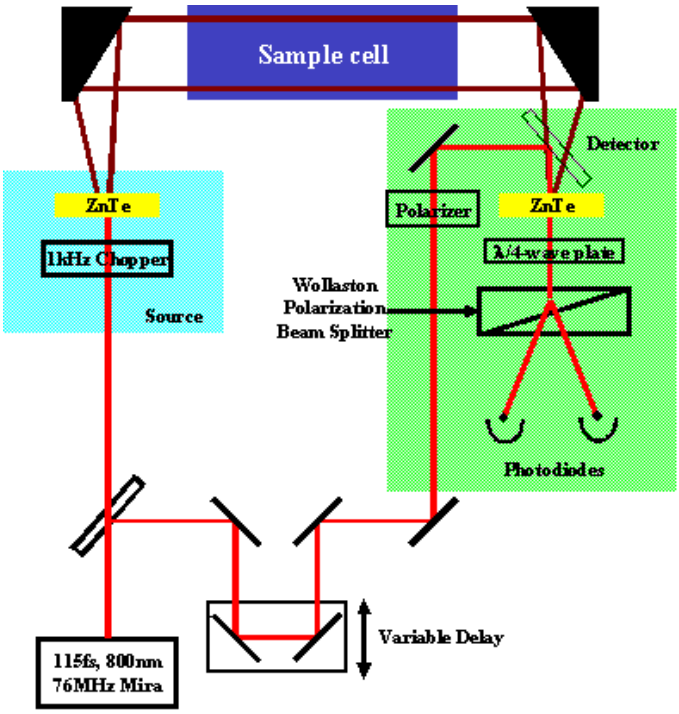

Figure 1. Diagram of the THz time-domain spectrometer. Femtosecond laser pulses chopped at 1KHz pump a <110> ZnTe crystal to produce THz radiation. The THz beam travels through the sample cell and collinearly propagates with an 800nm probe beam with horizontal polarization through a ZnTe sensor. The THz electric field strength is detected via polarization changes induced in the probe beam by the THz beam, inducing a change in the birefringence of the ZnTe sensor.

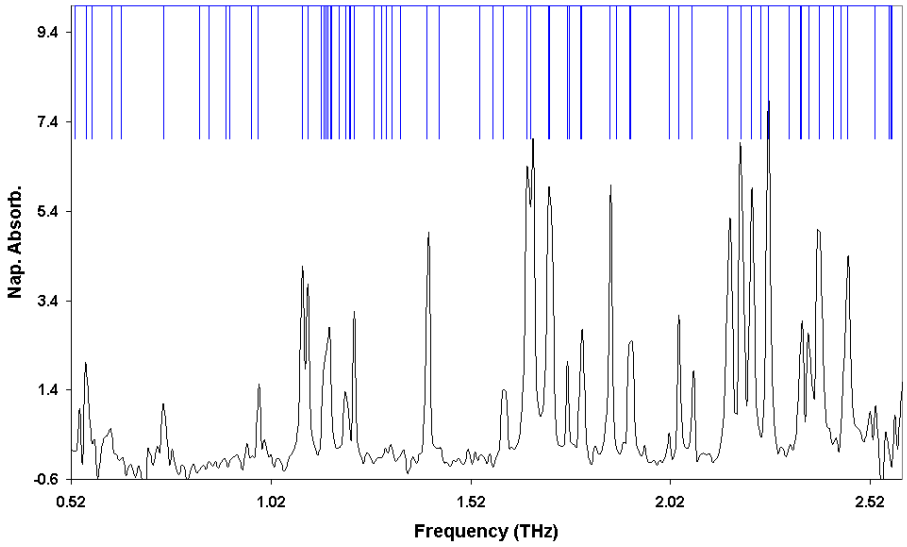

Figure 2. Water vapor absorption spectrum from 0.520 to 2.6THz. The blue ladders represent published lines in NASA's JPL database.

Science for Solid State Lighting

Cantilever Epitaxy of GaN Receives R&D100 Award

by ***D. M. Follstaedt, C. C. Mitchell, A. A. Allerman, D. D. Koleske, K. H. A. Bogart, A. J. Fischer, N. A. Missert, C. I. H. Ashby, P. P. Provencio, J. J. Figiel, K. W. Fullmer, K. C. Cross, M. P. Moran, A. K. Norman, G. M. Peake, L. Griego, A. Ongstad, and J. Sergeant***

Motivation—The semiconductor GaN has a large bandgap that allows optical emission in the visible and UV ranges by using its alloys with In and Al. Although GaN wafers are not available for device processing (like widely used Si wafers), GaN can be grown on sapphire and SiC wafers. However, the atomic spacing of GaN does not match these substrates, causing high densities of dislocation defects in the GaN that directly reduce optical emission. It is therefore important to reduce dislocation density to enable efficient light emission. Optical emission from GaN is thought to have the potential to provide general illumination with 50% efficiency, which could reduce U.S. electricity use by up to 10%.

Accomplishment—Our development of cantilever epitaxy (CE) to grow GaN with low dislocation density is described in previous *Physical and Chemical Sciences Center Research Briefs* (2001, p. 74; 2002, p. 18; and 2003, p. 20). This method minimizes the contact area of GaN on sapphire that produces these defects by nucleating the GaN on narrow mesas and growing it laterally over trenches as in Fig. 1. Adjacent cantilevers are grown together to coalesce into a uniform solid. After basic advantages of CE were identi-fied, we showed that remaining dislocations could be further reduced by turning them from vertical to horizontal and by identifying growth methods producing inherently fewer defects. However, we also found new non-radiative centers called "dark-block defects". These defects were caused by tilted cantilevers that did not coalesce properly, leaving cracks with additional dislocations around them. The defects were eliminated by increasing the nucleation density, by increasing the trench depth, and by controlling the facets on cantilever faces.

To determine the density of remaining dislocations accurately, we developed special imaging techniques for transmission electron microscopy to assure that all dislocations were detected. When used with scanning cathodo-luminescence and atomic-force microscopy images, our final dislocation density can be confidently stated as $2\text{-}5\times10^{7}/\text{cm}^{2}$. This is an order of magnitude or more below that for conventional planar growth of GaN on sapphire. The low density improves the output of light-emitting diodes (LEDs). Fig. 2 shows maps of the photo-luminescence output from identical InGaN quantum wells grown on two half wafers of GaN, one grown by CE and the other by conventional planar growth. The greater intensity from the CE GaN wafer directly demonstrates that dislocations reduce light emission and that cantilever epitaxy can increase the light output of LEDs.

Significance—The importance of CE GaN is demonstrated by our receiving a 2004 R&D 100 award for its development. Winning this award required not only technical achievement, but demonstration of commercial viability as well. Cantilever epitaxy has the advantage that once the trenches are patterned into the wafer, the GaN layer and LED structure can be formed with only one metallorganic chemical vapor deposition (MOCVD) growth. Competing schemes for reducing dislocations require multiple growths or very thick growth; both are more expensive and have other disadvantages. Thus CE GaN could enable economically the widespread use of solid-state lighting needed to achieve significant energy savings. Low-defect GaN appears potentially important for high-frequency electronic devices also.

Sponsors for various phases of this work include: DOE Office of Basic Energy Sciences, DOE Office of Energy Efficiency & Renewable Energy, Laboratory Directed Research & Development, and Nuclear Weapons/Science & Technology

Contact: David M. Follstaedt; Radiation-Solid Interactions, Dept. 1111
Phone: (505) 844-2102, Fax: (505) 844-7775, E-mail: dmfolls@sandia.gov

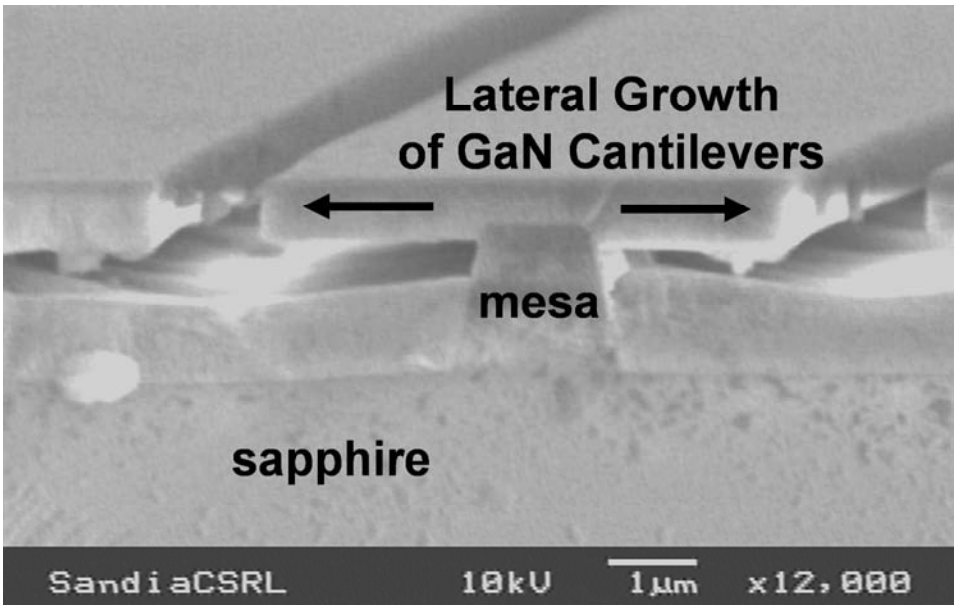

Figure 1. Cross-section scanning electron micrograph showing GaN growing off sapphire mesas and over trenches toward adjacent GaN cantilevers. Some GaN also grows in trenches between mesas.

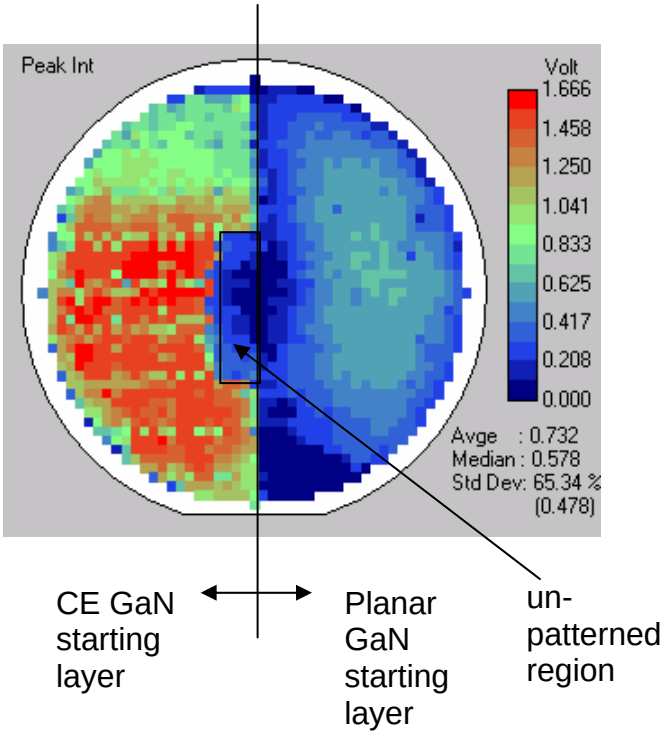

Figure 2. Photoluminescence map showing the intensity of emitted light from CE GaN (left) and conventionally grown planar GaN (right) when irradiated with a 325 nm HeCd laser. Both half-wafers were identically processed to form optically emitting InGaN quantum wells for LEDs. The light emission from CE GaN is 2 to 3 times brighter. (Data courtesy of Lumileds Lighting).

Interaction of Magnesocene ($MgCp_2$) and Ammonia (NH_3) Explains "Memory Effects" during p-Type Doping of Group-III Nitrides

by G. T. Wang and J. R. Creighton

Motivation—Magnesocene [$Mg(C_5H_5)_2$ = $MgCp_2$] is the dominant precursor used for the p-type doping of GaN and its alloys in the AlGaInN system (III-nitrides). Unfortunately, difficulties remain with predictably controlling the incorporation of Mg during metal organic chemical vapor deposition (MOCVD) film growth, which often exhibits poorly understood "memory effects." The electron deficiency of the Mg center in $MgCp_2$ suggests that it may be susceptible to nucleophilic attack by NH_3, resulting in the formation of condensable Lewis acid-base complexes (adducts). An improved understanding of the interaction between $MgCp_2$ and NH_3 could shed light into the p-type doping issues.

Accomplishment—We have determined, for the first time, the details of the interaction between magnesocene and ammonia using a combined experimental and theoretical approach. Our results show that at room temperature $MgCp_2$ and NH_3 react to form the complexes NH_3:$MgCp_2$ and $(NH_3)_2$:$MgCp_2$. The formation and subsequent condensation of these low vapor pressure adducts is the probable source of parasitic Mg loss that results in the observed unpredictable Mg incorporation and slow turn-on and turn-off response during p-type doping of III-nitrides (i.e., the so-called memory effects).

The interaction between $MgCp_2$ and NH_3 at room temperature was investigated by FTIR spectroscopy and density functional theory (DFT) quantum chemistry calculations. Figure 1 summarizes the model developed, which is consistent with the observed and calculated chemistry. Upon mixing, $MgCp_2$ and NH_3 can undergo complexation to form a "1:1" NH_3:$MgCp_2$ adduct, which is calculated to have a binding energy of 5.4 kcal/mol (relative to the reactants). We calculated only a minor energy barrier to formation of 1.0 kcal/mol, indicating that the reaction should be facile at room temperature. Interestingly, the 1:1 adduct can undergo further complexation with a second NH_3 molecule to form a more stable "2:1" $(NH_3)_2$:$MgCp_2$ adduct. The 2:1 adduct has a binding energy of 12.3 kcal/mol and no significant energy barrier to form. Thus, equilibrium exists between $MgCp_2$, NH_3, and the 1:1 and 2:1 adducts which is dependent on the process conditions. We have confirmed this using *in situ* infrared spectroscopy experiments. Figure 2 shows the IR spectra of the 1:1 and 2:1 adducts condensed on a KCl window at room temperature, which can be isolated at low and high pressure (or NH_3 concentration), respectively. The calculated spectra for the complexes (overlaid as bars) show good agreement with the experimental data. Formation of both the condensable 1:1 and 2:1 adducts was found to be completely reversible at room temperature.

Significance—Due to our improved understanding of the interaction between $MgCp_2$ and NH_3, intelligent efforts to eliminate or minimize condensable adduct formation can now be undertaken. These efforts should lead to improvements in reactor design and performance with regards to the crucial issue of controlled p-type doping of III-nitride materials. This work was recently featured on the cover of, and as an article within, *The Journal of Physical Chemistry A* (June 3, 2004).

Sponsors for various phases of this work include: DOE Office of Basic Energy Sciences and Laboratory Directed Research & Development

Contact: George T. Wang; Advanced Materials Sciences, Dept. 1126
Phone: (505) 284-9212, Fax: (505) 844-3211, E-mail: gtwang@sandia.gov

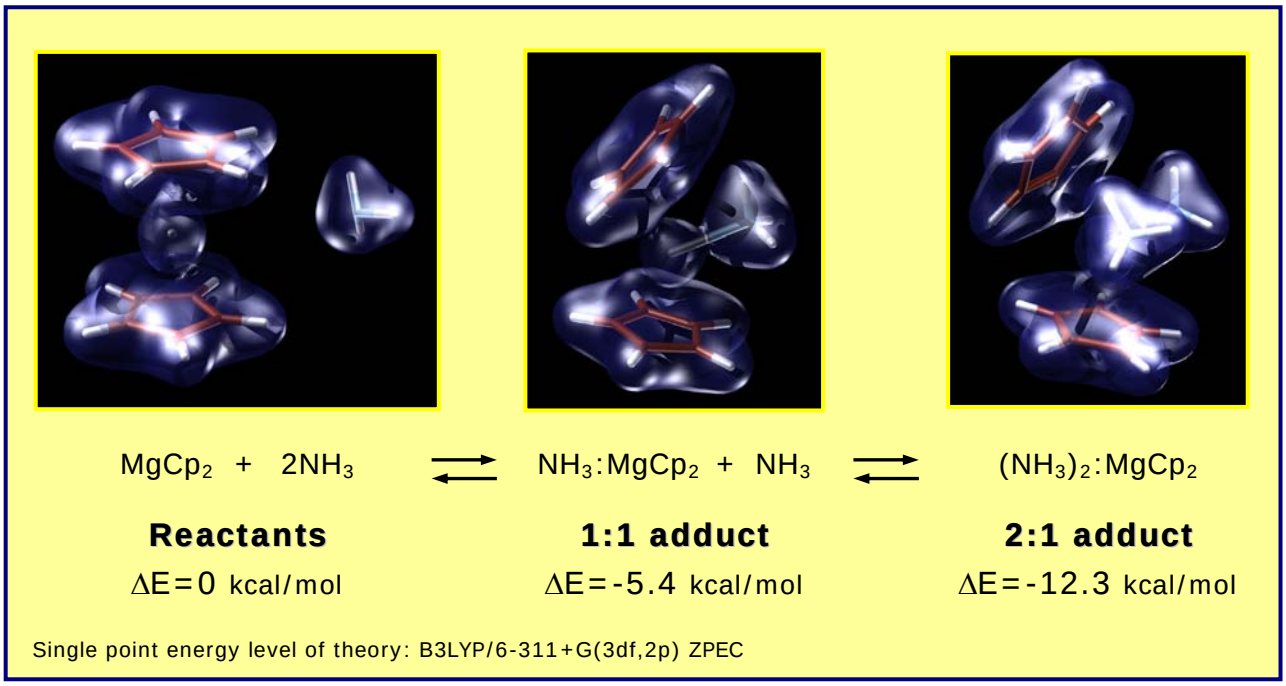

Figure 1. Model summarizing the interaction between magnesocene and ammonia, shown with calculated optimized geometries and energetics.

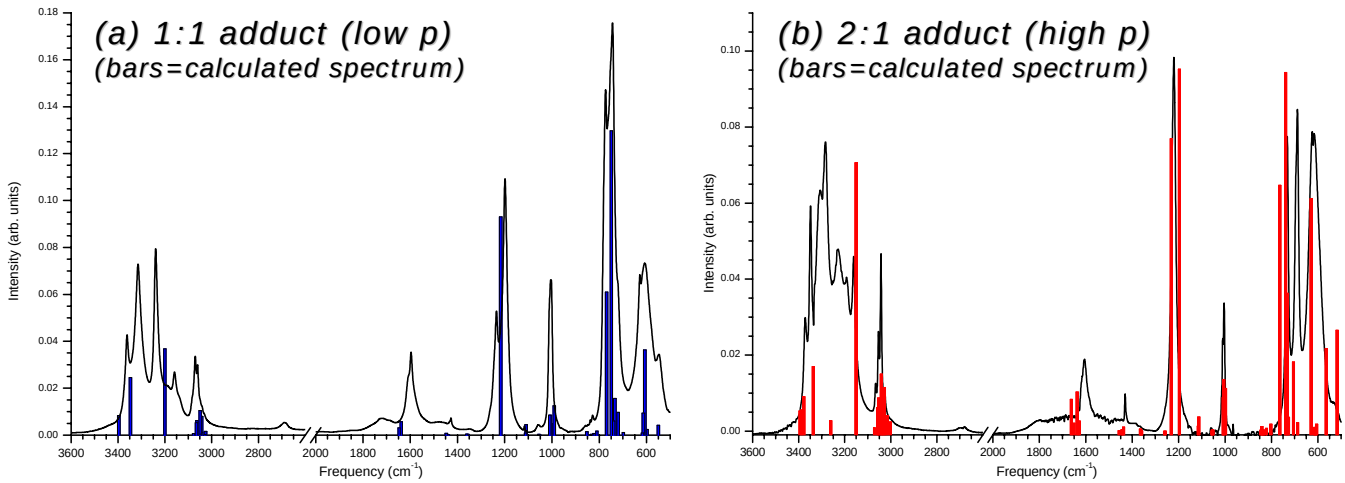

Figure 2. IR spectra of the condensed (a) 1:1 adduct and (b) 2:1 adduct at room temperature, with calculated spectra overlaid (bars).

Tunable Broad White Light Emission from Single Size Semiconductor Quantum Dots

by ***J. P. Wilcoxon, B. L. Abrams, and S.G. Thoma***

Motivation—The development of highly efficient GaN-based solid-state illumination sources requires new types of phosphors, which absorb near UV energy strongly while re-emitting visible, white light. Phosphors based on semiconductor nanoparticles offer advantages compared to conventional powder phosphors including negligible optical backscattering due to the small diameter of the dots. More importantly, we discovered that direct white emission from a single size dot is possible, obviating the need to blend two or more dots of differing size. Use of a single size dot eliminates self-absorbance of the emitted light at the high optical densities required for full absorbance of the excitation energy while maintaining optical transparency in the visible, 450 to 700 nm regime.

Accomplishment—We have demonstrated tunable broad white light emission from single size CdS semiconductor quantum dots (QDs) (see Fig. 2b). This accomplishment is made possible by our discovery that for sufficiently small CdS and CdSe quantum dots (QDs) of diameters ≤ 2 nm (or ~ 90 formula units) the onset of absorption (determined by quantum confinement, or dot size) and the emission energy, or color (determined by interfacial chemistry) can be independently controlled. The decoupling of these two features has allowed us to widely separate the absorption and emission to eliminate self-absorption of the emitted light and to tune the emission throughout the visible range from a population of single-size dots. In essence, these QDs behave much like organic laser dyes with significant adjustable Stokes shifts resulting in negligible self-absorption.

Key to this discovery is the ability to tailor the interface states of the QDs. This is accomplished in two ways during our inverse micellar synthesis and subsequent processing: (i) by the use of suitable surfactants that bind to selected sites on the QD surface causing changes in the energies and lifetimes of the interface states which determine the emission; (ii) the addition of surface active agents such as suitable electron or hole traps (e.g., by the addition of Zn^{2+} or excess S^{2-} ions, respectively) to a monodisperse population of CdS or CdSe QDs, which also tailor the emission.

Significance—Though quantum confinement of carriers by the finite size of a semiconductor QD can be used to adjust the color emitted, the overlap between absorbance and emission bands in the case of larger QDs leads to strong self-absorption of the emitted light (see Fig. 1). By synthesizing dots so small that a majority of their atoms are at the QD interface, the chemistry of this interface alone determines emission color, while the absorption is fixed by dot size. All the excitation light can then be converted to tunable, visible emission. Compared to conventional white light phosphors, our QDs can be selected by material type and size to have absorbance in the near-UV (360-420 nm) region, while conventional white light phosphors must be excited below 300 nm to emit in the visible (see Figs. 2a & b). This causes an inherently larger energy loss than excitation near 400 nm. The principles determining the optical properties of these new phosphors should extend to other nanosize semiconductors like Si, and, thus, these new nanomaterials have great potential as white phosphors for both solid-state lighting and fluorescence illumination devices.

Sponsors for various phases of this work include: DOE Office of Basic Energy Sciences and Laboratory Directed Research & Development

Contact: J. P. Wilcoxon; Advanced Materials Sciences, Dept. 1126
Phone: (505) 844-3939, Fax: (505) 844-4045, E-mail: jpwilco@sandia.gov

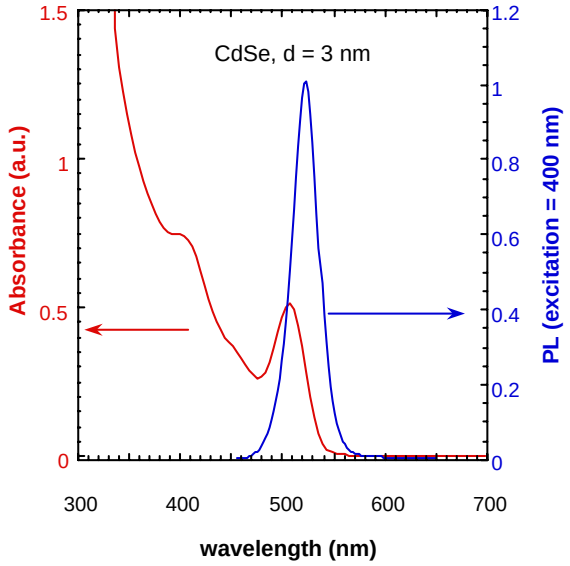

Figure 1. Strong overlap between **absorption** and **emission** leads to self-absorption in large Q dots.

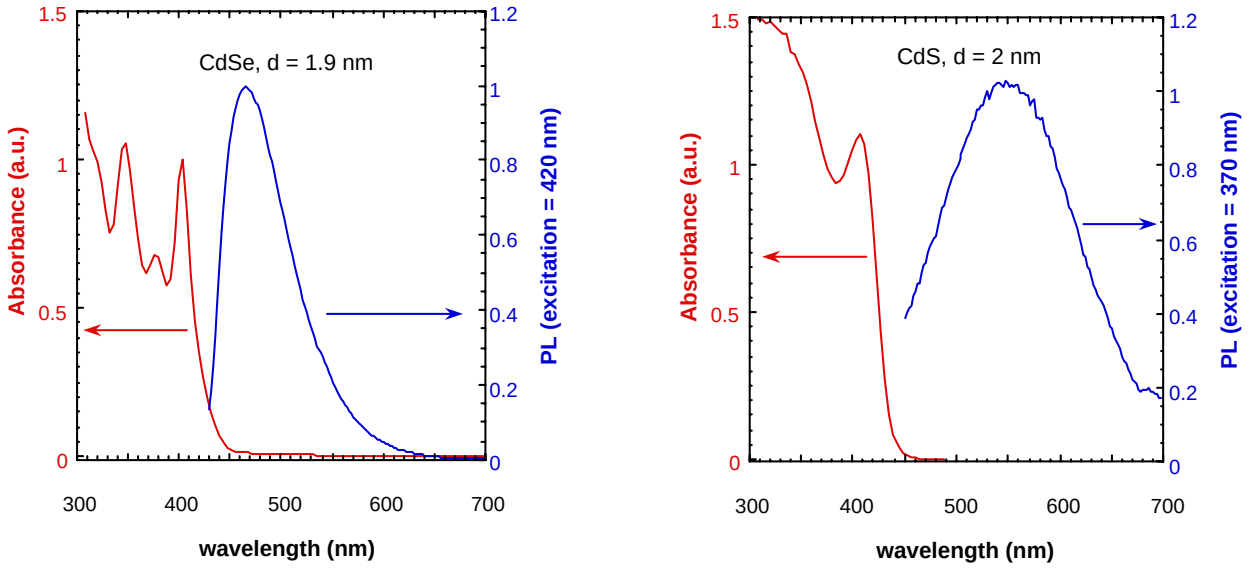

Figure 2. Significant Stokes shift in smaller Q dots results from decoupling of the **absorption** and **emission** and eliminates self-absorption. (a) CdSe, (b) CdS.

Mechanics of Materials and Systems

Mechanical Dissipation in Disordered Materials: Micro-scale to Nano-scale

by J. P. Sullivan, D. A. Czaplewski, T. A. Friedmann, N. A. Modine, D. W. Carr, B. E. N. Keeler, and J. R. Wendt

Motivation—Small mechanical oscillators are increasingly important for new technological areas, including clocks/filters for electrical circuits, mechanical-based detectors for chemicals/biological species, and scanning probes for force detection. The performance of these systems is limited by mechanical dissipation, 1/Q, where Q is the quality factor. Fundamental understanding of mechanisms that control dissipation in small oscillators is severely limited. Knowledge is especially lacking in mechanisms that control dissipation in disordered or amorphous materials. This work describes an experimental and theoretical effort aimed at understanding mechanical dissipation in oscillators of micron-scale to nanometer-scale dimensions.

Accomplishment—A variety of mechanical oscillators were fabricated out of one class of amorphous materials, tetrahedral amorphous carbon, ta-C [also termed "amorphous diamond," — see Fig. 1(a-c)]. These oscillators were created with dimensions ranging from many microns [1(a)] down to 10s of nanometers [1(c)], with designs that were chosen to minimize mechanical losses to the supports. The oscillator resonance frequencies ranged from about 1 kHz to over 10 MHz, permitting a study of time-dependent relaxation processes. Concurrent with these experimental activities, molecular dynamics theoretical simulations were performed on another class of amorphous materials, amorphous silicon, which was chosen for the availability of large, multi-atom theoretical unit cells [see Fig. 2 (inset)]. Dissipation in the theoretical system was identified through observation of the decay in amplitude of the lowest frequency vibrational mode in the system.

Experimental measurements of Q in ta-C oscillators revealed a nearly dispersionless dissipation (i.e., no frequency dependence). This dissipation differs from dissipation found in crystalline materials, which is often controlled by intrinsic processes, e.g., thermoelastic dissipation, or by specific defect relaxation processes, e.g., vacancy motion. In ta-C, the dissipation is controlled by a relatively flat spectrum (uniform concentration) of defects, and measurements of dissipation vs. frequency permit determination of the defect relaxation activation energies [see Fig. 1(d)]. Defect activation energies are small, which is consistent with local (non-diffusional) relaxation processes, but the exact nature of the dissipative defects is still to be determined. Theoretical simulations provided a unique view of dissipation in a model amorphous material. Low Qs were observed in amorphous Si, whereas Qs for simulations on crystalline Si were about 2 orders of magnitude higher. The dissipation in the amorphous silicon cell did not appear to be limited by a single specific defect; rather, the low phonon mean free path appeared to play a greater role. Studies using larger cells should offer even greater insight.

Significance—Studies of fundamental dissipation mechanisms in small oscillators will provide scientific understanding of the mechanical behavior of small (down to nano-scale) mechanical systems. This knowledge is critical for a number of revolutionary technologies, including single molecule/single spin detectors, systems of multiple miniature chemical or biological sen-sors, and high frequency oscillators for electronic signal processing.

Sponsors for various phases of this work include: Laboratory Directed Research & Development and DOE Office of Basic Energy Sciences

Contact: John P. Sullivan; Nanostructure & Semiconductor Physics, Dept. 1112
Phone: (505) 845-9496, Fax: (505) 844-1197, E-mail: jpsulli@sandia.gov

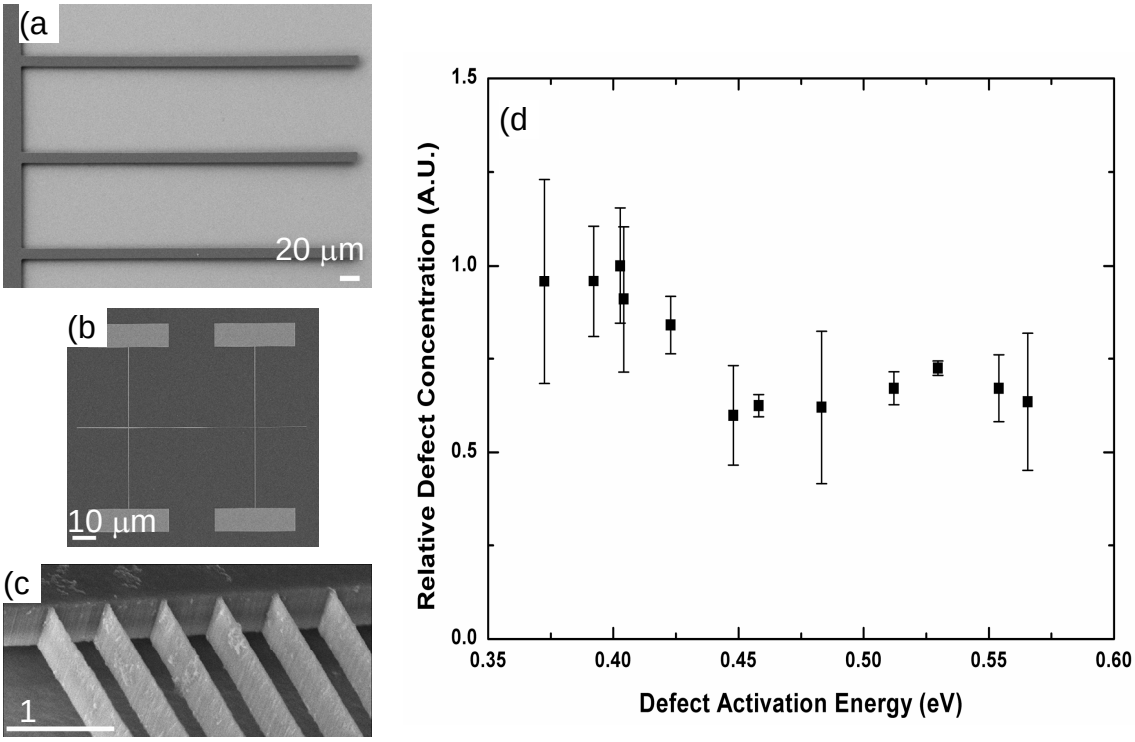

Figure 1. Tetrahedral amorphous carbon oscillators with microns to sub-micron dimensions (a-c), and (d) distribution of activation energies for the mechanically dissipative defects in this material.

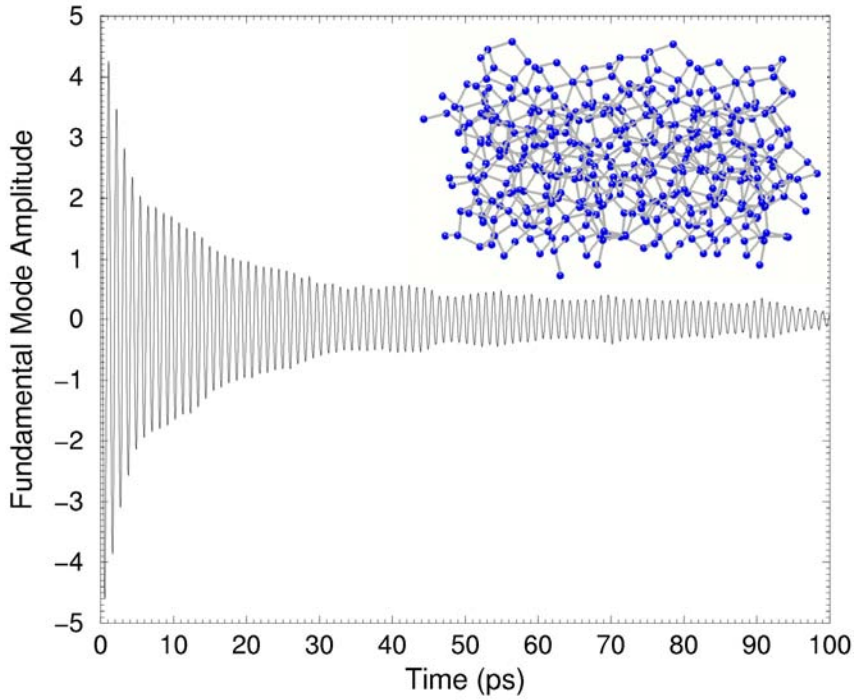

Figure 2. Computer simulation of mechanical dissipation of the lowest resonant mode of a 432 atom amorphous silicon cell (shown in inset). Q and f_0 are 3.6 and 943 GHz, respectively.

Island Coalescence Stress: Solving a 30-Year-Old Scientific Debate

by ***S. J. Hearne, S. C. Seel, J. A. Floro, C. W. Dyck, W. Fan, and S.R.J. Brueck***

Motivation—The effective mechanical proper-ties of a material are highly dependent upon the residual stress state introduced during fabrication. Unfortunately, the evolution of intrinsic stress during deposition of non-epitaxial thin films is quite complex and still highly debated. The only area where there is a consensus as to the mechanism is during island coalescence, where tensile stresses have been observed to exceed one gigapascal. Existing theoretical models for coalescence stress all determine the mean tensile stress in mechanical equilibrium, as a function of island size and geometry at the moment of coalescence. However, computational necessity requires the use of highly simplified island geometries with uniform sizes and simultaneous coalescence. In real films, coalescence events are stochastically distributed in time and occur among islands with a broad range of sizes and shapes. As a result, despite models having existed for over 30 years, it has not been possible to compare them quantitatively to measurements in stochastically-nucleated films.

Accomplishment—We have obtained, for the first time, both the functional dependence of the mean tensile stress on island radius, and the absolute magnitude of the stress during island coalescence. This was accomplished by meas-uring stress changes during electrodeposition of Ni islands where the coalescence process was constrained via lithographically-defined island nucleation sites and selective-area growth (Fig. 1). As shown in Fig. 2, by systematically varying the radius of the coalescing cylindrical islands over two and a half orders of magnitude, we demonstrated that the experimentally measured initial coalescence stress is in good agreement with the predictions from the recently developed Hertzian contact model of Freund and Chason (FC) [J. Appl. Phys. **89**, 4866 (2001)] and also with our two-dimensional finite element (FE) analysis. This agreement confirms that all of the dominant physical mechanisms in the initial island coalescence process are known and accounted for in the FC and FE models. Moreover, we have also determined that the initial coalescence stress is a minority component of the total stress created during the coalescence and planarization of the film. This striking result had not been previously observed in unpatterned metal films due to the inability to differentiate the stress created at the initial contact from that created during planarization.

Significance—The majority of thin films currently in use grow via an islanding mode, which invariably results in a tensile component in the stress. As the dimensions of these islands decrease into the nanometer regime, the coalescence stress can exceed a gigapascal, which impacts the effective materials properties. Therefore, the understanding of the stress evolution during the ubiquitous island coalescence process is crucial for nano-technologies. This work provides the founda-tion for understanding the physical processes active during the initial coalescence of islands and lays the groundwork for future analysis of the post-contact stress generation process, which is considerably more complex. This understanding will help make more reproducible microsystems from electrodeposited metals – like the components formed in precision molds by the LIGA process and metal MEMS structures used in RF communications.

Sponsors for various phases of this work include: DOE Office of Basic Energy Sciences, Laboratory Directed Research & Development, and Nuclear Weapons/Science & Technology

Contact: Sean J. Hearne; Nanostructure & Semiconductor Physics, Dept. 1112
Phone: (505) 845-0804, Fax: (505) 844-1197, E-mail: sjhearn@sandia.gov

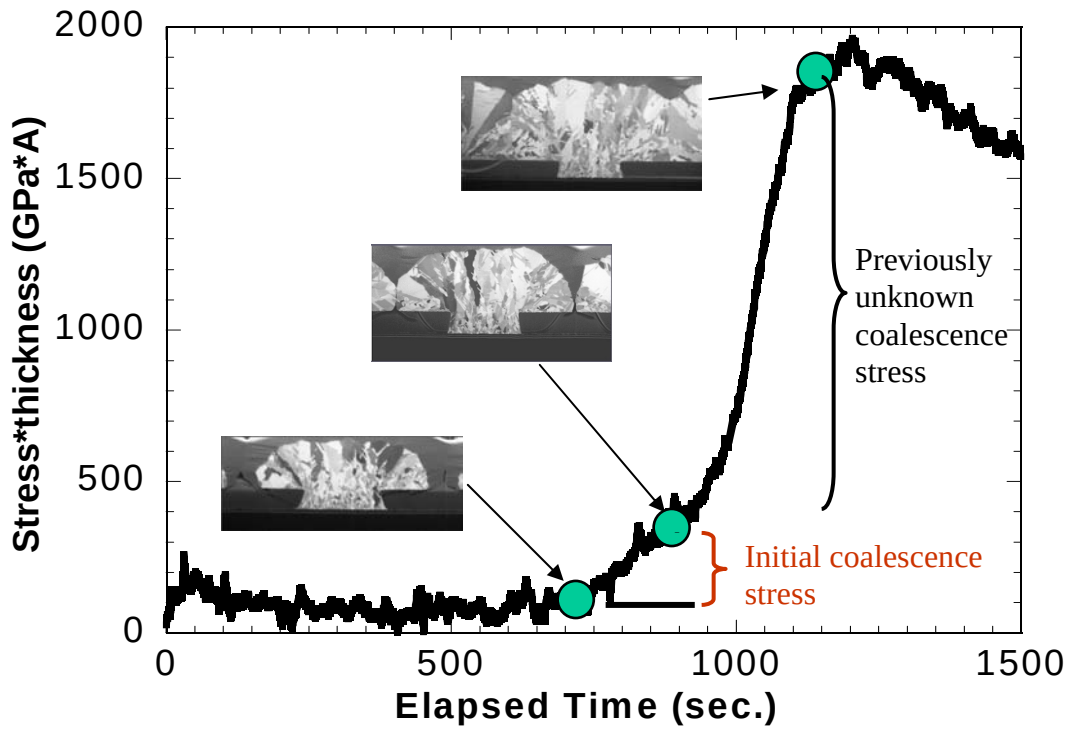

Figure 1. Plot of the stress evolution observed during electrodeposition of Ni onto a patterned substrate. Insets are cross-sectional focused ion beam (FIB) images of islands during the pre-coalescence, initial coalescence, and planarization stages of growth.

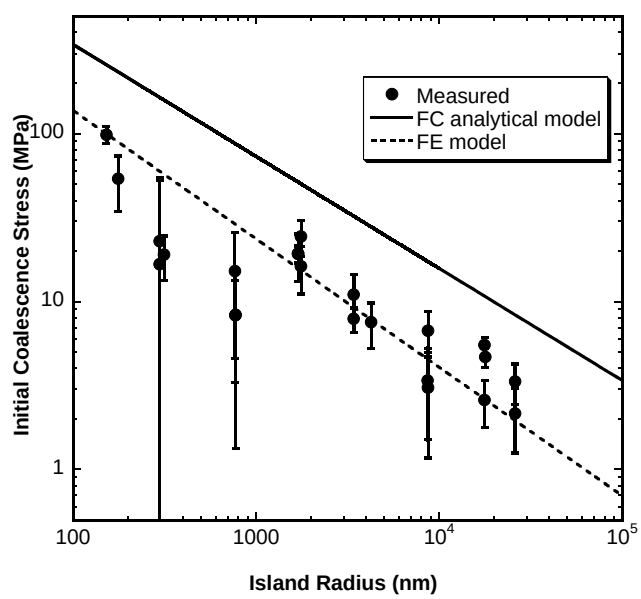

Figure 2. Plot of measured, Freund-Chason Hertzian contact (FC), and finite element (FE) calculated island coalescence stress as functions of radius. The plot demonstrates the excellent agreement between theory and experiment over two orders of magnitude.

Shear in Granular Couette Cells

by Jeremy B. Lechman and Gary S. Grest, Sandia National Laboratories
Antonio Barbero, Heinrich Jaeger, and Sidney R. Nagel, University of Chicago

Motivation—Slow flows in dense granular materials are of practical concern in a variety of applications such as soil failure and powder processing but are still poorly understood. While progress has been made in understanding rapid flows in terms of kinetic theory, the nature of slow flows limits the use of such approaches. These denser systems often exhibit thin, localized regions of particle motion, shear bands, separating largely solid-like, immobile regions. To understand the flow in dense granular materials, we carried out a combined experimental and simulation study of flow in a split-bottom Couette cell as shown in Fig. 1. Unlike traditional Couette cells with an inner wall that is rotated, an inner ring on the bottom of the cell is used to shear the system. This eliminates the need for an inner wall, which can have a strong effect on the size of the shear zone.

Accomplishment—Using our parallel discrete element simulation code, it is now possible to model the same system sizes as in the experiment. As the fill height H of the particles in the cell increases, the width of the shear band increases and moves away from the outer wall. In Fig. 2, results for the azimuthal surface velocity in piles of various heights from both experiments using glass beads and discrete element simulations are shown. Similar results are found from simulations for the azimuthal velocity as a function of depth within a given pack. Moreover, these azimuthal velocities can be rescaled to fall on a universal curve regardless of the particle properties. This universal curve is in excellent agreement with both experiment and the simulation. The shape of this universal curve is slightly asymmetric. We are presently investigating the origin of this asymmetry.

When shearing shallow packs (R_s<H/2) the simulations exhibit an inner region which moves along with the bottom disk in a nearly solid-like fashion, while the region between this inner core and a few particles lining the outer wall is fluidized. Snapshots of this inner core are shown in Fig. 3 by removing the "flowing" particles. Note the change in the shape and width as the height of the pile increases. For higher piles, this inner solid-like region disappears, as evident from Fig. 2. The shape of this inner core is in qualitative agreement with a simple theoretical model based on Janseen's 1895 model of shear stresses in granular silos, which we investigated in previous studies. These results are also in agreement with nuclear magnetic resonance (NMR) experiments using mustard seeds instead of glass beads to provide the required signal.

Significance—Using a new type of shear cell, we are able to study the development of the shear zone in dense granular flows. The new cell has several advantages over the standard Couette cell. The width of the shear zone can grow arbitrarily large without interference from the boundaries, and the velocity profiles have a universal character independent of particle properties. This suggests that in a single system access to a range of flowing states can be gained, and fundamental questions about the nature of dense granular flow can be addressed. Thus, the new geometry allows more precise measurement of the particle fluctuations which can be tracked either visually from motion on the surface or in the bulk by NMR. The simulations complement the experiments and give more detailed information on the structure of the pack and stresses than can be obtained experimentally. Future work includes studying the effect of cohesive interactions, such as moisture, on the shape of the shear zone.

Sponsors for various phases of this work include: DOE Office of Basic Energy Sciences

Contact: Gary S. Grest; Surface & Interface Science, Dept. 1114
Phone: (505) 844-3261, Fax: (505) 844-1197, E-mail: gsgrest@sandia.gov

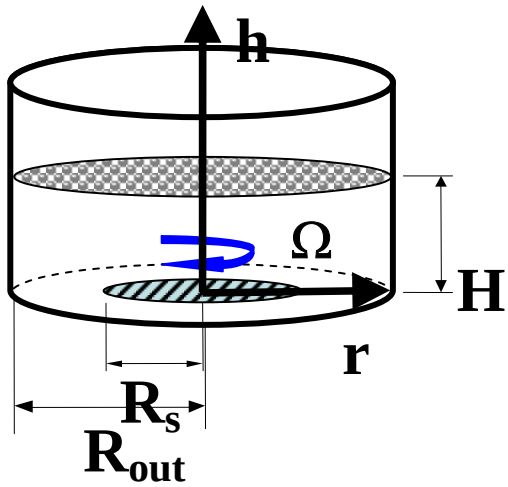

Figure 1. Schematic of split-bottom Couette system; only the inner plate of radius R_s rotates. For the results presented here R_s=30d and R_{out}=39d, where d is the particle diameter.

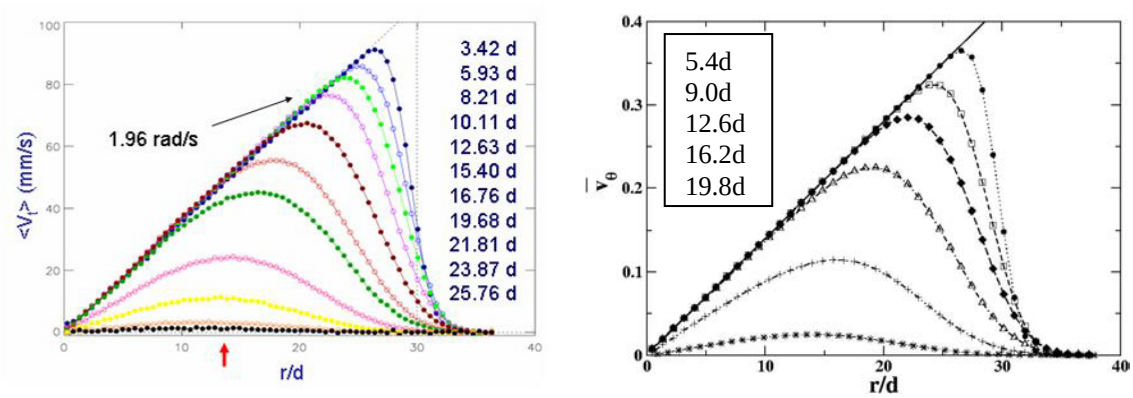

Figure 2. Azimuthal surface velocity profiles for packs of varying height, experiment result for glass beads (left), simulation (right)

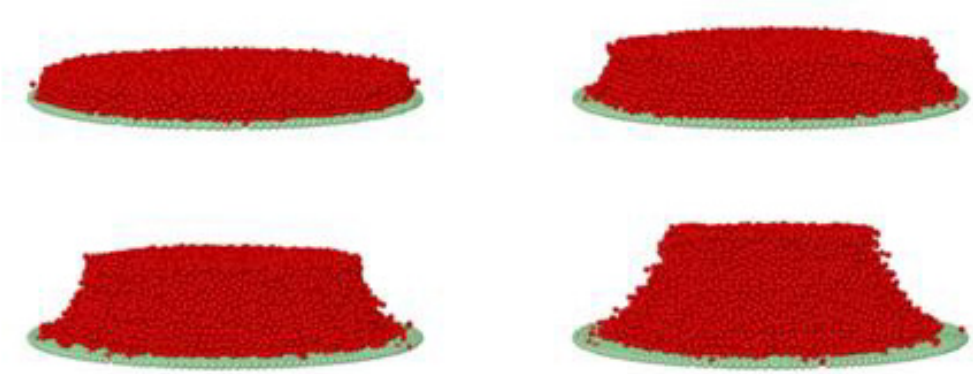

Figure 3. Snapshot of static inner core (red) particles determined by selecting particles which after ~1/4 revolutions had moved less than 0.005d in both h and r directions. Heights of the pile are 5.4, 9.0, 12.6 and 16.2d, where d is the diameter of a particle.

Nanoscale Studies of Surfaces

Implications of Spectroscopic Measurements of an Ultrathin Water Layer

by ***Peter J. Feibelman***

Motivation—Many examples teach that the structure of an adsorbed layer is not understood without confirmation from several experimental approaches. Thus, our inference that water forms a partially-dissociated wetting layer on the close-packed face of ruthenium [Science **295**, 99(2002)], based on successful comparison of ab initio calculations to low energy electron diffraction (LEED) structure analysis, has recently been subjected to spectroscopic tests. The vast importance of water behavior within microns of surfaces, in technology (membranes, sensors, micromachines) and nature (bio-transport, geophysical transport, raindrop formation), and the knowledge that the first water layer on a solid is a "template" determining the behavior of adjacent water over microns, has made it urgent to confirm or disprove that wetting and H_2O dissociation go hand-in-hand.

Accomplishment—Vibrational and X-ray photoelectron spectroscopies have been applied (by experimentalists in Germany, Sweden, England and the U.S.) to the water-on-ruthenium system, and we have performed first-principles calculations of the expected spectra, for both dissociated and undissociated cases, to guide the interpretation of the results, leading to a vigorous debate in the literature.

New spectroscopic data first emerged from non-linear optics ("Sum Frequency Generation") coupled with thermally programmed desorption. Supporting dissociation, absence of a high-frequency stretching vibration mode implied that all the hydrogens of the wetting layer were involved in H-bonding. For a layer of intact water molecules (Fig. 1), this would not be the case. But the new data also appeared to show a spectral peak at a frequency characteristic of water. We clarified the meaning of this result, producing new and marshalling old evidence that the stretch vibrations of an H-bonded system reveal the O-O distance distribution, not whether its molecules are intact or dissociated. We also estimated the breadth of the O-O distance distribution for the expected level of proton disorder, showing that it agrees both with the width of the observed vibration peak and also a new electron diffraction analysis.

New, low-fluence, high-resolution X-ray photo-electron spectra (Fig. 2) reveal an O (1s) feature with two peaks split by 1.6 eV. We have accounted for this splitting with ab initio calculations - it results from the presence of OH and H_2O in the wetting layer, which is, accordingly, part dissociated. The peak heights imply that H atoms split off from only about 40% of deposited water molecules. Our latest calculations also account for this result. There is considerable controversy over whether this O-H bond-breaking is kinetically possible in the absence of sufficient ionizing radiation. There is no question, however, that the new XPS study confirms that the ab initio calculations do explain the early LEED experiment, and that dissociation is favored thermodynamically.

Significance—Confirming an atomic-scale understanding of water on ruthenium, the only wetting system whose structure has been measured, is the key to establishing it as "the hydrogen atom" of wetting phenomena. That the H_2O molecules are partially dissociated, in this case, has potentially profound implications for nanofluidics and electrochemistry.

Sponsors for various phases of this work include: DOE Office of Basic Energy Sciences

Contact: Peter J. Feibelman; Surface & Interface Sciences, Dept. 1114
Phone: (505) 844-6706, Fax: (505) 844-1197, E-mail: pjfeibe@sandia.gov

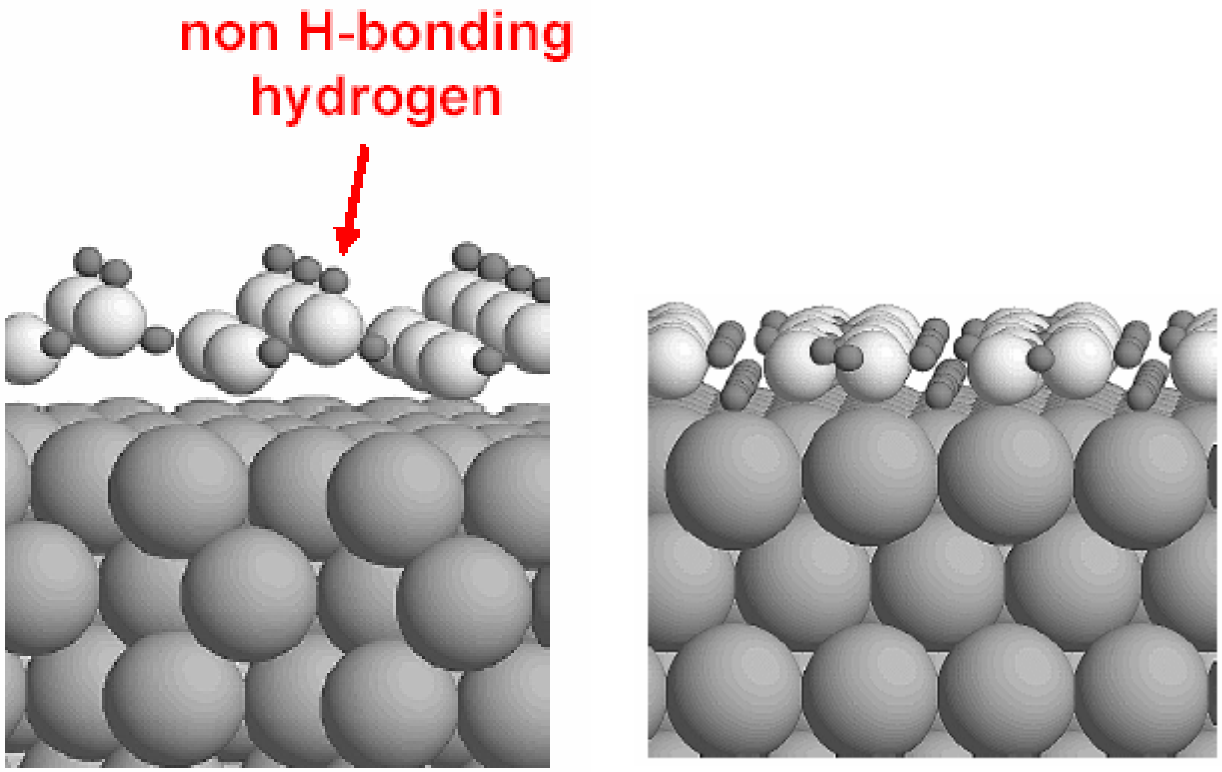

Figure 1. Left: Side view of an ice-like arrangement of a single layer of intact water molecules, adsorbed on the hexagonal surface of a ruthenium crystal. Large, medium and small spheres represent Ru, O and H or D atoms. Note the presence of non H-bonding H atoms. They should give rise to a particularly high frequency O-H stretching mode. That it is not seen is evidence that the structure depicted does not occur in nature. Right: Side view of a fully H-bonded arrangement of half H_2O molecules and half OH fragments. Note that the non H-bonding H atoms broken off water molecules to make the OH fragments are bonded directly to Ru atoms.

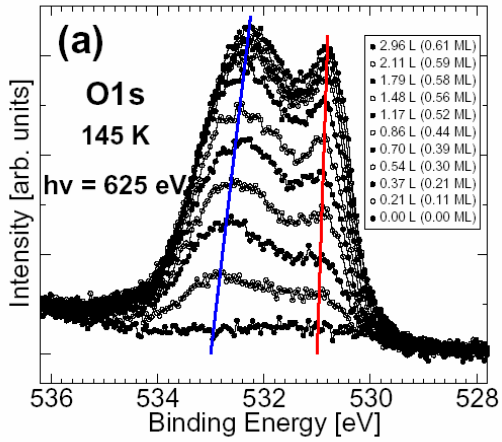

Figure 2. O (1s) X-ray photoemission spectrum up to 1ML water on ruthenium. The lower(higher) energy peak is from OH(H_2O). The smaller area under the OH peak implies that about 40% of the water molecules present are dissociated. [*Physical Review Letters* **93**, 196102 (2004)]

Scanning Probe Studies of Water Nucleation and Growth on Aluminum Oxide

by N. Missert and R. G. Copeland

Motivation—Understanding the interaction of nanoscale water layers with surfaces is important for many processes, such as atmospheric corrosion, stiction in MEMS and microfluidics. The initial layers of water that adsorb on a surface are thought to have a structure and properties that differ from the bulk. The defects, impurities, and morphology at the surface may profoundly influence the distribution of the water layer and thereby impact the properties of the water/solid interface.

Accomplishment—One approach to investigate the water/solid interface at the nanoscale is to use scanning probe microscopy to image the distribution of the water layer as a function of relative humidity. Initially, we have focused on the aluminum oxide covered aluminum surface, which is important in gaining understanding of atmospheric corrosion of interconnects in microelectronic components. Corrosion of the underlying aluminum occurs when the passive surface oxide is locally compromised through its interaction with water and aggressive halide species in the environment. The specific nature of the initiation sites is not known. However, if water adsorption is influenced by surface inhomogeneities, then by imaging the water layer distribution and measuring its properties we may gain a better understanding of the corrosion mechanisms and initiation sites.

We imaged the nucleation and growth of water droplets on aluminum thin films as a function of relative humidity using *in-situ* atomic force microscopy (AFM). A gold-coated hydrophobic tip, operated in tapping mode, minimized the interaction between the tip and the water layer and allowed imaging without distortion. Scanned images were acquired in an environmental chamber for humidities ranging from < 2% up to 99%. Although the interaction force between the probe tip and the sample surface showed an abrupt increase near 20% RH, topographical contrast due to the presence of a water layer was not observed until reaching 80% RH. Figure 1 shows the amplitude image as the RH is increased from (a) < 2% to (b) 80%. The hemispherical water droplets observed in (b) range in size from 20 nm to 200 nm. After 5 min. at 80% RH, the droplet size is observed to grow, while the distribution remains constant. The results for decreasing relative humidity are shown in Fig. 2. Here the droplets were observed to gradually evaporate, leaving behind a surface residue. Although the properties of this surface residue have not yet been investigated, its presence may impact corrosion of components that undergo cyclic variations in relative humidity.

Significance—These results suggest that there are preferred sites for water nucleation on the aluminum oxide surface. If these sites do play a role in the initiation of localized corrosion, then a greater understanding of these sites will contribute to our ability to make accurate lifetime predictions for electronic components.

Sponsors for various phases of this work include: Nuclear Weapons/Engineering & Science Campaigns (ESC) and Nuclear Weapons/Readiness Technical Base & Facilities (RTBF)

Contact: Nancy Missert; Nanostructure & Semiconductor Physics, Dept. 1112
Phone: (505) 844-2234, Fax: (505) 844-1197, E-mail: namisse@sandia.gov

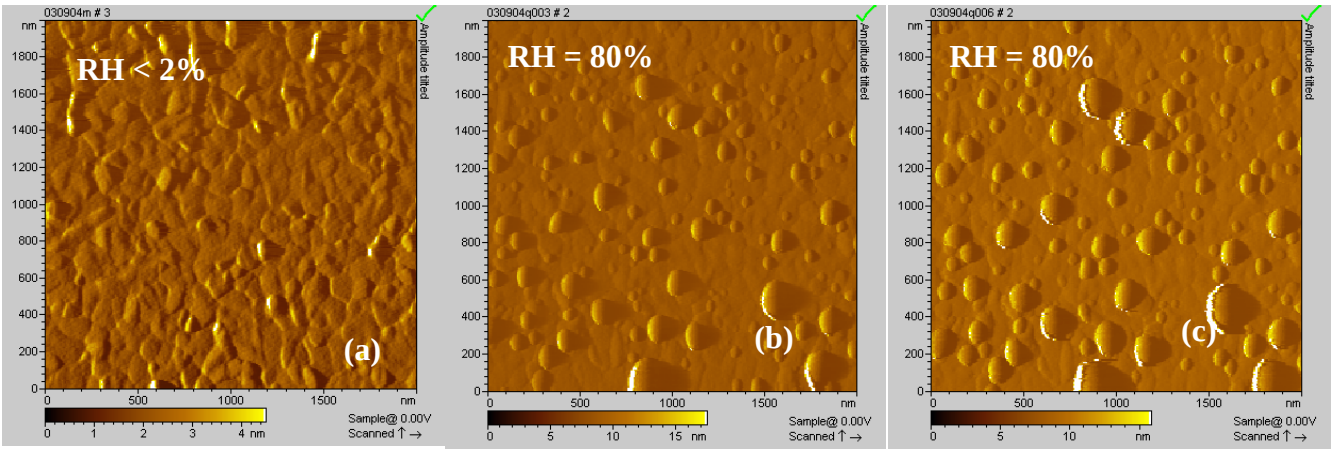

Figure 1. AFM images of an aluminum oxide covered aluminum thin film (a), showing the nucleation of hemispherical water droplets at 80% RH (b). After 5 minutes at 80% RH the droplets grow in size (c).

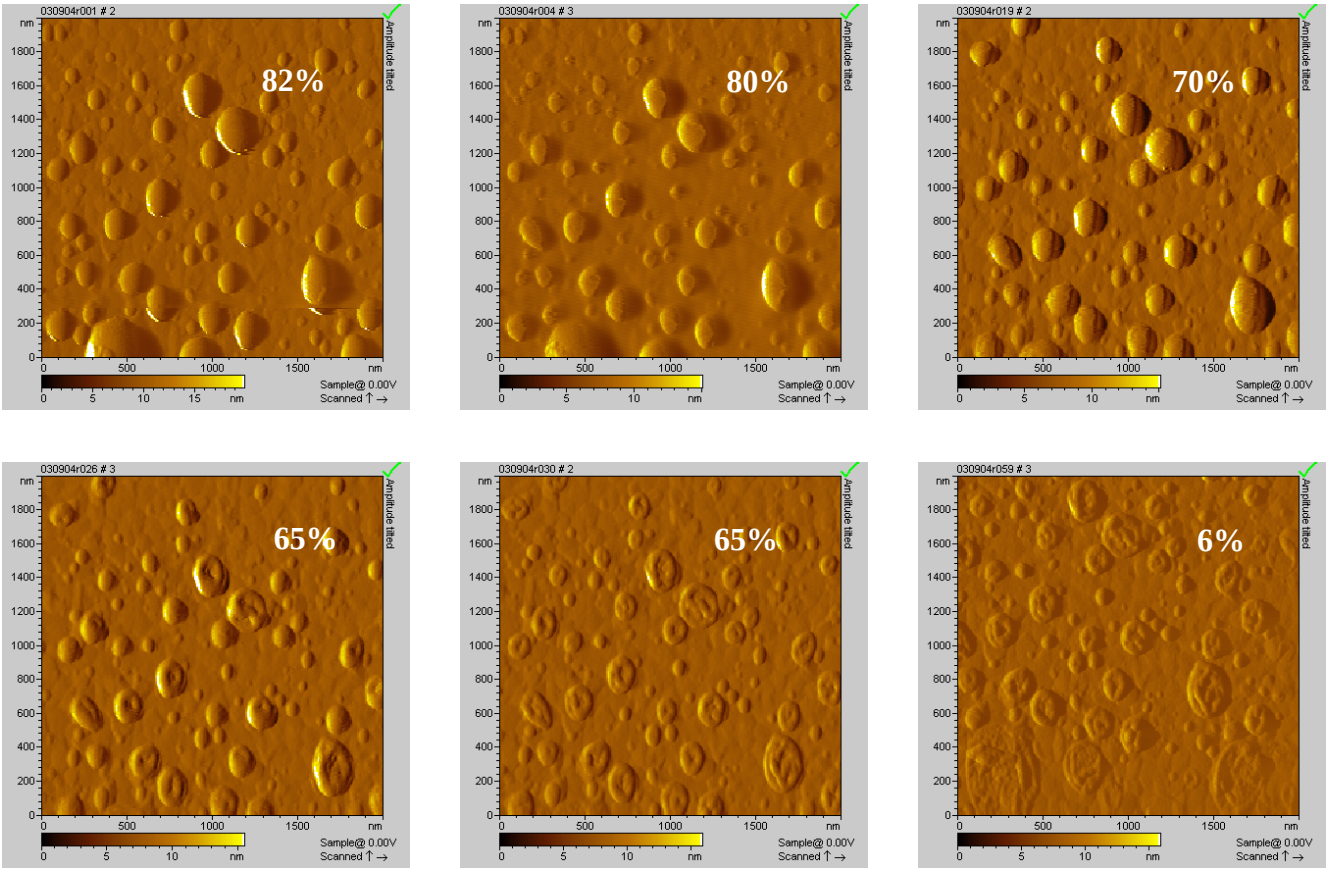

Figure 2. AFM images of an aluminum oxide covered aluminum thin film as a function of decreasing relative humidity following droplet nucleation at 82% RH. Droplets evaporate gradually as the RH decreases, leaving behind a surface residue.

Switchable Monolayers for Microfluidic Systems

by Bruce Bunker, Byung-Il Kim, Dale Huber, Gayle Thayer, William Smith, Jack Houston, and Thomas Phely-Bobin

Motivation—Interfacial water plays a key role in mediating the performance of microsystems ranging from fluidic devices to sensors to micromachines. The structure and properties of water can be changed dramatically near surfaces. Particularly as system dimensions enter the sub-micron regime (e.g., in small channels, pores, or spacings between micromachine components), the anomalous behavior of water can lead to system behavior that is dramatically different from that predicted on the basis of the properties of bulk water. We have been using a scanning probe instrument called the interfacial force microscope (IFM) to detect the presence of interfacial water and to probe interactions between materials that are mediated by the presence of water at length scales from microns to atomic dimensions. Recently, we have been using the IFM to probe changes in interactions that can be achieved using programmable self-assembled monolayers (SAMS).

Accomplishment—Interactions between water and substrates are normally controlled by the number and spacing of specific functional groups that terminate the surface. We have been investigating methods of switching the behavior of surface functional groups using signals that can be generated "on-chip", including heat, light, and electric fields. All systems investigated to date involve the incorporation of active molecules into self-assembled monolayers. Configuration changes within the active molecules promote changes in the adjacent solution, allowing us to manipulate interactions including repulsive and attractive hydration forces, double layer forces, hydrophobic/hydrophilic character, and capillary forces. The switching of interfacial interactions has been monitored using the interfacial force microscope, which enables us to obtain force-distance profiles between a functionalized substrate and a scanning probe tip as a function of separation distances typically ranging from 100 nm down to less than 1 nm. An example of a switchable surface is provided by the changes in surface chemistry that accompany the photoactivated opening and closing of rings in tethered spiropyran monolayers (Fig. 1). Contact potential measurement performed in the IFM show that exposure of native spiropyran to UV light opens an aromatic ring to produce an open isomer containing charged groups. This light-induced ring opening can be reversed with visible light, regenerating an aromatic, hydrophobic surface. Normal force measure- ments performed in the IFM (Fig. 2) show that the creation of charged sites via ring opening generates significant electrical double layer forces when the monolayer is immersed in water. These double layer forces can be switched on and off by exposing the surface to UV and visible light, respectively.

Significance—The IFM results demonstrate that it is possible to program interactions between surfaces immersed in water using heat, light, or electric fields. Such surfaces can be used to perform a wide range of functions in microfluidic devices, including pumping and control of fluid flows, reversible switching of adsorption and desorption of solution species, and controlling surface chemistries for switch-able separations and sensor devices. For example, we have demonstrated that a thermally-switchable polymer film (PNIPAM) can be used as a reversible trap for proteins. Development of such devices requires a funda-mental understanding of how materials interact with each other in water at sub-micron length scales. The interfacial force microscope pro-vides a unique tool for measuring such inter-actions and probing interaction mechanisms.

Sponsors for various phases of this work include: DOE Office of Basic Energy Sciences and Laboratory Directed Research and Development

Contact: Bruce Bunker; Biomolecular Materials & Interfaces, Dept. 1116
Phone: (505) 284-6892, Fax: (505) 844-5470, E-mail: bcbunke@sandia.gov

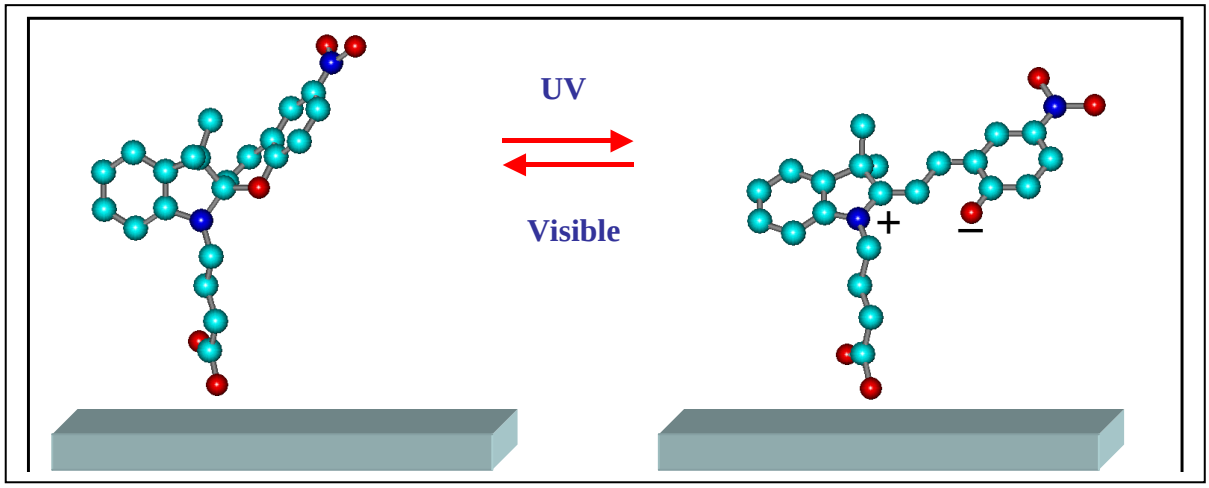

Figure 1. Representations of the spiropyran molecule in its native state (left) and after exposure to UV light (right).

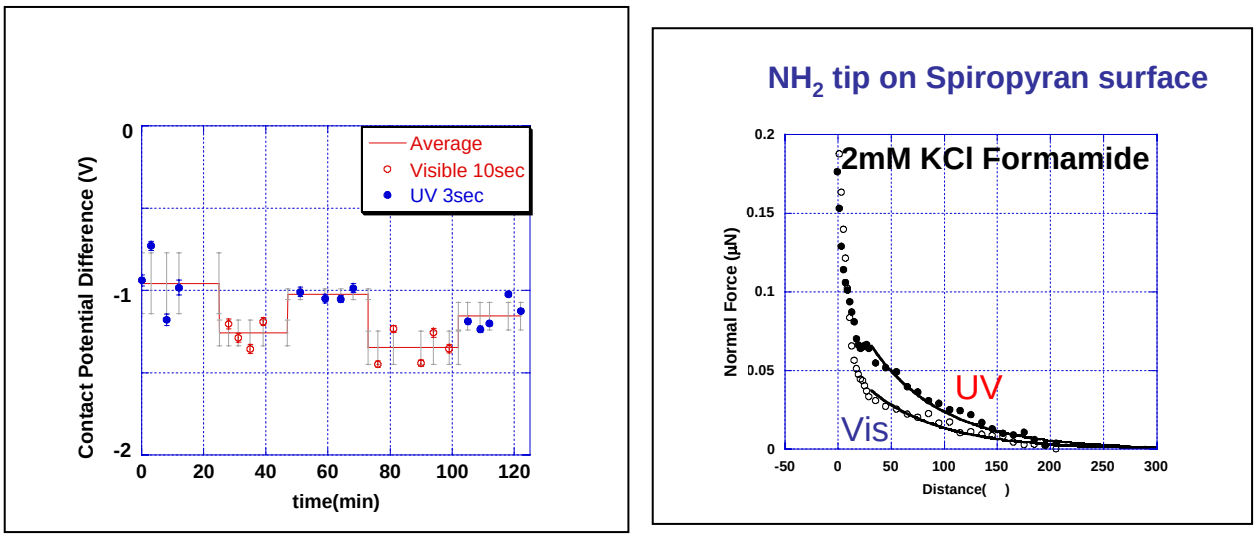

Figure 2. Interfacial force microscope results on switchable spiropyran films. Left – Changes in contact potential induced by sequential exposures to UV and visible light showing reversible creation and elimination of charged surface states due to ring opening and closing, respectively. Right – Force-distance profiles showing the UV-activated enhancement of electrical double repulsion that accompanies the formation of charged sites due to ring opening in tethered spiropyran monolayers.

Bridging the Nano-Micro Length Scale in Surface Science

by M. L. Anderson, N. C. Bartelt, B. S. Swartzentruber, P. J. Feibelman and G. L. Kellogg

Motivation—The ability to control the nanometer-scale structure of solids requires a fundamental understanding of physical phenomena occurring over multiple length scales. This is especially true for processes at surfaces, where often a delicate interplay between atomic-scale kinetics and macro-scale thermodynamics leads to stable nanoscale structures. To understand this interplay, experimental tools and modeling approaches that probe *both* the behavior of individual atoms as they migrate across surfaces *and* the collective motion of thousands of atoms as they organize into the desired surface structures are required.

Accomplishment—We are the first to combine scanning tunneling microscopy (STM) and low energy electron microscopy (LEEM) to understand the atomistic mechanisms controlling the 10-1000 nanometer-scale structure of a surface as it spontaneously self-assembles. The STM with its single-atom resolution can image surface features with dimensions of Angströms to tens of nanometers. The LEEM with a lateral resolution of 7-8 nanometers can image features from tens of nanometers to tens of microns. Together, the two instruments can view surface features spanning dimensions covering six orders of magnitude. The phenomenon that we are investigating is a particularly dramatic example of surface self-assembly—the spontaneous ordering of two-dimensional Pb islands on Cu(111) into stable patterns with submicron periodicities. In addition to a proper balance of thermodynamic forces, pattern formation in this system requires that two-dimensional islands containing tens of thousands of atoms have sufficient mobility to move across the surface and find their equilibrium positions. To understand the atomistics of this large-scale, collective motion, we are investigating the thermal decay (shrinking) of two-dimensional Pb overlayer and Pb-Cu alloy islands (Fig. 1). By applying both STM and LEEM to the same surface process we are able to measure decay rates covering 6-7 orders of magnitude (2-3 orders of magnitude are typical) and show that the mechanisms and energetics of mass transport remain the same from atomic to micron length scales (Fig. 2). From the temperature dependence of the decay rates, we determine that it is the migration of just one atomic species (Cu) that controls the overall kinetics of island decay. Combined with LEEM studies of Cu deposition on Pb overlayers and first-principles calculations of the formation energy for vacancies and interstitials within the Pb overlayer, these studies are providing a self-consistent picture of how two-dimensional islands, approaching 100 nanometers in diameter, move intact across Pb-Cu alloy surfaces.

Significance—A comprehensive understanding of pattern formation on surfaces requires quantitative information on both the thermodynamic forces that drive self-assembly and the kinetic processes that allow the patterns to evolve. Here, we find that the surprisingly large mobility of large two-dimensional islands (key to pattern evolution) is the result of mobile defects within the Pb overlayer—a totally unanticipated discovery. The new understanding is the result of our ability combine complementary surface microscopies and bridge length scales from atoms to microns.

Sponsors for various phases of this work include: DOE Office of Basic Energy Science and Nuclear Weapons/Science & Technology

Contact: Gary L. Kellogg; Surface & Interface Sciences, Dept. 1114
Phone: (505) 844-2079, Fax: (505) 844-1197, E-mail: glkello@sandia.gov

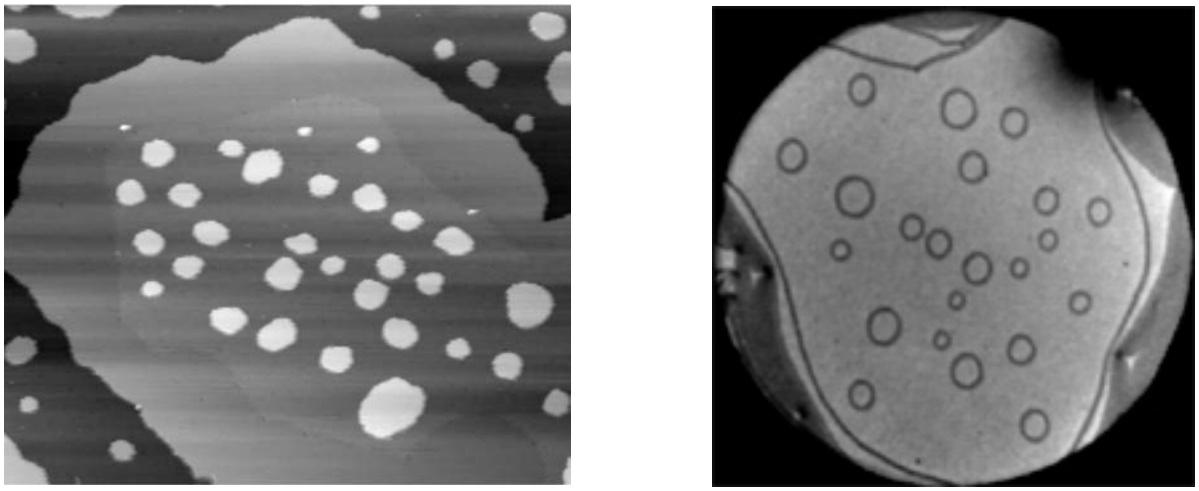

(a) STM (260 nm field of view) (b) LEEM (3 micron field of view)

Figure 1. Images of Pb overlayer islands on Pb-Cu surface alloy [(a) STM image and (b) LEEM image]. Note that the field of view in the two images differs by more than an order of magnitude. In both cases, the islands decay (shrink) as a function of time. Measurements of the decay rates probe the mechanisms and energetics of atom diffusion.

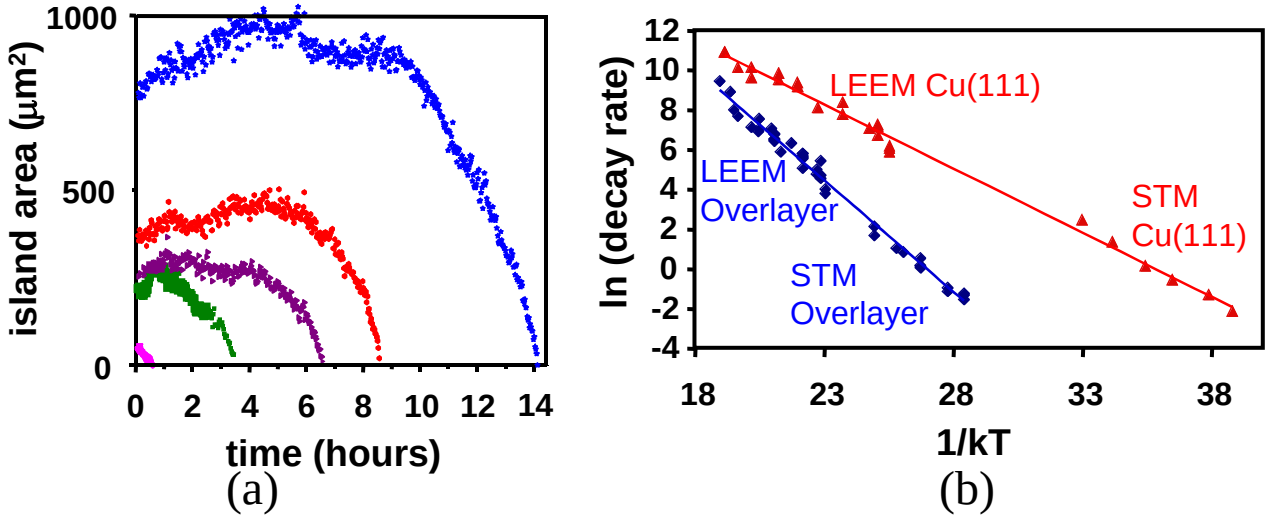

Figure 2. (a) Decay curves for selected Pb overlayer islands on a Pb-Cu surface alloy. (b) Arrhenius plots of island decay rates for pure Cu islands on Cu(111) and Pb overlayer islands on Pb-Cu surface alloy. Note that the data fall on a single straight line for the LEEM and STM measurements. All data are from this work except STM measurements of pure Cu islands, which are from: G.S. Icking-Konert, M. Giesen, H. Ibach, Surf. Sci. 398, 37 (1998).

Biomolecular Materials

A Thermostable Kinesin Motor Protein for Hybrid Nanoscale Systems

by G. D. Bachand, S. B. Rivera, S. J. Koch, and J. M. Edwards

Motivation—Living organisms assemble, organize, and disassemble nanoscale materials through the active consumption of chemical energy sources. Such energy-driven processes enable these materials to change composition, structure, and morphology in response to environmental conditions and stimuli. Our overall goal is to understand and to exploit key strategies used by living systems to develop new nanocomposite materials whose assembly and configuration can be programmed or "self-regulated" in artificial environments. To this end, we have isolated and characterized a thermostable kinesin motor protein that plays a central role in trafficking nano- and molecular scale materials within cells.

Accomplishment—A key hurdle to integrating active biomolecules into hybrid nanoscale systems centers on the ability to interface intrinsically diverse components. Fortunately, Nature provides an extraordinary array of organisms and molecular machines that have evolved to function under a wide range of conditions. The thermophilic, deuteromycetous fungus *Thermomyces lanuginosus* was selected for our work based on its high temperature growth optimum, and anticipated robustness in artificial environments. A gene encoding a kinesin motor protein was isolated using reverse transcription and the polymerase chain reaction to amplify the sequence from purified mRNA. The *Thermomyces* kinesin (*TKIN*) gene was then cloned into a bacterial expression plasmid, and engineered to introduce a 10x Histidine tag into the motor protein. The recombinant *TKIN* was expressed in the Tuner (DE3) pLacI strain of *Escherichia coli*, and purified from lysates using Ni-NTA chelate chromatography.

The temperature-dependent biochemical and biophysical properties of the recombinant *TKIN* were characterized with respect to use in synthetic architectures. DNA analysis of the coding sequence indicated that the *TKIN* is a member of the Unc104/KIF1A subfamily of kinesins. Size exclusion chromatography and gel electrophoresis confirmed that the *TKIN* exists as a functional monomer, compared to the conventional dimeric kinesin motor protein. The rate of ATP hydrolysis displayed a clear temperature dependency, with an apparent maximum at 50ºC followed by a rapid decline due to microtubule depolymerization (Fig. 1). The rate of microtubule transport in gliding motility assays displayed a maximum at ~45ºC (Fig. 1). The transport rate increased from 1.5 µm/sec at 25ºC, to a maximum of 5.5 µm /sec at 45ºC, which is substantially greater than any other characterized kinesin. Directional gliding motility assays indicated that *TKIN* is a plus-end directed motor protein, which is consistent with other members of this kinesin subfamily. We then evaluated the long-term performance of *TKIN* by monitoring changes in ATP hydrolytic rates over an extended period of time. No change in the hydrolytic rates was observed over this period, suggesting that this kinesin is capable of functioning at maximum performance for more than 11 days at room temperature (Fig. 2), which has not been previously demonstrated for any kinesin.

Significance—The ability to actively transport nanoscale cargo is a requisite first step for developing dynamic nanocomposite materials. We have isolated, engineered, and characterized a thermostable kinesin motor protein that possesses the necessary characteristics for integration at synthetic interfaces. Our detailed analysis and understanding provides a critical framework for defining the operational range in which *TKIN* can be used to assemble and organize nanocomposite materials.

Sponsors for various phases of this work include: DOE Office of Basic Energy Sciences, Laboratory Directed Research & Development, and Defense Advanced Research Projects Agency

Contact: George D. Bachand; Biomolecular Materials & Interfaces, Dept. 1116
Phone: (505) 844-5164, Fax: (505) 844-5470, E-mail: gdbacha@sandia.gov

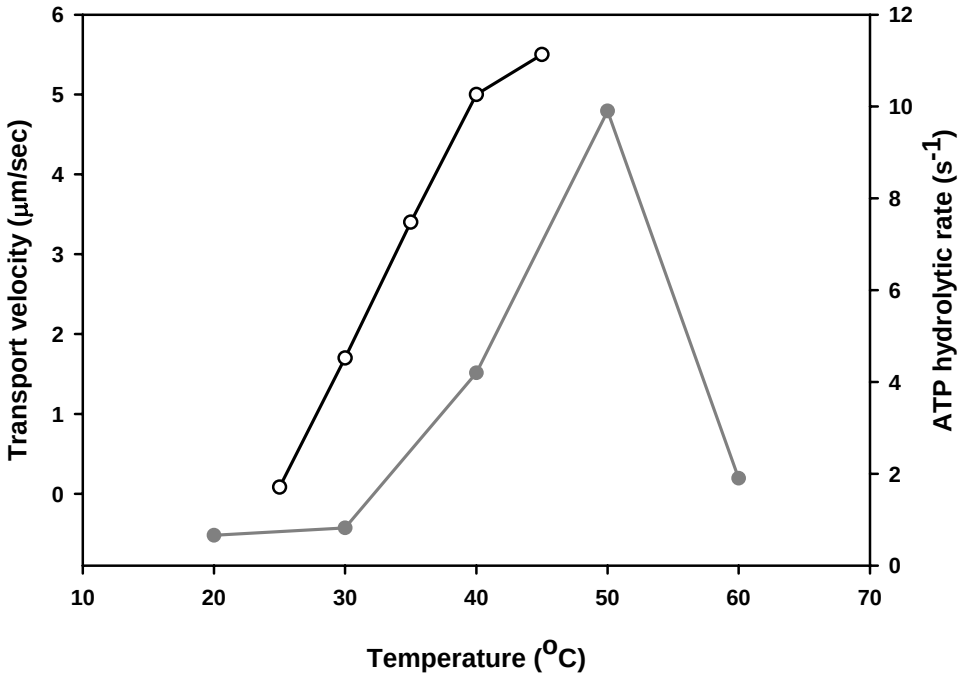

Figure 1. Temperature-dependent effects on the transport rate (-○-) and ATP hydrolysis (-●-) observed for *Thermomyces* kinesin. Both the transport and hydrolytic rates display an apparent peak at 45 – 50ºC, which is consistent to the temperature optimum for this fungus.

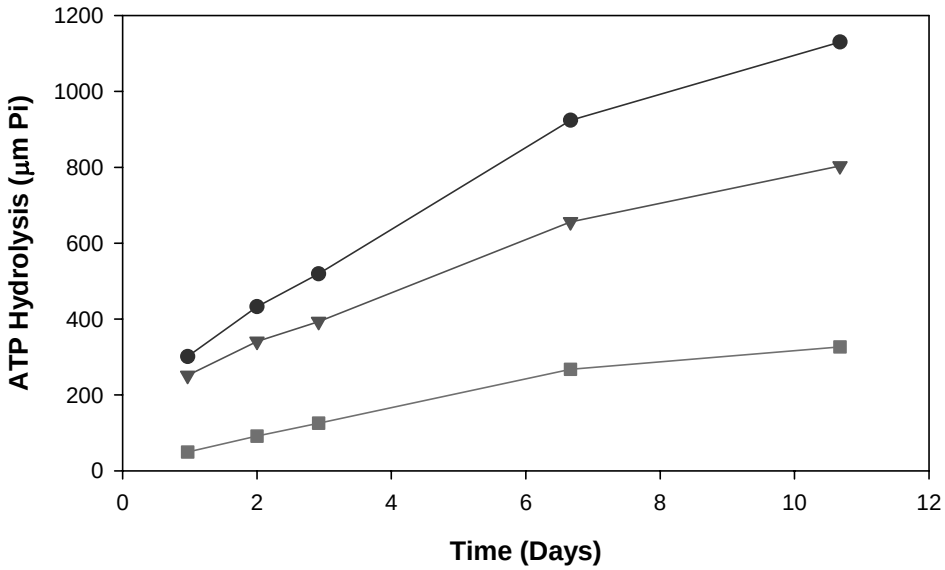

Figure 2. Rate of ATP hydrolysis of *Thermomyces* kinesin over 11 days at room temperature. The corrected rate of kinesin hydrolysis (-●-) was determined by subtracting the background rate of ATP hydrolysis (-▼-) from the total rate of ATP hydrolysis (-■-).

Nanoparticle Transport Using Motor Proteins

by Bruce Bunker, George Bachand, Andrew Boal, Susan Rivera, Joe Bauer, and Ron Manginell

Motivation—In living systems, molecular motors called motor proteins are used to assemble and manipulate objects ranging in size from proteins to muscles. Sandia is currently exploring the extent to which these molecular machines can be exploited within artificial microfluidic systems to manipulate nanometerials. As a first step, we are developing the basic components of an energy-consuming active transport system that can be used to pick up, transport, and deposit nano-particles within a microfluidic system. The active transport system is based on the interactions between self-assembled monolayers containing the motor protein kinesin and short (5-10 μm long) segments of 25 nm diameter protein tubes called microtubules. In the presence of a fuel source (adenosine triphosphate or ATP), the head groups in the motor proteins "walk" along specific sites on the microtubule. When the kinesin motors are tethered within self-assembled monolayers (Fig. 1), the collective action of the motors can propel microtubule "shuttles" across a substrate surface.

Accomplishment—We have now demonstrated that microtubule shuttles can be functionalized to carry nanoparticles across a surface, and have also developed surface functionalization schemes for substrates that allow nanoparticles to be collected and deposited in desired regions within a microfluidic system. Random incorporation of the chemical handle biotin has been used to provide binding sites for streptavidin-coated gold nanoparticles. Video images obtained in a fluorescence microscope show that large numbers of particles can be carried by each microtubule without interfering with transport (shuttles continue to move at velocities of up to 2 μm/sec — Fig. 2). However, for the case of streptavidin-coated CdSe quantum dots, it appears that particle loadings are so high that the motor proteins can no longer bind to the microtubules. To overcome this problem, we have used functionalized microtubules as "seeds" to grow hybrid microtubules in which the ends of the tubes contain no functional groups. The non-functionalized segments serve as "engines" for the microtubule "train" whose central segment serves as the "car" for carrying nano-cargo. Transport measurements show that the hybrid microtubules laden with quantum dots are readily transported across monolayers containing the motor proteins (Fig. 2). Work is in progress to utilize this active transport system to: (1) assemble conductive interconnects using gold particles (by analogy to the natural assembly of diatom skeletons from silica nanoparticles), and (2) reconfigure arrays of quantum dots in analogy to the color changing system of the chameleon.

Significance—Self-assembly processes represent the current state-of-the-art for organizing nano-scale objects into macroscopic materials. While objects ranging in complexity from self-assembled monolayers to meso-porous materials can be produced via self-assembly, the range of structures that are possible from such assembly are limited by diffusion and equilibrium interactions between assembling components. By progressing to active assembly processes using energy-consuming molecular machines such as motor proteins, we should ultimately be able to create or reconfigure highly non-equilibrium structures. The research reported here represents an important first step in controlling active assembly. We have shown that motor protein systems can be used to pick up, transport, and deposit nanoparticle cargo within artificial microfluidic systems. The next step in the process will involve learning how to actively program transport and cargo manipulation functions.

Sponsors for various phases of this work include: DOE Office of Basic Energy Sciences, Defense Advanced Research Project Agency, and Laboratory Directed Research & Development

Contact: Bruce Bunker; Biomolecular Materials & Interfaces, Dept. 1116Phone: (505) 284-6892; Fax: (505) 844-5470; E-mail: bcbunke@sandia.gov

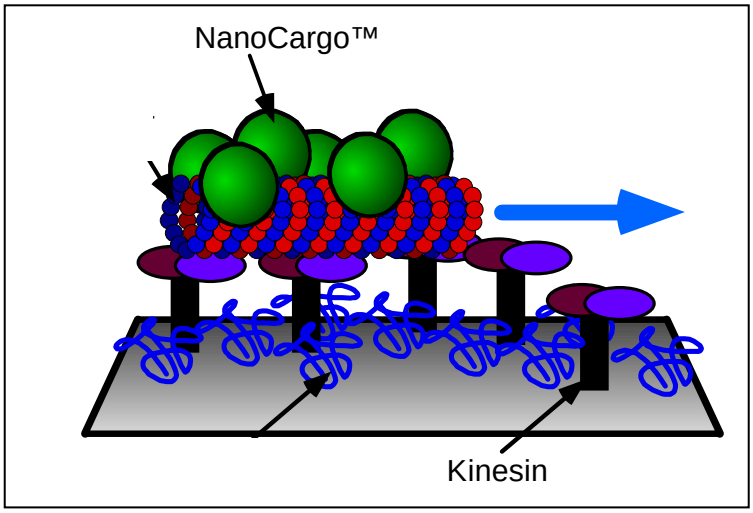

Figure 1. Schematic showing the monolayer geometry used to deploy motor proteins for active transport in artificial microfluidic substrates. Black tails of kinesin motors are tethered within a monolayer (blue lines) on a substrate surface. ATP-activated motion of head groups (ovals) propels a microtubule and its associated nanoparticle cargo.

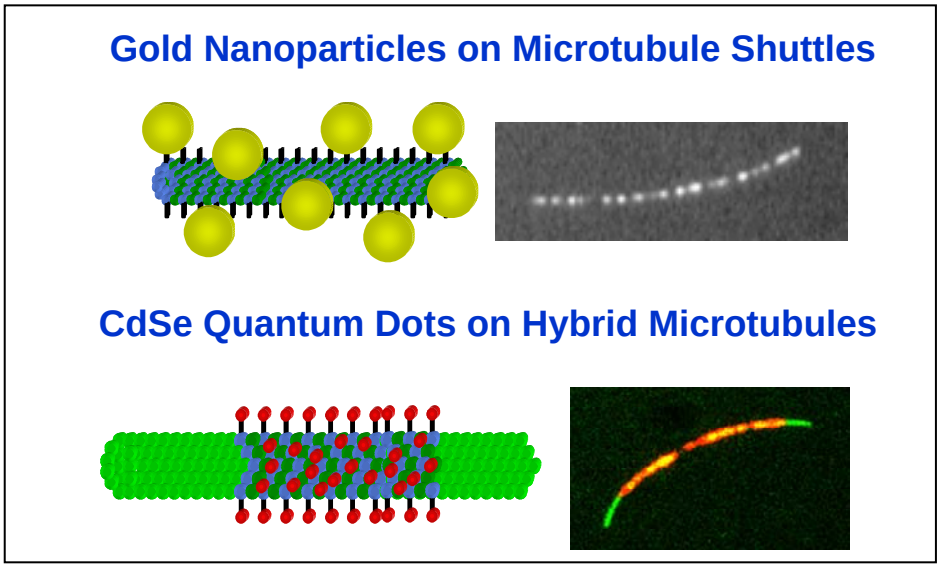

Figure 2. Top – Random functionalization of microtubules allows for attachment (left) and transport (right) of fluorescently labeled gold nanoparticles. Bottom – Hybrid microtubule (left) forms a "nanotrain" in which normal tubulin (green) provides transport, while functionalized tubulin (blue) carries quantum dot cargo. Microtubules shown in the micrographs on the right are around 8 μm long, and are taken from video images in which both types of shuttles crawl along the substrate surface. The bright spots in the upper micrograph are gold nanoparticles. In the bottom image, the green regions are fluorescently labeled tubulin, while the red and gold areas are regions laden with quantum dots.

BioLaser INCEPTOR for Rapid Detection and Differential Analysis of Anthrax Endospore Simulants

by ***Paul Gourley, Anthony McDonald, Judy Hendricks, Guild Copeland, Keith Barrett***

Motivation—The anthrax bio-terrorism threat has become a reality. Innocent people have died by inhalation of anthrax spores sent via U. S. mail. A transduction method that could quickly detect anthrax spores would be a valuable tool in the fight against bio-terrorism. To this end, we devised a highly sensitive quantum optics transduction method using biocompatible laser microcavities to detect submicron pathogenic spores. The method uses recent advances in surface chemistry of semiconductor materials to create the microcavity.

Accomplishment—Anthrax spores and their simulants are very tiny particles, less than a micron in diameter, and nearly as small as the wavelength of light. Detection and analysis of these ultra-small particles requires new spectral-imaging techniques with high sensitivity. Our bright idea was to use nano-squeezing of spontaneous light emitted through a spore flowing at high speed in a biocompatible semiconductor microcavity. This quantum squeezing allows even tiny spores to generate a whoppingly large spectral signal that can be easily detected. The spectral images (hyperspectra) are rapidly recorded and analyzed in a newly devised biolaser INCEPTOR (intracellular protein transduction by optical resonance) spectral imager/analyzer shown in Fig. 1. The laser light is spatially, spectrally, and temporally analyzed within seconds using efficient recognition software. This method extracts critical biological information from the lasing hyperspectra, including the protein coat morphology, intracellular granularity, spore shape and intracellular protein density and uniformity. The highly sensitive testing of two common spore types *b. subtilus* and *b. pumilus*, which appear identical under the microscope, are shown in Fig. 2.

Significance—These data indicate that, with further development and testing, the biolaser INCEPTOR could rapidly identify different types of anthrax spores, within a population of non-pathogenic spores. This analysis could be very useful for rapid, front-end screen of suspected pathogenic bacteria. The entire process, from set-up to diagnosis, could be completed in minutes. Such a field-deployable instrument is an attractive alternative to other, more time-consuming and labor-intensive DNA fragment analyses. Those analyses typically require restriction enzymes, PCR amplification, fluorescent tagging and cumbersome pulsed-field gel electrophoresis or specialized, expensive flow cytometry equipment. Further, the biolaser technique is compatible with immunofluorescence methods using molecular tags designed for anthrax antibodies. If intra-cavity surfaces are coated with an immunoassay antibody and the sample solution containing the conjugate antigen flowed over the surface, the emitted light sensor will detect the interaction.

Sponsors for various phases of this work include: DOE Office of Basic Energy Sciences and Laboratory Directed Research & Development

Contact: Paul L. Gourley; Biomolecular Materials & Interfaces, Dept. 1116
Phone: (505) 844-5806, Fax: (505) 844-5470, E-mail: plgourl@sandia.gov

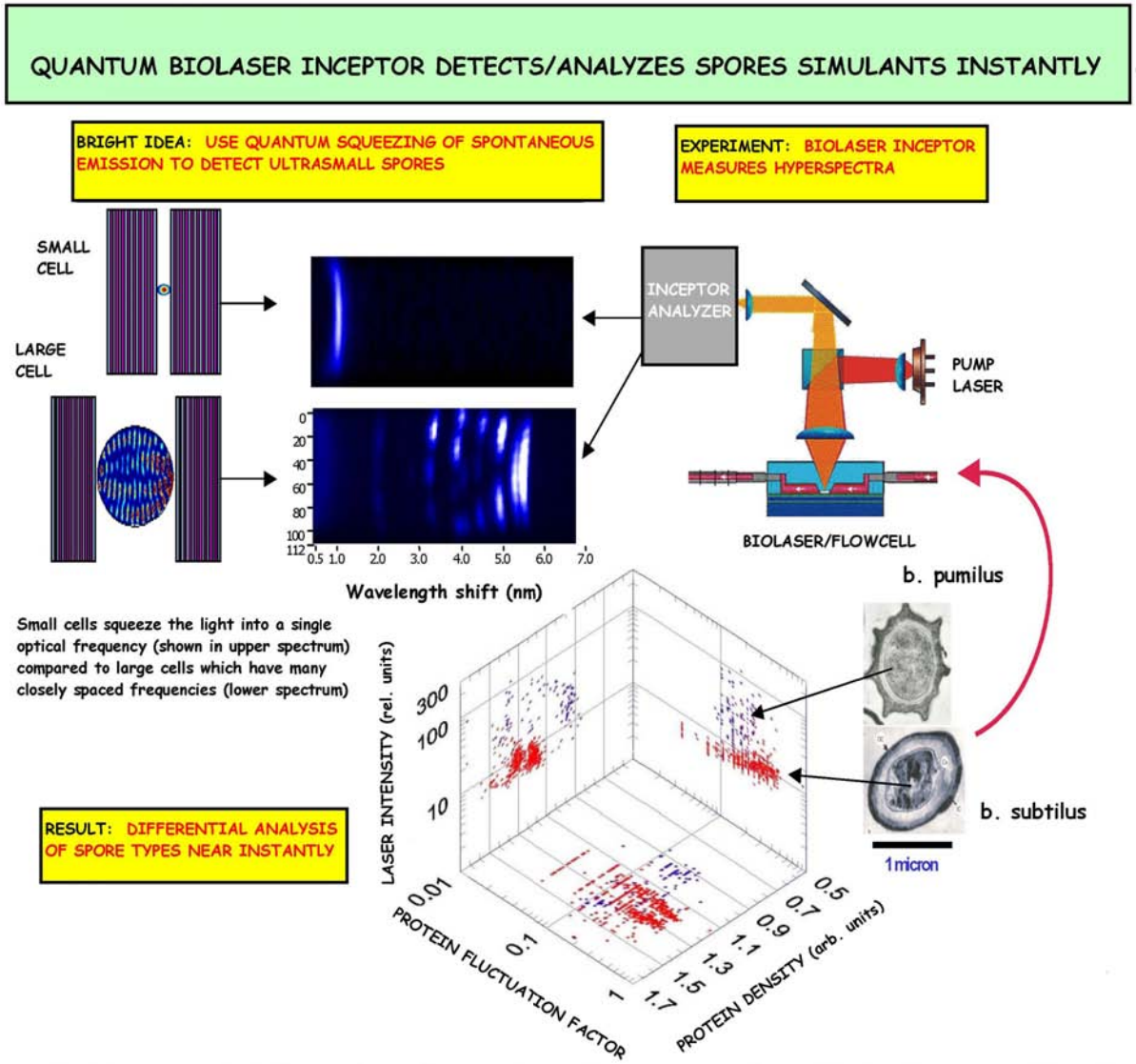

Figure 1. The upper left figure is an illustration of nano-squeezing of light through cells. The upper right figure represents an experimental for measuring spores. The lower figure is a measurement of spores showing different signatures for *b. pumilus* and *b. subtilus*.

Antibody Trapping on Switchable Films

by ***Bruce Bunker, Dale Huber, William Smith, George Bachand, and Thomas Phely-Bobin***

Motivation—For Homeland Security, Sandia needs to develop compact separations systems and sensors that can selectively adsorb and detect a wide range of potential biological agents. The most sensitive and selective materials for binding bio-agents are antibodies. Unfortunately, most existing analytical systems that exploit antibodies utilize antibodies that are permanently tethered to substrate surfaces. This means that active surfaces must be discarded after only one use, and that a given active surface can only be used to detect the one species that is recognized by the specific antibody. The motivation of this research is to use Sandia's existing "protein trap" technology to reversibly adsorb and release antibody monolayers for reusable microanalytical systems.

Accomplishment—Sandia's reversible protein trap consists of a micro-hotplate device onto which a thermally-activated polymer (PNIPAM) film is tethered. The hotplate is used to switch PNIPAM between a room-temperature phase that repels proteins and a higher temperature phase that adsorbs proteins. The bare PNIPAM film is not particularly selective for specific proteins, adsorbing a wide range of different bio-species from solution. However, we have recently demonstrated that PNIPAM films can be made highly selective by using the thermally-activated films to grab and release monolayers consisting of antibodies. The viability of the adsorbed antibody film as a highly selective adsorbing layer for biosensors has also been demonstrated. Adsorption experiments to date have involved tobacco mosaic virus (TMV) as a model "bio-agent" and two antibodies [non-specific Rabbit immunoglobulin G (Rabbit IgG) and the TMV-specific TMV-IgG]. Component adsorption on thermally-activated PNIPAM films has been monitored using ellipsometry (Fig. 1) and neutron reflectivity measurements performed using the LANSCE neutron scattering facilities at Los Alamos. First, the ellipsometry results show that PNIPAM films can be programmed to reversibly adsorb and release antibodies (both Rabbit IgG and the TMV-IgG). Second, TMV adsorption experiments show that TMV-IgG remains active and is highly selective for TMV when adsorbed on the PNIPAM surface. While slight TMV adsorption is observed on bare PNIPAM, no adsorption is observed when the PNIPAM is covered with Rabbit IgG, while extensive adsorption is observed when the TMV-IgG is present. Recent experiments suggest that once the TMV is bound to TMV-IgG on the PNIPAM, the antibody-antigen complex can be desorbed almost completely by cooling the PNIPAM to room temperature.

Significance—Now that reversible trapping of antibodies and antigens has been demonstrated, we are in a position to start learning how to integrate reversible antibody trapping into separation and sensor systems. The scheme shown in Fig. 2 illustrates how the antibody trap can be used to selectively remove specific bioagents from a feed stream in a microfluidic system. For biosensors, agents pre-concentrated and released from the trap could be sent to down-stream components, eliminating the undesired background associated with other biomaterials present in the feed stream. Alternatively, the film used for capture and release could be incorporated into an active sensor element, producing a compact device in which capture and sensing are performed simultaneously. Work is in progress to integrate the antibody trap into a shear-horizontal acoustic wave device to test this concept.

Sponsors for various phases of this work include: Laboratory Directed Research & Development

Contact: Bruce Bunker; Biomolecular Materials & Interfaces, Dept. 1116Phone: (505) 284-6892, Fax: (505) 844-5470, E-mail: bcbunke@sandia.gov

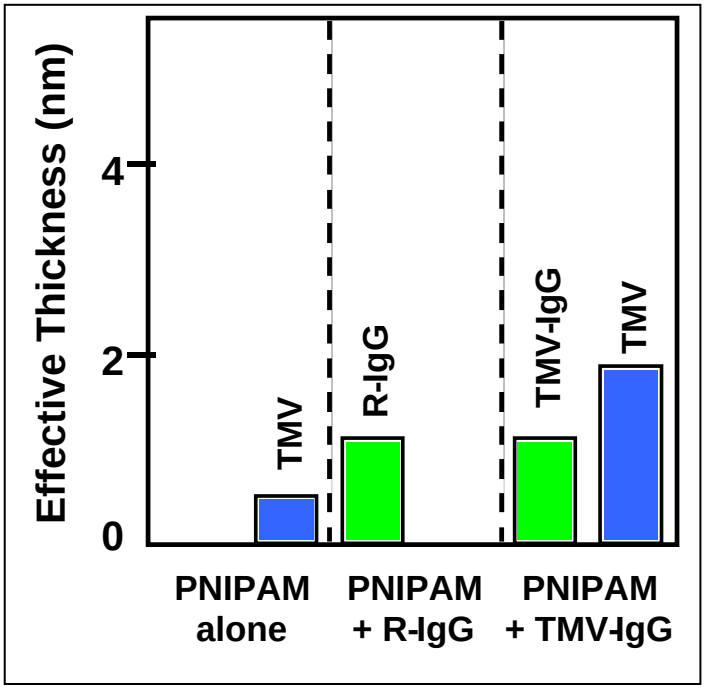

Figure 1. Left – Adsorption of tobacco mosaic virus (TMV) on activated PNIPAM film. Center – Adsorption of Rabbit immunoglobulin G (R-IgG) and TMV on the R-IgG layer. Right – Adsorption of TMV-IgG and TMV on the adsorbed TMW-IgG showing the high specificity for TMV adsorption on the TMV antibody relative to the rabbit antibody.

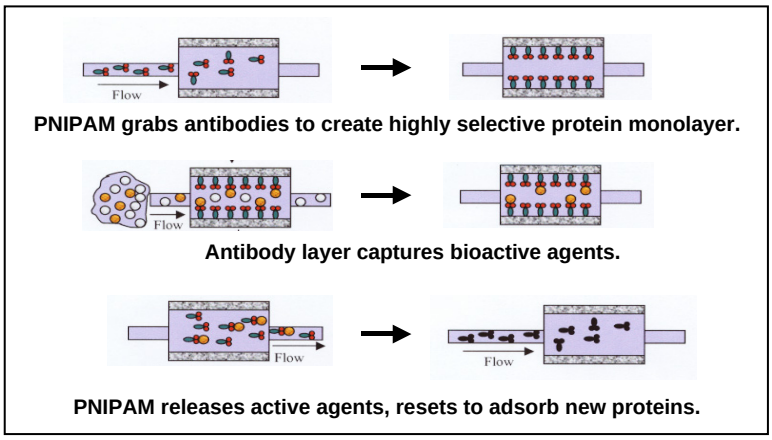

Figure 2. Schematic showing the sequence of steps needed to capture and release bio-species using reversible antibody trapping.

New Properties of Nanomaterials

Photocatalytic Nanotubes

by Zhongchun Wang, Craig J. Medforth, and John A Shelnutt

Motivation—Photocatalytic processes in nature are efficient means for generating energy sources and controlling chemical reactions. A biological example is the generation of energy-rich sugar molecules through photosynthesis. The goal of this research is to understand the energy- and electron-transfer processes that function within porphyrin nanotubes. We recently discovered these nanotubes, which may mimic the photosynthetic function of the chlorosomes of green sulfur bacteria, and can be used to create functional composite nanotube devices such as a nanodevice that splits water to produce hydrogen.

Accomplishment—The porphyrin nanotubes were discovered while attempting to make photocatalytic porphyrin fibers as templates for metal growth. The nanotubes are formed by ionic self-assembly of two types of porphyrin molecules of opposite charge. The tubes were imaged by electron microscopy and found to be hollow with a uniform average outside diameter of 60 nm and inside diameter of 20 nm; the lengths are variable and typically micrometers long. Smaller diameter nanotubes can be made by altering the molecular structure of one of the porphyrins. Transmission electron microscope (TEM) images of the porphyrin nanotubes are shown in Fig. 1.

The aggregated porphyrins forming the walls of the tubes are *J*-type aggregates, leading to intense resonance light scattering from the *J*-aggregate absorption bands in the green and red region of the UV-visible spectrum. The coherent coupling of porphyrin molecules indicated by the resonance light scattering suggests that energy and electron transport in the porphyrin nanotubes is facile and further suggests that the nanotubes may be conductive, photoconductive, and might serve light-harvesting and electron-transport functions in nanodevices. We have also found the nanotubes to be mechanically responsive to light; that is, they become soft when exposed to bright light and heal when they are returned to the dark. Since the nanotubes are composed of a porphyrin that is a known photocatalyst, we have investigated the possibility of growing novel metal composite structures by using the nanotubes as templates. Reduction of metal is found to take place only on the tubes and in a surface-selective manner. Figure 2 shows TEM images of nanotubes upon which either platinum or gold has been grown by photocatalytic reduction of metal ions from aqueous solution. In the case of gold, metal is deposited only in the cores of the tubes in the form of continuous polycrystalline wires, which grow a gold ball at one end of the nanotube. In contrast, platinum metal appears as 3-nm particles attached to the outer surfaces of the tubes, dense columns of platinum particles inside the tube cores, or as nanodentrites attached to the outer surface of the tubes.

We are continuing our efforts to gain synthetic control over these metal-nanotube composites. We are also attempting to build nanodevices for chemical sensing and other applications. For example, we have designed a nanodevice for water-splitting to produce hydrogen based on the use of the gold nanowire as a conductor linking an inorganic photocatalyst for oxygen evolution to our hydrogen-evolving platinized nanotubes.

Significance—The photocatalytic nanotubes are capable of serving as functional elements in many types of self-assembled nanodevices, including chemical sensors, mechanical sensors, and artificial photosynthetic systems. The photocatalytic properties of the nanotubes themselves can be employed for the assembly of the nanodevice. The porphyrin tubes may also serve as nanoscale functional elements of other photonic and electronic devices that utilize their novel conductivity and light scattering properties.

Sponsors for various phases of this work include: DOE Office of Basic Energy Sciences and Laboratory Directed Research & Development

Contact: John A. Shelnutt; Biomolecular Materials & Interfaces, Dept. 1116
Phone: (505) 272-7160, Fax: (505) 272-7077, E-mail: jasheln@unm.edu

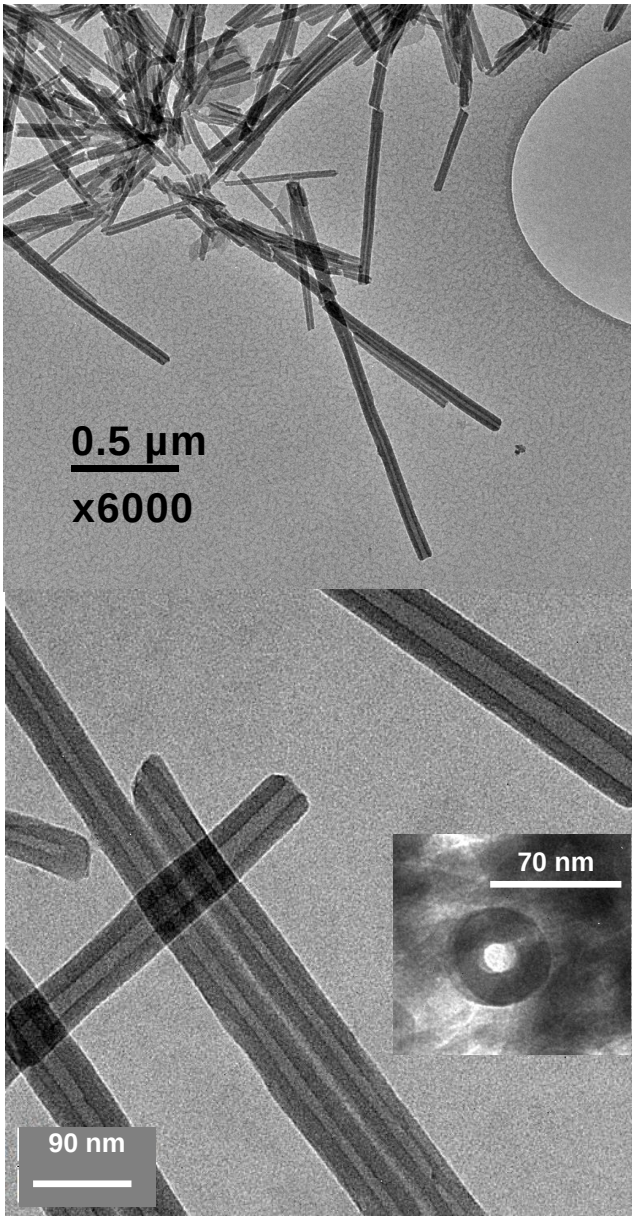

Figure 1. TEM images of porphyrin nanotubes at low (top) and high (bottom) magnification. Inset: a tube caught in a vertical orientation.

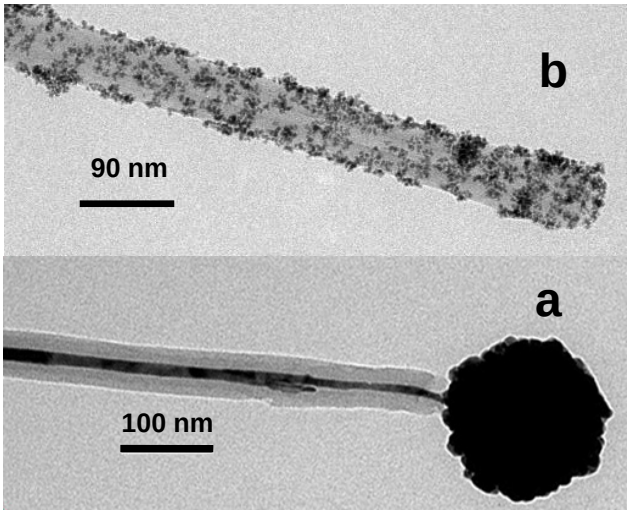

Figure 2. TEM images of a gilded porphyrin nanotube (a) and a platinized porphyrin nanotube (b).

Fe Nanoclusters: Novel Solution Synthesis and Enhanced Magnetic Properties

by D. L. Huber, E. L. Venturini, J. E. Martin, and P. P. Provencio

Motivation—Structured superparamagnetic (i.e., monodomain) particle composites can produce susceptibility enhancements far superior to those achievable in micron scale, multi-domain particles. Micron-scale multidomain particles have a susceptibility that is limited by classical physics to a maximum of 3 (MKS units are used throughout this report) for spheres due to the effect of the demagnetizing field. This limitation does not exist for superparamagnetic particles, and they can have particle susceptibilities that are much greater than 3. Such high susceptibility particles have a very strong response to even weak magnetic fields, and represent a situation where nanoparticles have properties that are unachievable in coarser materials. Our goal was to synthesize magnetic nanoparticles that have a very strong magnetic response to be used in the formation of field-structured nanocomposites.

Accomplishment—Our synthetic approach is based on the widely used decomposition of iron pentacarbonyl. The novelty of the approach is the surfactant system used. Studies with a number of strongly bound surfactants have resulted in decreased magnetic response, due to surface oxidation, disturbing the electronic structure of the surface atoms, or some other mechanism. This typically results in iron nanoparticles that have a saturation magnetization of 40-50% that of bulk iron (for 5-6 nm particles), due to strong electronic interactions with the surfactants. With this in mind, we chose to work with a weak surfactant, a β-diketone. β-diketones do have a history as adhesion promoters in bonds between metals and polymers, but have never been used to synthesize metallic nanoparticles. Synthesizing particles with this surfactant, we have achieved saturation magnetization values of greater than 80% that of bulk iron for approximately 5 nm particles (see Fig.1). Additionally we have observed very high susceptibilities, as high as 14 (at 150K), which far exceed the theoretical maximum of 3 for spherical multi-domain particles. This represents a sample of magnetic nanoparticles whose magnetic response is much higher than is possible in similar materials with larger dimensions. The magnetic susceptibility is so high that in the absence of an applied magnetic field the particles magnetically aggregate into coarse columnar structures (see Fig. 2). Although mechanical agitation can create a very fine dispersion, and both TEM and magnetic measurements confirm that the sample is made up of discrete nanoparticles, agglomerates quickly form in solution leading to a precipitate. The ease with which these particles magnetize and form structures in the absence of an applied magnetic field, implies that the application of an external field will readily structure the nanoparticles.

Significance—The synthetic procedure presented here represents a substantial step forward in the ability to synthesize highly magnetic iron nanoparticles. These particles are highly crystalline bcc iron, and are free of detectable oxide. This synthesis seems particularly useful in the 5-10 nm size range, which is an important size iron nanoparticles, as it represents the lower limit of sizes where iron particles are expected to strongly structure under an applied magnetic field at room temperature.

Sponsors for various phases of this work include: DOE Office of Basic Energy Sciences and Laboratory Directed Research & Development

Contact: Dale L. Huber; Nanostructure & Semiconductor Physics, Dept. 1112
Phone: (505) 844-9194, Fax: (505) 844-1197, E-mail: dlhuber@sandia.gov

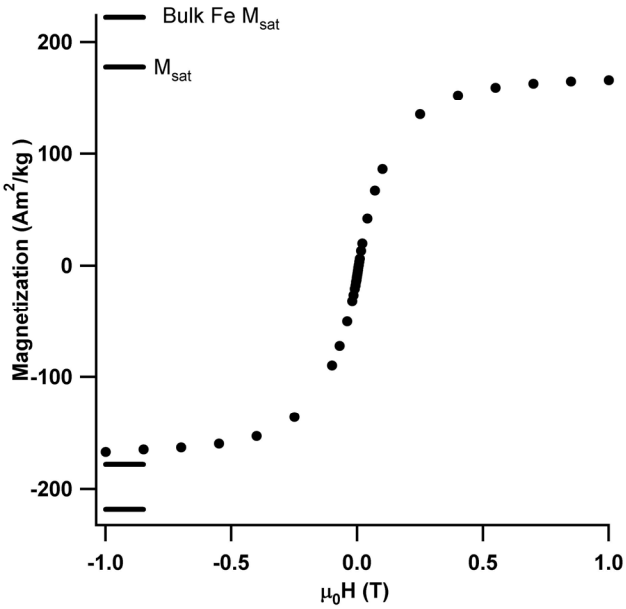

Figure 1. Magnetization versus field for an iron nanoparticle sample at 150 K. The sample is below its blocking temperature and therefore shows a weak but detectible coercivity (5.6 mT). Saturation magnetization is determined by extrapolating to infinite field and is 178 A m^2/kg, or greater than 80% of the value of bulk iron.

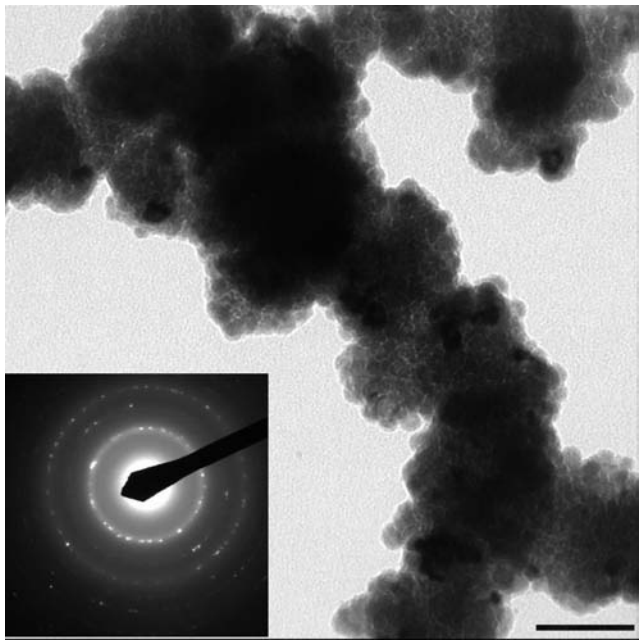

Figure 2. TEM micrograph of approximately 6nm iron nanoparticles, showing magnetic agglomeration. The scale bar represents 60 nm. Inset diffraction pattern verifies that this sample is pure BCC Fe with diffraction rings at 0.8, 0.9, 1.0, 1.2, 1.4, and 2.0 Å.

Nanoporous-carbon: A Revolutionary New Material for Chemical Microsensors

by M. P. Siegal, D. L. Overmyer, P. P. Provencio, W. G. Yelton, and A. W. Staton

Motivation—Gas-phase sensors for rapid detection of airborne chemicals are critical to public health and national security. Chemical sensors depend on sorbent coatings compatible with environmental parameters, such as temperature, humidity, and chemical background. Such coatings need to be sensitive, reproducible, and stable for long-term use. Unfortunately, typical polymer and sol-gel coatings are constrained by stresses to sub-micron thicknesses, limiting the available sorption, and degrade with time and repeated thermal cycling. Surface acoustic wave (SAW) devices respond to gas-phase analytes by decreasing the oscillating frequency as a function of analyte concentration due to an increase in the sorbent mass. To be useful for SAWs, the coating must have both high surface area and rigidity. Nanoporous-carbon (NPC) uniquely combines these critical properties. NPC grows at room temperature with negligible residual stress on any substrate to any thickness. Purely graphitic and nanocrystalline, NPC is chemically robust and stable to temperatures > 600 ˚C, well above any thermal cycling used for devices.

Accomplishment—NPC grows via pulsed-laser deposition by focusing 248 nm excimer radiation to ablate a graphite target with an energy density just above the ablation limit. The ablated species kinetic energy is further attenuated via a controlled argon pressure during deposition, resulting in a lower average NPC mass density. Figure 1 shows transmission electron microscope images for NPC with densities of 0.25 and 1.0 g/cm^3. Films with the lowest densities have nm-sized voids, as shown by the arrow in Fig. 1(a); however, all NPC films have interplanar spacings between graphene sheet fragments greater than that of crystalline graphite. The spacing decreases with increasing density. Both of these structural features add useful surface area for analyte sorption. Intercalation into graphite is well known, and increasing the interplanar spacing should ease diffusion both in and out of the coating.

Figure 2(a) shows SAW performance detecting acetone sorption into various density NPC films. The power law relationship infers that while low-density NPC has greater adsorption of acetone at high concentrations, such films lose sensitivity at lower analyte concentrations, with the slopes predicting the sensitivity of coatings at low analyte concentrations. Figure 2(b) shows that the acoustic loss of NPC-coated SAW devices in air decreases with increasing mass density, i.e., the greater the film rigidity, the better the ultimate signal-to-noise (s/n) ratio. The NPC acoustic loss correlates with the isotherm slope, demonstrating that the acoustic loss (film rigidity) relates to sensitivity in very dilute analyte concentrations.

Figure 3(a) compares the adsorption isotherm for NPC with several commonly used sorption coatings for a common toxic chemical, chlorobenzene. Figure 3(b) extrapolates this power-law behavior toward infinite dilution, providing a prediction of the limits of detection. The y-axis minimum is set 10x above the s/n limit of the measurement system. The x-axis minimum is set to an analyte concentration of parts-per-billion (ppb). Only NPC exceeds this desired limit, and is > 6 orders of magnitude more sensitive than the best polymeric sensor coating. Similar data exist for many other gas analytes.

Significance—NPC-coated SAW devices offer the first hope toward ppb microsensor chemical detection. Compared to all existing sorbent coatings, NPC enhances sensitivity by multiple orders-of-magnitude and promises greater lifetime and field applications, including Homeland Defense, ES&H, and Industry.

Sponsors for various phases of this work include: Laboratory Directed Research & Development

Contact: Michael P. Siegal; Advanced Materials Sciences, Dept. 1126
Phone: (505) 845-9453, Fax: (505) 844-4045, E-mail: mpsiega@sandia.gov

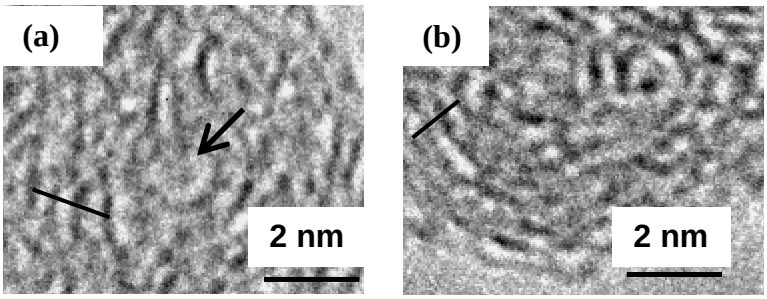

Figure 1. TEM images of NPC films with varying mass density: (a) 0.25 g/cm^3 and (b) 1.0 g/cm^3. The arrow in (a) points to a fullerene-sized void. The lines in each image show several aligned graphene sheet fragments.

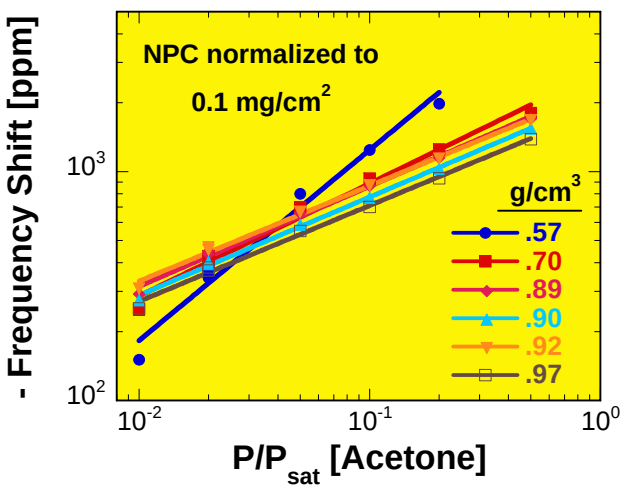

Figure 2(a). Log-log representation of acetone adsorption isotherms from SAW sensor devices coated with varying average NPC mass densities.

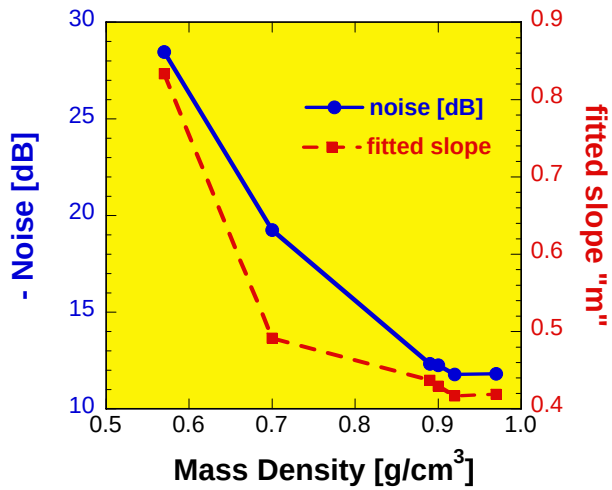

Figure 2(b): Network analysis of SAW acoustic loss and the fitted slopes from Fig. 2(a) as functions of average NPC mass density.

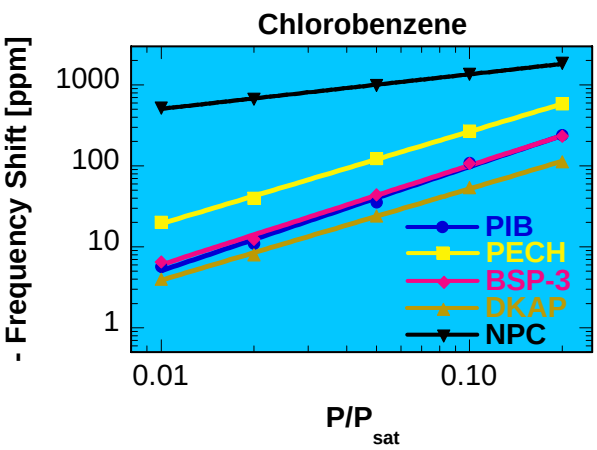

Figure 3(a). Log-log (power law) representation of SAW frequency shifts for various coatings responding to chlorobenzene from 1 – 20 % of its saturation pressure.

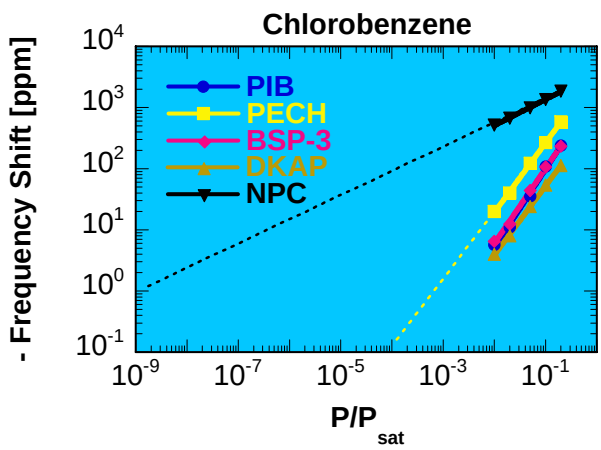

Figure 3(b). Extrapolation of power-law functions of isothermal adsorption data to very low (ppb) dilution limits for a variety of SAW sensor coatings.

Ferromagnetic Domains Induced by Dipolar Coupling?

by James E. Martin, Gene Venturini, and Dale Huber

Motivation—The basic description of ferromagnetic materials is that the magnetic spins on neighboring atoms experience quantum mechanical exchange coupling, which results in substantial parallel spin alignment well below the so-called Curie temperature. Statistical mechanical treatments such as the Ising model describe this emergence of spin alignment near the Curie point. However, exchange coupling is a local interaction, so the interaction between distant spins is dominated by dipole interactions. These interactions are weak, but are long range and have the important effect of causing the aligned spins to break into domains. In a soft magnetic material domain walls move freely, so domains form to nullify the net magnetic moment. Some years ago we had the idea that it should be possible to create a system where dipolar interactions, not exchange interactions, play the role of creating both ferromagnetic ordering and domain formation. This idea is based on using single-domain superparamag- netic nanoparticles as the fundamental entity, which interact only via dipolar interactions. Simulations showed us that organizing these particles into chain-like structures can cause ferromagnetic ordering and domain formation if the particle susceptibility exceeds about 5 (MKS). Because the interaction between domains is weak, the resultant nanocomposite will have an anomalously large susceptibility (Fig. 1). Such nanocomposites are expected to exhibit exceptional properties, such as large magnetostriction at small applied fields.

Accomplishment—Realizing a composite of high susceptibility nanoparticles proved a significant challenge. Standard synthetic routes for Fe and magnetite particles yielded a susceptibility well below the critical value of 5. After some effort, we were able to synthesize 5 nm Fe nanoparticles with nearly bulk saturation magnetism, and susceptibility in the range of 5-10. Due to their large susceptibility, these particles agglomerated so strongly that standard dispersion methods proved ineffective. Dispersion was ultimately achieved by magnetic mixing in an ac triaxial magnetic field. Chain-like structures were created by removing two field components, resulting in a uniaxial composite having an effective particle susceptibility of 181 and 9.9 parallel and perpendicular to the chains, respectively (Fig. 2).

Significance—The large susceptibility we have achieved is a strong indication of the formation of ferromagnetic domains due to dipolar coupling. This susceptibility exceeds by a factor of ten that which is possible in a composite of multidomain particles. Work is now underway to create nanocomposites in an elastomer, to use as an artificial muscle. In the presence of a magnetic field it is expected that such an elastomer will contract with considerable stress, this stress being proportional to the square of the susceptibility. Thus, these nanocomposites should exhibit the same magnetostriction as mesoscale magnetic composites, but with only 1% of the power.

Sponsors for various phases of this work include: DOE Office of Basic Energy Sciences

Contact: James E. Martin; Nanostructure & Semiconductor Physics, Dept. 1112
Phone: (505) 844-9125, Fax: (505) 844-4045, E-mail: jmartin@sandia.gov

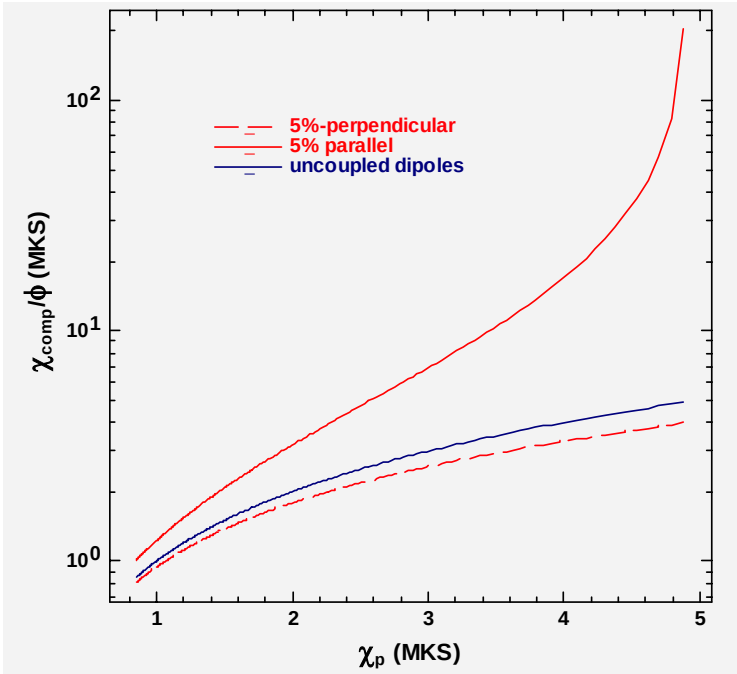

Figure 1. The specific susceptibility of a simulated 5% composite is compared to the susceptibility of a composite of uncoupled Langevin dipoles, where $\chi_{comp}/\phi = \chi_p$, and ϕ is the particle volume fraction. There is a slight suppression perpendicular to the chains. The enhancement becomes quite dramatic (but not infinite) near the critical value for domain formation, $\chi_p \approx 5$.

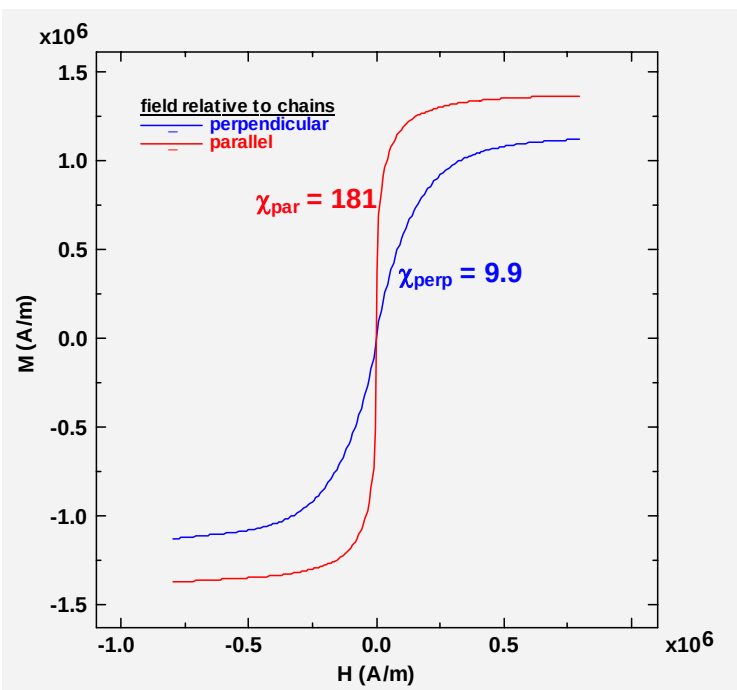

Figure 2. Magnetization curves of the nanocomposite show the enormous effect of structure on the susceptibility. Here the susceptibility parallel and perpendicular to the chains is contrasted.

Quantum Phenomena

Tunneling in Double Quantum Wire Devices

by M. P. Lilly, E. Bielejec, and J. L. Reno

Motivation—Interactions in nanoelectronic systems is a frontier area of basic science and possible novel application. One very good candidate for study is the system of coupled double quantum wires. Single one-dimensional (1D) wires are expected to have ground states that are strongly modified by Coulomb interactions. Coupled 1D wires have been used to probe many-body effects and have been suggested as a platform for quantum computation. In our experiments, we focus on the fundamental nature of the inter- and intra-wire interactions and examine the role of coherent tunneling of the electrons between the 1D wires.

Accomplishment—We have measured tunneling in a double quantum wire device and observed a narrow tunneling resonance that we attribute to 1D-1D tunneling. An image of the device is shown in Fig. 1a where the dark regions are the semiconductor and bright regions are metallic gates. A GaAs/AlGaAs electron bilayer with a 10 nm AlGaAs barrier between the two GaAs quantum wells is grown using molecular beam epitaxy (MBE). Electron beam lithography is used to pattern metallic gates above and below the electron layers. In the central region two pairs of split gates (only the two top gates are visible due to the high degree of alignment) form the top and bottom quantum wires. The gates on the left and right that span the image are used to establish independent contacts to the individual wires.

The conductance of both wires in parallel is shown in Fig. 1b. In the 1D regime, plateaus form as integer numbers of subbands in the quantum wires are occupied. The equally spaced white regions (I and III) are the well known quantized conductance steps of a single wire. In the center of the plot (region II), the structure of both wires overlap and form diamonds where two 1D wires coexist. One advantage of this device is our control of the number of occupied 1D subbands in each wire.

Tunneling measurements are presented in Fig. 2. In a tunneling measurement, electrons are transferred between the quantum wells conserving both energy and momentum. Fortunately, we have control over both energy (via a dc source-drain voltage between the layers) and momentum (using a parallel magnetic field to give the electrons a momentum "kick"). Due to limitation of lateral patterning, the active tunneling areas consist of two small 2D-2D coupled areas joined by the 1D-1D (diagram in Fig. 2), so both 2D-2D tunneling and 1D-1D tunneling signatures are expected. The tunneling conductance as a function of the voltage between the layers is shown in the main panel in Fig. 2 at three magnetic field values. The large peak at B=0 is easily identified as the 2D-2D contribution to the tunneling. The peak position, splitting with magnetic field and ultimate collapse at high field can be quantitatively understood through simple tunneling models. The side peak at $V_{source\text{-}drain}$ = -9 mV, however, is not expected from 2D-2D, and its position varies as the split-gate voltages are varied. The presence of this peak indicates 1D tunneling.

Significance—We have identified a 1D tunnel resonance in the vertically coupled 1D-1D device. Demonstration of the 1D resonance is the first step in future experiments on coherent tunneling oscillations. Coherent transport is one of the major advantages of nanoelectronics.

Sponsors for various phases of this work include: DOE Office of Basic Energy Sciences and Laboratory Directed Research & Development

Contact: Michael P. Lilly; Semiconductor Material & Device Sciences, Dept. 1123
Phone: (505) 844-4395, Fax: (505) 844-1197, E-mail: mplilly@sandia.gov

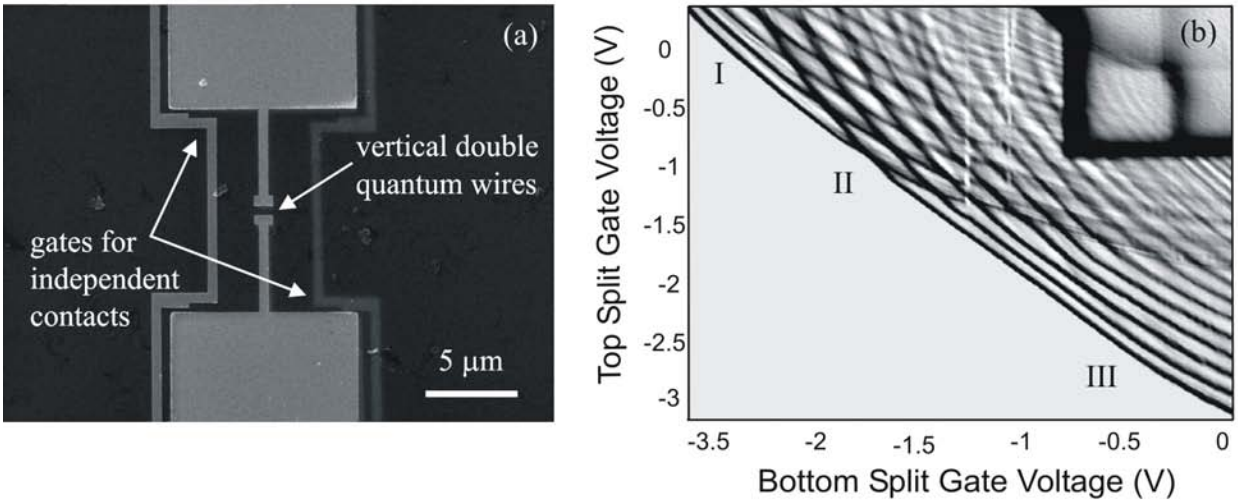

Figure 1. (a) Scanning electron microscope image of the double quantum wire device. (b) Parallel conductance of the double wire. White regions are dg/dV ~ 0 (plateaus) and dark regions are dg/dV > 0. Regions I and III are singly occupied 1D wires with evenly spaced quantized plateaus indicating high quality ballistic quantum wires. In region II, both wire are occupied, and the number of subbands can be controlled with the top and bottom split gate voltages.

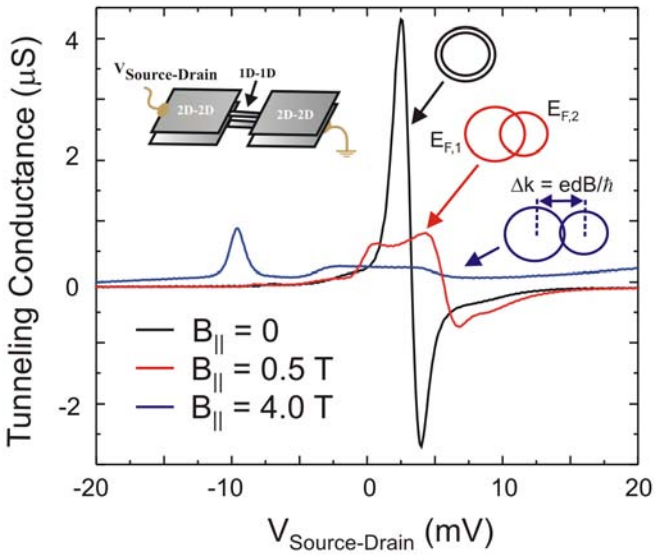

Figure 2. Tunneling conductance in the double quantum wire system. The diagram (upper left) indicates that both 2D-2D and 1D-1D tunneling can occur. The large peak at $V_{Source\text{-}Drain}$ = 2.5 mV that splits with a parallel magnetic field is due to 2D-2D tunneling. The parallel field separates the Fermi circle in k-space; tunneling only occurs at the intersection of the Fermi circles. The onset of a second peak at high field is due to 1D tunneling.

Hysteresis in Double Quantum Well Structure: Evidence for a Wigner Crystal

by W. Pan, J. L. Reno, and J. A. Simmons

Motivation—There is a great deal of current interest in the study of the double quantum well (DQW) structures. Compared to a single layer two-dimensional electron system (2DES), the existence of another layer introduces significant interaction effects between the two wells. Over the years, DQWs have proven to be ideal for studying the charge and energy transfer over multi-length scales, and many novel physical phenomena have been discovered. In addition, since the coupling (or separation) between the two wells can be precisely tuned from a few tenths of a nanometer to several microns, DQW structures have shown promise as possible electronic devices for next generation information processing.

Accomplishment—The electronic state of a 2DES in the presence of a high magnetic (B) field is the result of a competition between electrostatic effects and subtle quantum mechanics. At very high B field and low carrier concentration electrons are forced into tiny orbits as compared to their separation. As a result, the mutual wave function overlap vanishes and electrostatics dominates. An electron crystal, analogous to a classical Wigner crystal (WC) of point charges, is expected to form. At lower B field, or higher carrier concentration, wave function overlap is appreciable. This leads to the fractional and integer quantum Hall effect (FQHE and IQHE) states at Landau level filling $\nu = n/s$, where n is the carrier concentration and s is the magnetic flux density. The hallmark of a quantum Hall state is the vanishingly small diagonal resistance R_{xx} and precisely quantized Hall resistance $R_{xy} = (h/e^2)/\nu$.

In this research brief, we show experimental results of transport hysteresis in a DQW in the QHE regimes, and interpret it as the evidence of formation of a high B field WC. The sample structure is shown in Fig.1a. The ratio of top layer density (n_t) to bottom layer density (n_b), tuned by the front gate voltage (V_g), is $n_t/n_b \sim 1/6$ in Fig. 2a. Transport hysteresis is seen at the IQHE states $\nu = 1$ and 2. When $\nu < 1$ and the 2DES is in the FQHE regime, no hysteresis is seen. Surprisingly, in another type of measurement where B remains constant and V_g is varied (Fig. 2b), prominent hysteresis is observed for $\nu < 1$ at the same experimental parameters, *e.g.*, $V_g = -0.79$V and B =12.9T.

The huge transport hysteresis in the V_g sweeps is striking. We believe it is new evidence of formation of a high B field WC, in the top layer. When V_g is swept, electrons are added to or removed from the top layer. Since the WC is weakly pinned by residual disorders and the 2DES is insulating, it then requires a finite time for the carriers in the top layer to reorder and reach the final equilibrium state. This finite time constant, combined with a finite V_g sweep rate, can cause hysteresis. On the other hand, in the B sweeps, there is no such charging/discharging process. Consequently, no hysteresis is expected or observed.

Significance—Adding a high-density, high-mobility 2DES close to a low-density one allows us to study some physical properties of WCs that might not be accessible in a single layer system. This novel approach, combined with other well-established experimental techniques, such as Coulomb drag and photoluminescence, is expected to shed more light on the physical properties of the high B field Wigner crystal phase, which has been a challenging problem for many decades.

Sponsors for various phases of this work include: DOE Office of Basic Energy Sciences

Contact: Wei Pan; Semiconductor Material & Device Sciences, Dept. 1123
Phone: (505) 284-9545, Fax: (505) 844-3211, E-mail: wpan@sandia.gov

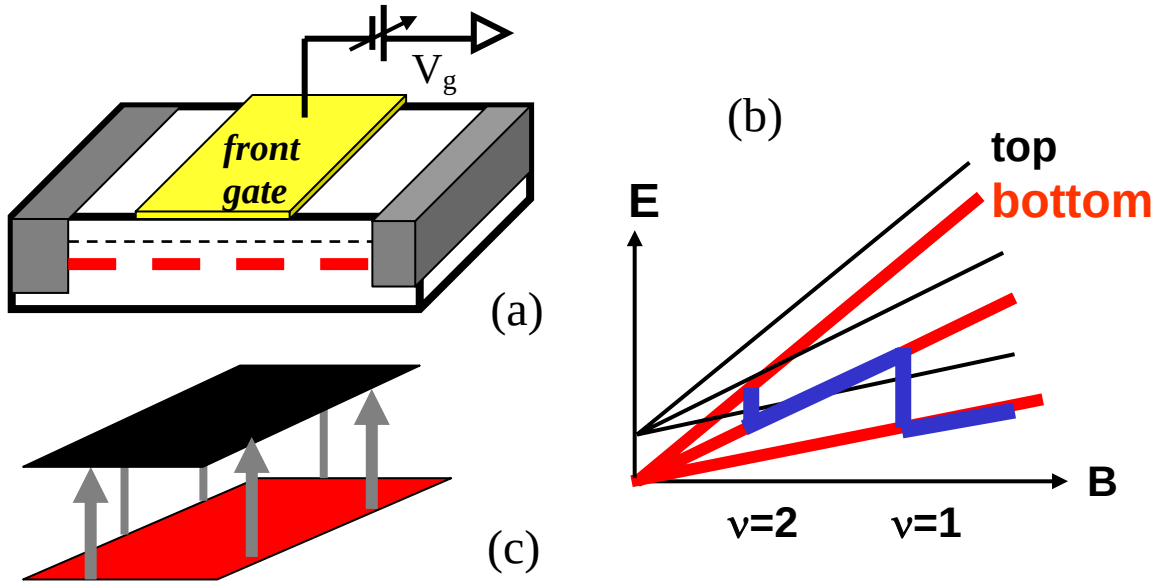

Figure 1. (a) Schematic of sample structure. The black thin dashed line represents the top layer and the red thick dashed line the bottom. (b) The transport hysteresis can be understood as spontaneous charge transfer between the two quantum wells. When the bottom layer enters into an IQHE state, its Fermi level (blue line) jumps from one Landau level to another. Consequently, the chemical potential between the two QWs becomes unbalanced. In reaching an equilibrium state, a spontaneous charge transfer from one QW to the other will occur, through ohmic contacts (Fig. C). Since the bottom QW is in the IQH regime and the bulk is insulating, redistribution of the transferred charges would take a finite time to finish. This finite time constant, combined with the finite sweeping rate of B field, gives rise to hysteresis in electronic transport. Once $\nu < 1$ is reached, the Fermi level will stay in the lowest Landau level and experience no more sudden jumps. Thus, no hysteresis is expected, consistent with our results.

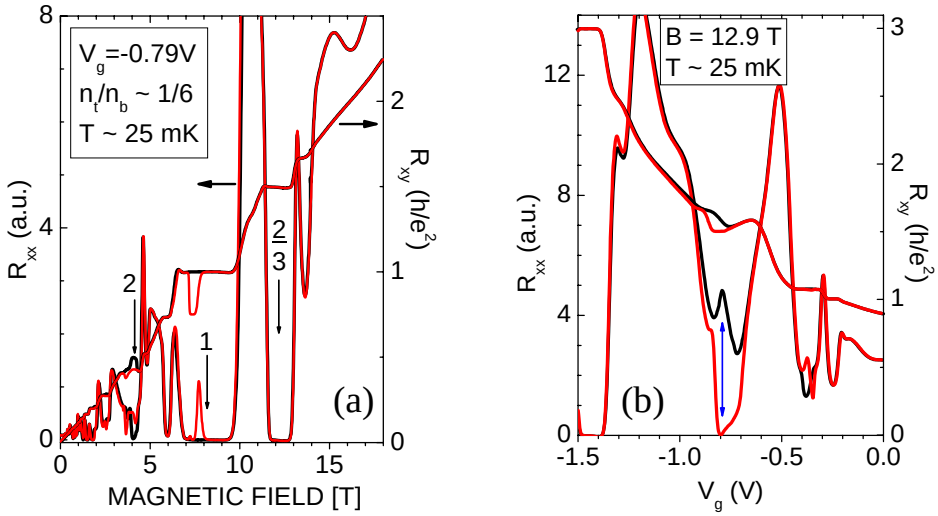

Figure 2. (a) No hysteresis is seen around V=2/3 at V_g = -0.79 V and B = 12.9 T in B sweeps (black curve, B up; red, B down). (b) Huge hysteresis is seen in V_g sweeps at the same experimental parameters, V_g =-0.79 V and B=12.9 T (red curve, V_g up; black, V_g down).

Dipolar Centers in Quantum Paraelectrics: Mn and Fe in $KTaO_3$

by E. L. Venturini and G. A. Samara

Motivation—Random lattice disorder produced by chemical substitution in ABO_3 perovskites can lead to the formation of dipolar impurities and defects that influence the static and dynamic properties of these materials. Because of the high polarizability of the ABO_3 host lattice, associated with its soft ferroelectric mode, dipolar entities polarize regions around them forming polar nano-/microdomains whose size is determined by the temperature-dependent correlation length, r_c, in the host. When these dipolar entities possess more than one equivalent orientation, they may undergo dielectric relaxation in an applied *ac* field. At sufficiently low concentration, each polar domain behaves as a non-interacting dipolar entity with a single relaxation time, but at higher concentrations of disorder, the polar domains can interact, leading to the formation of a glass-like relaxor state, or even an ordered ferroelectric state.

Accomplishment—We have investigated the dipolar relaxational properties of the disordered quantum paraelectric $KTaO_3$, where the disorder is produced by dilute Mn and Fe impurities. A significant aspect of this work is the influence of hydrostatic pressure on these properties. $KTaO_3$ is a model soft ferroelectric (FE) mode system whose long wavelength TO phonon frequency softens with decreasing temperature (T), but never quite vanishes because of quantum fluctuations at sufficiently low temperatures. The soft mode imparts unto $KTaO_3$ a strongly T-dependent r_c, making the behavior of dipolar centers in this crystal quite interesting. We have determined the temperature and pressure dependencies of r_c as shown in Fig. 1. The Mn^{2+} center results from the off-center displacement ($\cong 0.9$ A) from the K^+ site along one of six equivalent [001] directions. At a concentration of 0.01 at.%, the Mn^{2+} centers are, on the average, farther apart than r_c and there is no measurable anomaly in the real part of the dielectric susceptibility, but there is a loss ($\tan\delta$) peak at ~50K. r_c at this temperature is two unit cells long ($2a_o$ in Fig. 1), and thus there is no overlap or correlations among the polar nanodomains. At a concentration of 0.3 at.% Mn, however, one in every ~300 unit cells has a Mn^{2+} ion, and in this case, for $r_c = 2a_o$ there is some overlap and correlations among the nanodomains. The result is weak relaxor behavior that is reflected in both the dielectric susceptibility (or ε') and $\tan\delta$ as shown in Fig. 2. Pressure reduces r_c (Fig. 1) resulting in weaker correlations and smaller ε' and $\tan\delta$ anomalies.

Iron produces two dipolar centers in $KTaO_3$, an Fe^{3+}-oxygen interstitial complex and an Fe^{2+} center most likely produced by an off-center position of Fe^{2+}. Unlike Mn doping, Fe doping at the 0.3 at.% level does not lead to any measurable anomalies in $\varepsilon'(T)$, the Fe centers behaving as non-interacting nanodomains with $\tan\delta$ peaks at ~150K and ~185K (Fig. 3). The absence of $\varepsilon'(T)$ anomalies is easily understood from the results in Fig. 1. In the 150-200K range, r_c is only $\cong 1a_o$ so that the nanodomains are much smaller than in the case of Mn (where $r_c \approx 2a_o$) at its $\tan\delta$ peak and, thus, there is essentially no overlap or correlation among the Fe center.

Significance—Soft mode systems such as $KTaO_3$ are ideal hosts for studying the onset and evolution of correlations among dipolar centers because the correlation length for dipolar interactions in these hosts can be delicately tuned by either temperature or pressure, as shown in Fig. 1. This property is unique to soft mode systems where the soft mode frequency is determined by a delicate balance between short-range and coulombic forces. In turn, the dielectric signature of dipolar centers provide an indirect probe of soft mode behavior.

Sponsors for various phases of this work include: DOE Office of Basic Energy Sciences

Contact: E. L. Venturini, Nanostructure & Semiconductor Physics, Dept. 1112
Phone: (505) 844-7055, Fax: (505) 844-4045, E-mail: elventu@sandia.gov

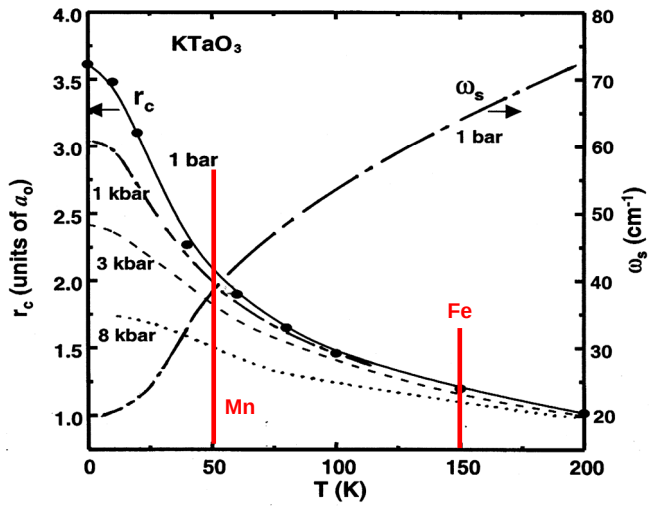

Figure 1. Temperature dependence of the ferroelectric soft mode frequency (ω_s) and of the correlation length (r_c) for dipolar correlations of $KTaO_3$. The influence of pressure on $r_c(T)$ is also shown.

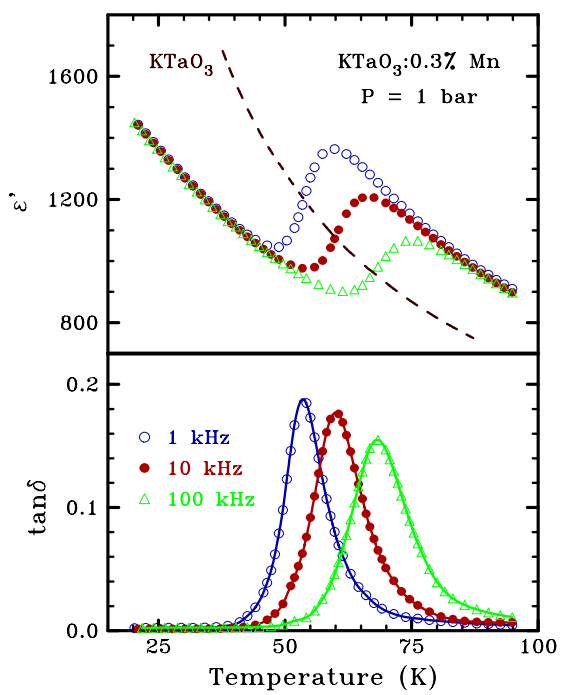

Figure 2. Temperature dependence of ε′ and tan δ at 1 bar of a $KTaO_3$ crystal with 0.3 at % Mn showing the relaxational character of the response. The non-relaxational ε′(T) response of undoped $KTaO_3$ is shown (dashed line) for comparison.

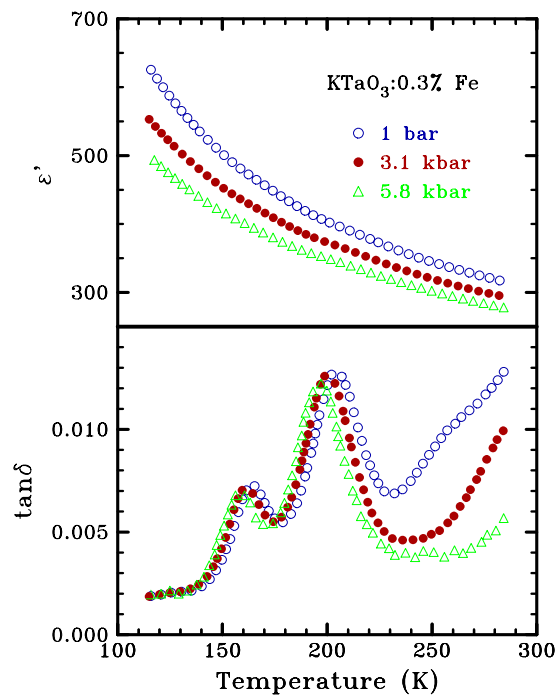

Figure 3. Temperature dependences of ε′ and tan δ at different pressures of a $KTaO_3$ crystal doped with 0.3 at % Fe.

Recent Awards and Prizes

Recent Awards and Prizes

National and International Awards

2004 — **National Academy of Engineering (NAE) Election:** "For leadership and distinguished research in the epitaxy of dissimilar materials." (Julia Phillips)

2002 — **Plasma Prize for Science and Technology** presented by the American Vacuum Society, Plasma Science and Technology Division, for innovative development of diagnostics and insightful fundamental studies of low temperature plasmas and their successful application to the advancement of plasma technologies. (Greg Hebner)

— **National Academy of Engineering (NAE) Election:** For originating the field of strained-layer superlattices and related structures, which has led to revolutionary advances in electronics and optoelectronics." (Gordon Osbourn)

DOE Basic Energy Sciences, Material Science Awards

2002 — **BES "Chunky Bullet Shootout":** Winner for "Ultrasensitive Chemical Sensors for Counter Terrorism Applications." (Jim Martin and Bob Anderson)

Other Awards

2004 — **American Vacuum Society (AVS) Fellow Appointment:** "For developing innovative optical, microwave, and electrical diagnostics of plasma sources." (Greg Hebner)

— **Optical Society of America (OSA) Fellow Appointment:** "For contributions to the field of nonlinear optics." (Arlee V. Smith)

— **R&D100 Award**: "Cantilever Epitaxy and Growth of Low-Dislocation Gallium Nitride." (Inventors: C. I. H. Ashby, D. M. Follstaedt, C. C. Mitchell and J. Han; Developers: A. A. Allerman, K. H. A. Bogart, K. Cross, A. J. Fischer, K. Fullmer, L. Griego, D. D. Koleske, N. A. Missert, M. P. Moran, A. K. Norman, A. Ongstad, G. M. Peake, P. Provencio and J. Sergeant)

— **Wilbur Lucius Cross Medal Recipient** – highest award of the Yale University Graduate School Alumni Association: Cited for "scientific achievements, leadership in research management, outstanding service to the nation, and inspiration as a role model for young women in science and engineering." (Julia Phillips)

2003 — **2003 President's Silver Quality Award:** "Weapon Program Phase 7 Process Development" Team. (David Walsh)

— **APS Fellow Appointment:** Elected Fellow of the American Physical Society (APS) "for his pioneering and continued contributions to the metal-organic chemical vapor deposition of compound semiconductors, especially strained layer superlattices and Bragg reflectors for use in optoelectronic devices for industrial applications." (Bob Biefeld)

— **AAAS Fellow Appointment:** Elected Fellow of the American Association for the Advancement of Science (AAAS) for his "research advances, particularly the development and exploitation of interfacial force microscopy, leading to fundamental understanding of the interaction of solid surfaces with the environment." (Jack Houston)

— **Humboldt Research Award** for early experimental research on electrical discharge excimer lasers and for recent accomplishments on the microscopic theory of semiconductor lasers. (Weng Chow)

— **National Associate of the National Academies** (NAS, NAE, Institute of Medicine, NRC): Awarded for "extraordinary service to the National Academies." (Julia Phillips)

— **Nellie Yeoh Whetten Award** from the AVS Science and Technology Society for recognition of excellence in graduate research by a woman in a scientific or technical area of interest to the AVS. (Meredith Anderson)

2002 — **APS Fellow Appointment:** Elected Fellow of the American Physical Society (APS) "for pioneering work in applying scanning probe microscopy techniques to elucidate the nanometer scale electronic and optical properties of novel materials – in particular the physics related to defect." (Julia Hsu)

— **AAAS Fellow Appointment:** Elected Fellow of the American Association for the Advancement of Science (AAAS) for her "seminal research on growth and properties of magnetic, superconducting, and optical thin films and for leadership in the management of interdisciplinary research." (Julia Phillips)

— **APS Fellow Appointments:** Elected Fellows of the American Physical Society (APS) for:

  — contributions to the fundamental understanding of the gas-phase and surface chemical processes in the chemical vapor deposition of semiconductor materials. (Michael E. Coltrin)

  — outstanding contributions to the physics of tunneling in two dimensional electronic materials, including fractional quantum Hall and double quantum well systems. (Jerry A. Simmons)

  — pioneering studies of atomic-scale, kinetic, and thermodynamic aspects of the morphology of Si surfaces and significant innovations in scanning tunneling microscopy. (Brian S. Swartzentruber)

— **Federal Laboratory Consortium (FLC) Excellence in Technology Transfer Award** for the development of instrumentation and software analysis to measure, *in situ*, thin film growth rates and wafer temperature during the fabrication of compound semiconductor optoelectronic device structures. (Bill Breiland)

— **Horizon Award** presented by the New Mexico Commission on the Status of Women and the U. S. Department of Labor Women's Bureau: The recipient of this award must be a New Mexico resident who has contributed significantly to the acceptance and advancement of women in Science, Math, Engineering, and Technology. (Julia Phillips)

— **Humboldt Research Award** in recognition of research accomplishments in the area of polymer modeling, which will be used to further collaborations with colleagues in Germany. (Gary Grest)

— **Publication in "All Star" collection** of 25 significant and most cited articles that appeared in ECS journals since 1940. (M. E. Coltrin, R. J. Kee, and J. A. Miller)
— **Sandia Fellow Appointment:** By distinguishing himself and Sandia through his technical novations in several very important fields, including strained-layer technology, the application of biological vision and pattern recognition systems to computer-based sensor systems, and collective intelligence and self-organizing systems. (Gordon Osbourn)
— **Weapon Award of Excellence**: The CY 2001 Weapons Award of Excellence winners included two teams at Sandia Laboratories led by Center 1100:
  — (1) The Neutron Tube Production R&D Team for applying scientific tools and methods to improve yield and reliability of Neutron Tubes. (Paul A. Miller, Team Lead, et al.)
  — (2) The Photonic Driver Team for developing a Photonic Driver capability for microscale shock wave physics research. (Bob Setchell, Team Lead, et al.)

2001 — **APS Fellow Appointment:** Elected Fellow of the American Physical Society (APS) for pioneering work in applying scanning probe microscopy techniques to elucidate the nanometer scale electronic and optical properties of novel materials, in particular the physics related to defect. (Julia Hsu)
— **The Lockheed Martin NOVA Award:** The NOVA Awards honored a Sandia/industry team that developed the first 1.3-micron electrically pumped vertical cavity surface emitting laser (VCSEL). (John Klem, Andy Allerman, Kent Choquette, et al.)

Patents Awarded

2004

— Patent 6,790,476
Title: Strong Adhesion and Wetting of Metals to Oxide Surfaces
Originator: Dwight Jennison

— Patent 6,775,314
Title: Distributed Bragg Reflector Using AlGaN/GaN
Originator: Stephen Lee

— Patent 6,775,054
Title: Image Rotating 4-Mirror Ring Optical Parametric Oscillator
Originator: Arlee Smith and Darrell Armstrong

— Patent 6,718,821
Title: Multi-Axis Force-Feedback Sensor with Laser Interferometer Displacement Detection
Originator: Jack Houston

— Patent 6,627,048
Title: Laser Interferometry Force-Feedback Sensor for an Interfacial Force Microscope
Originator: Jack Houston and William L. Smith

2003

— Patent No. 6,665,329
Title: Broadband Visible Light Source Based on ALLNGAN Light Emitting Diodes
Originator: Mary H. Crawford

— Patent No. 6,663,697
Title: Microfabricated Packed Gas Chromatographic Colum
Originator: Carolyn M. Matzke

— Patent No. 6,647,034
Title: Method To Improve Optical Parametric Oscillator Beam Quality
Originator: Arlee V. Smith

— Patent No. 6,647,033
Title: Optical Parametric Oscillators with Improved Beam Quality
Originator: Arlee V. Smith, and William J. Alford

— Patent 6,627,048
Title: Reductive Precipitation of Metals Photosensitized by Tin and Antimony Porphyrins
Originator: John A. Shelnutt

— Patent 6,608,846
Title: Bistable Laser with Multiple Coupled Active Verticle-Cavity Resonators
Originators: Arthur J. Fischer, Weng W. Chow, Kent D. Choquette

— Patent 6,600,761
Title: Semiconductor Laser with Multiple Lasing Wavelengths
Originators: Arthur J. Fischer, Weng W. Chow, Kent D. Choquette

— Patent 6,599,362
Title: Substrate Texturing for Cantilever Epitaxy of III-N and Other Materials
Originators: Carol I. Ashby, Christine C. Mitchell, David M. Follstaedt, Jung Han (Yale University)

— Patent 6,570,333
Title: A Method for Generation of Surface Plasma Using Radio-frequency Power Across Pairs of Insulator Conductors where the Plasma Can Cover a Variety of Flat or Curved Surfaces, such as Aircraft Surfaces in High-altitude Flight Operation
Originators: Paul A. Miller, Ben P. Aragon

— Patent 6,567,454
Title: Coupled-resonator Vertical-cavity Lasers with Two Active Gain Regions
Originators: Arthur J. Fischer, Weng W. Chow, Kent D. Choquette

— Patent 6,552,338
Title: Ion Photon Emission Microscope
Originators: Barney L. Doyle

— Patent 6,504,859
Title: Light Sources Based on Semiconductor Current Filaments
Originators: Weng Chow, et al.

— Patent 6,479,919
Title: Solid-state Nuclear-to-electric Energy Conversion: Beta-voltaic Cells of Icosahedral Borides
Originators: Terrence L. Aselage, David Jacob Emin

— Patent 6,406,931
Title: Conductivity Control of GaN Using LT AIN Buffer Layers
Originators: Jeffrey J. Figiel, Jung Han (Yale University)

2002
— Patent 6,406,931
Title: Conductivity Control of GaN Using LT AIN Buffer Layers
Originators: Jeffrey J. Figiel, Jung Han
— Patent 6,393,038
Title: Frequency-doubled Vertical External Cavity Surface Emitting Laser
Originators: William J. Alford, Mary H. Crawford, Andrew A. Allerman, Thomas D. Raymond
— Patent 6,391,393
Title: Nonvolatile, Dual Level, Magnetic Storage Media
Originators: James E. Martin, Chris P. Tigges, Robert A. Anderson, Eugene L. Venturini
— Patent 6,375,759
Title: Batch Fabrication of Precision Miniature Permanent Magnets
Originators: Terry J. Garino, Eugene L. Venturini, Todd R. Christenson
— Patent 6,368,775
Title: 3-D Photo-Patterning of Refractive Index Structures in Photosensitive Thin Films
Originators: Barrett G. Potter, Jr.; Kelly Simmons Potter
— Patent 6,365,428
Title: Buried Distributed Bragg Reflector for Planar Waveguide Applications
Originators: Walter J. Zubrzycki, Gregory A. Vawter, Andrew A. Allerman
— Patent 6,304,675
Title: A New Cluster Analysis Method
Originators: Gordon C. Osbourn, Rubel F. Martinez

2001
— Patent 6,291,823
Title: Ion Induced Electron Emission Microscopy
Originators: Barney L. Doyle, Gyorgy Vizkelethy, Robert A. Weller (Vanderbilt Univiversity)
— Patent 6,290,868
Title: Field-structured Chemical Sensor
Originators: Robert C. Hughes, James E. Martin, Robert A. Anderson
— Patent 6,288,394
Title: Highly Charged Ion Based Time of Flight Emission Microscope
Originators: Barney L. Doyle, LLNL Team
— Patent 6,258,615
Title: Multiple Wavelength Vertical Cavity Resonance Devices Fabricated by Selective Area Epitaxy in MOVPE
Originators: Michael E. Coltrin, Hong Q. Hou, Kent D. Choquette

— Patent 6,252,287
Title: Heterojunction InGaAsN Solar Cells
Originators: Steven R. Kurtz, Eric Daniel Jones, Andrew A. Allerman, John F. Klem
— Patent 6,248,992
Title: Tailored Doping Profile for Photoconductive Semiconductor Switch
Originators: Guillermo M. Loubriel, Darwin James Brown, Fred J. Zutavern, Wesley D. Helgeson, Martin W. O'Malley, Gary J. Denison, Charles T. Sullivan, Hong Q. Hou, Albert G. Baca, Thomas E. Zipperian, Andrew A. Allerman, Harold P. Hjalmarson
— Patent 6,245,200
Title: Visible Light Photooxidation of Toxic Organic Chemicals Using Nanoscale MoS2
Originator: Jess P. Wilcoxon
— Patent 6,194,769
Title: Sensor Devices Based on Field-structured Composites
Originators: Robert C. Hughes, James E. Martin, Robert A. Anderson
— Patent 6,187,592
Title: Method for Determining Hemoglobin Concentration in Individual Red Blood Cells
Originator: Paul L. Gourley

Government Advisory Boards and Professional Societies/International Committees/Journals

Government Advisory Boards

Argonne National Laboratory
— Materials Science Division External Review Committee; Julia Phillips, Chair; 2003

Department of Energy, Office of Basic Energy Sciences
— Materials Sciences and Engineering Program Committee of Visitors; Julia Phillips, member; 2003
— Scientific User Facilities Division Committee of Visitors; Julia Phillips, member; 2004
— Review of Nanoscience Research Center Operational Plans; Julia Phillips, member; 2004

Lawrence Berkeley National Labs (LBNL) Committee
— Accelerator and Fusion Research/Directors Review Committee; Barney Doyle, member; 2003

National Institute of Biomedical Imaging and Bioengineering (NIBIB)
— National Institutes of Health (NIH) Study Panel; Alan Burns, Special Emphasis Panel member; 2003

National Research Council
— Committee on Nanotechnology for the Intelligence Community; Wil Gauster, member, 2003-2004
— National Materials Advisory Board: Julia Phillips, member, 1999-2001; Chair, 2002-2004
— Board on Physics and Astronomy; Julia Phillips, member; 2000-2006
— National Academy of Engineering, Symposium on Frontiers of Engineering; Julia Hsu, participant; 2003
— U.S. Liaison Committee for the International Union of Pure and Applied Physics; Julia Phillips, member; 2000-2002
— Committee on Materials Research for the Defense-After-Next; Julia Phillips, member; 1999-2002
— National Academy of Sciences, Symposium on Frontiers of Science; Julia Hsu, participant; 2001
— Solid State Sciences Committee; Julia Phillips, Vice Chair; 1998-2001

National Science Foundation
— Advisory Committee, Mathematics and Physical Sciences Directorate; Julia Phillips, member; 2000-2003

Professional Societies/International Committees/Journals

American Association for the Advancement of Science (AAAS)
— Council; Julia Phillips, member; 2003-2005
— Physics Section Nominating Committee: Julia Phillips, member, 2003-2004; Chair, 2005
— Physics Section; Julia Phillips: Chair-elect, Chair, Past Chair; 2003-2005

American Association for Crystal Growth
— 15th American Conference on Crystal Growth and Epitaxy; Bob Biefeld, Co-chair; 2002

Professional Societies/International Committees/Journals (continued)

Air Force Office of Scientific Research (AFOSR)

— Plasma-assisted Combustion AFOSR Review Panel; Greg Hebner and Paul Miller, members; 2004

American Physical Society (APS)

— Division of Condensed Matter Physics (DCMP); Julia Phillips, Vice-Chair, 2005; Chair-Elect, 2006; Chair, 2007
— Forum on Industrial & Applied Physics (FIAP): Mark Lee, Vice-Chair, 2005; Chair-Elect, 2006; Chair, 2007
— Committee on Meetings; Mark Lee, member; 2003-2006
— Maria Goeppert Mayer Award Committee: Julia Phillips, member, 2001; Chair, 2002
— Division of Materials Physics (DMP) Executive Committee; Julia Hsu, Member-at-Large; 2004-2006
— March Meeting; Brian Swartzentruber, Symposium Organizer; 2004

American Vacuum Society (AVS)

— Board of Directors; Neal Shinn, member; 2003-2006
— 39th Annual Meeting of the New Mexico Chapter; Kate Bogart, Symposium Chair; 2003
— Chapters, Divisions, Groups Committee; Neal Shinn, member; 2002-2004
— Surface Science Division; Neal Shinn, Chair; 2001-2002

Army Research Office (ARO) Multi University Research Initiative (MURI)

— Technical Advisory Committee; Mark Lee, member; 2001-2002

BES Materials Council

— Workshop on Issues in Nanomechanics; Charles Barbour, Panel Chair; 2003

Gaseous Electronics Conference (GEC)

— 56th Annual Meeting; Greg Hebner: Chair-elect, Chair, Past Chair; 2003-2006

Institute of Electrical and Electronics Engineers (IEEE)

— Transactions on Plasma Science, 4th issue on Images in Plasma Science; Greg Hebner, Guest Editor, 2004-2005
— Nuclear and Plasma Sciences Society (NPSS); Paul Dressendorfer, Editor-in-Chief; 2002-present
— NPSS Radiation Instrumentation Steering Committee; Paul Dressendorfer, member; 1997-present
— Nuclear and Plasma Science Society (NPSS) Administrative Committee; Paul Dressendorfer, member; 1993-present
— Transactions on Nuclear Science; Paul Dressendorfer, Editor; 1993-present
— NPSS Radiation Effects Steering Group (RESG); Paul Dressendorfer, member; 1988-present

International Conference on Ion Beam Analysis

— Gyorgy Vizkelethy and Barney L. Doyle, Chairmen; 2003
— International Committee; Gyorgy Vizkelethy and Barney L. Doyle, members; 2003

Professional Societies/International Committees/Journals (continued)

International Conference on Nuclear Microscopy Technology and Applications
— International Committee, Barney L. Doyle; 1990-2004

International Journal of PIXE (IJPIXE)
— Editorial Board, Barney Doyle; 1996-present

International Union for Vacuum Science, Technique, and Applications (IUVSTA)
— Surface Science Electoral College; Neal Shinn, United States Representative; 2001-2004
— Surface Science Division: Neal Shinn, Chair, 2004-2007; Secretary, 2001-2004
— Surface Science Program, 15th International Vacuum Congress; Neal Shinn, Surface Science Chair; 2001
— Surface Science Program, 16th International Vacuum Congress; Neal Shinn, member; 2004

Industrial and Professional Advisory Council for the Engineering Science and Mechanics Department at Penn State University
— Neal Shinn, member; 2003-2006
— Wil Gauster, member; 2001-2004

Ion Beam Modification of Materials Conference
— International Committee; Charles Barbour, member; 1996-present

Journal of Chemical Physics
— Jim Martin, Editorial Board; 2003-2006

Journal of Crystal Growth
— Bob Biefeld, Associate Editor for the Journal of Crystal Growth for subject areas: "Epitaxial Growth and Nanostructures"; 2004-2006

Journal of Vacuum Science and Technology
— Neal Shinn, Associate Editor; 2002-present

Materials Research Society (MRS)
— External Relations and Volunteer Involvement (ERVI) Committee; Jerry Floro, Chair; 2004
— Meetings: Charles Barbour, Chair, Spring 2006; Julia Hsu, Chair, Fall 2004; Jerry Floro, Chair, 2001
— Board of Directors: Jerry Floro, member, 2002-2004; Julia Hsu, member, 2005-2007
— Task Force on Meeting Program/Board of Directors Interactions; Julia Phillips, Chair; 2003
— Task Force on Government Agencies Committee; Charles Barbour, member; 2002
— Symposium: Sean Hearne, Organizer, Fall 2002; Tom Friedmann, Organizer, 2001; Alan Wright, Organizer, Fall 2001
— Membership Committee; Charles Barbour, Chairman; 2001-present

Professional Societies/International Committees/Journals (continued)

National Institute of Health (NIH)

— Center of Biomedical Research Excellence (COBRE), External Advisory Board; Darryl Sasaki, member; 2001

— Biomedical Imaging & Bioengineering Study Panels: Small Business Novel Technologies for In Vivi Imaging and Image-guided Cancer Interventions, Shared Instrumentation, and Improvements in Imaging Methods and Technologies; Alan Burns, member; 2004

NASA Review Panel

— Bob Biefeld, member; 2002

Nuclear Instruments and Methods in Physics Research, Section B: Beam Interactions with Materials and Atoms

— Barney Doyle, Editorial Board; 2003-2006

Optical Society of America (OSA)

— Committees for 2000 Awards; Arlee Smith, Max Born Award Member; 2000

Radiation Effects in Insulators Conference

— Charles Barbour, International Committee member; 1997-present

Physical Review E

— Gary Grest, Senior Editor; 2002-present

The Minerals, Metals, and Materials Society (TMS)

— Electronic Materials Committee; Julia Hsu, member; 2000-2006

— Electronic Materials Committee: Bob Biefeld, member, 2002-present; Secretary, 2002-2004

Twelfth International Conference on Metal-Organic Vapour Phase Epitaxy

— Bob Biefeld, Organizing Committee member; 2002

US-Organometallic Vapor Phase Epitaxy Workshop

— Bob Biefeld, Organizing Committee member; 2002

Resources and Capabilities

Resources and Capabilities
Physical and Chemical Sciences Center

— Diagnostics and Characterization —

Atomic-Level Imaging and Spectroscopy

We have developed technical capabilities in:

- Scanning Tunneling Microscopy (STM) with the ability to track the diffusion of single atoms on surfaces,
- Low Energy Electron Microscopy (LEEM) with nanometer spatial resolution and real-time spectroscopic imaging capability at sample temperatures from 300K to over 1000K,
- Field Ion Microscopy (FIM) with single atom resolution and accurate temperature control to 1 Kelvin,
- Atom Probe Microscopy (APM) with pulsed laser desorption capability,
- Interfacial Force Microscopy (IFM) with feedback for accurate, simultaneous normal and frictional force profile measurements for the quantitative study of adhesion, tribology, and nanomechanics, and
- Atomic force microscopy (AFM) for imaging, force profiling, electrical measurements, and manipulation of individual biomolecules in fluid environments with simultaneous fluorescence detection.

Scanning Probe Metrology

We have developed a unique wide-field scanning Interfacial Force Microscope with calibrated force detection for the dynamic measurement of normal and lateral forces of micro-electrical-mechanical system components in operation.

Simultaneous Measurement of H, D, and T in Materials

We have designed and implemented a new ion beam analysis (IBA) system to simultaneously measure the absolute quantities of H, D, and T in materials using an elastic recoil detection (ERD) technique. The technique uses an E-dE detector arrangement, or particle telescope, to provide for accurate separation of the H, D, and T signals. The system can also simultaneously acquire information about medium and high Z elements in the sample using Rutherford backscattering spectrometry (RBS). Measurement of other light elements is possible using the nuclear reaction analysis (NRA) technique, which is isotope specific. The system will have an accuracy of < 2% for measuring the composition of solids.

Ion Accelerator Nuclear Microprobe

We have facilities for nuclear microscopy and radiation effects microscopy based on a 6 MV tandem Van de Graaff ion accelerator. We generate ion species from hydrogen to gold for both radiation effects research and quantitative high-energy ion beam analysis of materials containing light elements (hydrogen to fluorine) using heavy ion elastic recoil detection (ERD) and heavy elements using high-energy backscattering spectrometry, and Heavy Ion Backscattering (HIBS). An external Micro Ion Beam Analysis (X-MIBA) capability enables multi-elemental analysis and ion irradiation of samples, which are vacuum incompatible or extraordinarily large. The Sandia Nuclear Microprobe with micrometer size high-energy ion beams is used to study materials and devices. Special emphasis is given to the evaluation of the radiation hardness of microelectronic devices using three new advanced diagnostic techniques invented at Sandia: Single-Event-Upset Imaging, Ion-Beam-Induced-Charge-Collection Imaging (IBICC), and time-resolved IBICC. A recent development is the Ion Electron Emission Microscope (U. S. Patent No. 6,291,823 and 2001 R & D-100 Award winner), which can perform radiation microscopy using very highly ionizing particles without focusing the ion beam.

Materials Microcharacterization

Our capabilities in this area include optical microscopy, scanning, electron microscopy, analytical transmission electron microscopy, double crystal x-ray diffraction, ion beam analysis of materials (RBS, channeling, ERD, PIXE, NRA), Hall measurements, microcalorimetry, photoluminescence, light scattering, electronic transport, deep level spectroscopy, magnetization, and dielectric and magnetic susceptibilities.

Surface and Interface Spectroscopies

We maintain capabilities in Auger electron spectroscopy (AES), x-ray photoelectron spectroscopy (XPS), low energy electron diffraction (LEED), thermal desorption spectroscopy (TDS), and infrared reflectance-absorption spectroscopy (IRAS) for quantitative determination of materials structure and chemical composition.

Vision-Science Laboratory

The vision science laboratory consists of state-of-the-art hardware and software capabilities for carrying out video inspection, multi-spectral image analysis, and sensor-based pattern recognition. These capabilities are used in applications ranging from microsensor-based chemical detection and recognition to automated video/SEM inspection of semiconductor materials and circuits. This is a new approach to pattern recognition, coupling perception-oriented research with machine algorithms.

Chemical Vapor Deposition (CVD)

Our experimental tools for investigating CVD include optical probes (such as reflectance-difference spectroscopy and emissivity correcting pyrometry) for gas-phase and surface processes, a range of surface analytic techniques, molecular beam methods for gas/surface kinetics, and flow visualization techniques. These tools are integrated in a unique manner with research CVD reactors and with advanced chemistry and fluid models.

Growth Science Laboratory

Capabilities for in situ characterization of materials during thin film deposition, molecular beam epitaxial growth, and low energy ion beam simulated growth, include intensity profile sensitive reflection high energy electron diffraction (RHEED) for surface structure, energy dispersive x-ray reflectrometry for in situ surface and interface structure, multibeam wafer curvature for strain, and Auger electron spectroscopy for surface composition.

KMAP X-ray Diffractometer

Based on double crystal x-ray diffractometry in combination with position sensitive x-ray detection, our KMAP x-ray diffraction analysis is used to determine the lattice constant, strain relaxation, composition, layer orientation, and mosaic spread for a large variety of advanced epitaxial semiconductor material systems.

Nanoelectronics Laboratory

We have the capabilities for fabrication of nanoscale quantum device structures, together with capabilities for ultra-low-noise measurement of transport from 0.3 Kelvin to ambient at high magnetic fields.

Lasers and Optics

We provide characterization and advanced understanding in the area of solid-state lasers and non-linear optics, especially as coherent sources of broadly tunable light in rugged, compact geometries. We also have established expertise in long-term and transient radiation effects characterization of optical materials. Capabilities include the widely used (approximately 2000 users worldwide) SNLO (Sandia Non-Linear Optics) code, which is a lab-tested code for predicting the performance of non-linear optical components. In the area of integrated optical materials, our laboratories produce new types of photosensitive materials

(processing patent applied for) for directly-writeable waveguides and reconfigurable optical interconnects.

Laser and Optical Spectroscopies

Our capabilities in characterizing semiconductor materials by photoluminescence and magnetoluminescence extend down to low temperatures by optical laser imaging and laser microscopy, by laser excitation spectroscopy, and by the time-resolved measurements of optical emission. We also have developed a high lateral resolution, near-field scanning optical microscopy (NSOM) capability with time and frequency resolution.

Low-Temperature Plasma Analysis

We have state-of-the-art capabilities for the analysis of low-temperature plasmas as found in commercial processing reactors. These include emission spectroscopy, electrical characterization, laser and microwave-based measurements of species concentrations, in situ electric field measurements, and others. Sandia is the only lab that combines new diagnostics, relevant process chemistries (complex mixtures), and massively parallel (MP) computer models for simulation of continuous and transient plasmas.

— Synthesis and Processing —

Synthetic Organic Laboratory

Novel lipids, surfactants, and other small molecules are prepared in this laboratory via synthetic organic techniques. The laboratory is also capable or forming and characterizing self-organized structures (e.g., liposomes, micelles, self-assembled monolayers, LB films) generated with the newly synthesized molecules in pure or mixed molecular systems.

Biomaterials Laboratory

The Biomaterials Laboratory possesses equipment to perform numerous molecular biology and biochemistry research including genomic DNA, RNA, and plasmid isolation from a variety of sources (e.g., bacteria, viruses, and eukaryotic tissues and ells). DNA sequences can be cloned into a variety of organisms, permitting the manipulation and modification of DNA and protein sequences, structure, and function. Cloned DNA sequences can be genetically engineered using reverse transcription, the polymerase chain reaction and site-directed mutagenesis. Native and recombinant proteins also can be expressed, purified, characterized, and functionalized in this laboratory.

Monolayer Deposition of Organic Films

We have a Langmuir-Blodgett facility for controlled deposition of mono- and multi-layer organic films. The facility includes two computer-controlled troughs, in situ fluorescence microscopy, vibration isolation, and a dust-free down flow work area.

Nanocluster Laboratory

We have developed and patented a process based on the use of inverse micelles for the synthesis of large quantities of monodisperse clusters of metals, semiconductors, and oxides.

Electron Cyclotron Resonance (ECR)

This plasma facility has been built for studying fundamental processes governing the growth of oxide and nitride dielectric films used in optoelectronics and used as hard coatings. This is the only system in the U.S., which combines ECR plus e-beam evaporation.

Molecular Beam Epitaxy (MBE)

We have research semiconductor growth laboratories for ultra-pure and ultra-flexible MBE growth of III-V materials. In addition, we have research systems for Group IV semiconductor growth.

Metal-Organic Chemical Vapor Deposition (MOCVD)

We maintain research facilities with capabilities in MOCVD of III-V compound semiconductor materials including GaN-based materials and self-assembled quantum dots. These capabilities include research reactors designed specifically for studies of CVD chemistry, fluid dynamics, the development of advanced in situ diagnostics, and the development of advanced semiconductor heterostructures and devices.

Crystal and Thin Film Growth

Capabilities in this area include pulsed laser deposition chambers, a high vacuum metal deposition chamber, a thin film oxide deposition chamber, a diamond-like carbon deposition chamber, a hot filament chemical vapor deposition chamber, and various apparatus for single crystal growth. Our capabilities for stress relief of diamond-like carbon films and structures produced by pulsed laser deposition are not available elsewhere.

400 kV and 180 keV Ion Implanters

These systems are equipped with a variety of sources (gas, sputter, and metal vapor). This facility provides ion species from hydrogen to bismuth that can be used for studying fundamental irradiation mechanisms and selective chemical doping in semiconductors, metals, ferroelectrics, and superconductors.

High Pressure and Shock Wave Physics and Chemistry Laboratories

Our capabilities in this area include large volume static high pressure apparatus which can be operated at temperatures ranging from 2 to 700 K and in magnetic fields, as well as gas gun and explosive loading facilities with state-of-the-art, time-resolved diagnostics. Recovery fixtures have been developed for use with the gas gun and explosive shock loading facilities that allow unique material synthesis over broad ranges of shock pressures and temperatures.

Soft Nanolithography

Soft nanolithography refers to patterning techniques that complement UV and electron beam lithography. These approaches avoid the chemical and radiation exposure often used in conventional lithography processing, making soft nanolithography particularly useful for bio, organic, and molecular materials. Current capabilities include micro-contact printing, nanotransfer printing, and dip-pen nanolithography.

— Theory and Simulation —

Electronic Structure and Linear Scaling

We have developed state-of-the-art massively parallel electronic structure algorithms, based on ab initio pseudopotentials and plane-wave/Gaussian basis functions. These codes are used to develop a fundamental understanding of physical phenomena and materials, including compound semiconductor band structure, diffusion of point defects, dopants and impurities, optoelectronic properties of extended defects, adsorbate interactions on surfaces, bonding at metal-oxide interfaces, and enhanced reactivity of nanoparticles. To allow the investigation of more complex systems and phenomena, we have developed new computationally efficient algorithms, e.g., self-consistent linear scaling density functional theory and variable and real-space gridding.

Molecular Dynamics Simulation

Large scale, classical molecular dynamics simulations using the massively-parallel code LAMMPS (Large-scale Atomic/Molecular Massively Parallel Simulator) are being used to model a wide variety of systems. These classical simulations cover the length and time scale intermediate between quantum and continuum calculations. Systems of current interest include adhesion and friction in self-assembled monolayers, degradation of

polymer adhesives, wetting and spreading of multi-component fluids and transport in polymer membranes for fuel cells. Modifi- cations of the algorithm to include particle rotation and friction have been implemented to study granular materials.

Chemical Processes

We have extensive capabilities, including massively-parallel computation, to model complex chemically reacting flows such as occur in chemical vapor deposition manufacturing processes. Our numerical simulations can include the coupled gas-phase and gas-surface chemistry, fluid dynamics, heat, and mass transfer to provide predictive models of a chemical process.

Low-Temperature Plasmas

We have extensive capabilities in massively parallel codes to simulate the time and space evolution of low-temperature plasmas, focusing on new theoretical techniques for achieving rapid convergence and on direct comparisons with experimental results.

Optical and Wave Propagation

We have developed advanced simulation codes for understanding wave propagation in optical parametric oscillators and amplifiers for the purpose of designing highly efficient, tunable laser sources. We also have capabilities in novel optical designs, including resonators for compact laser geometries. These capabilities are coupled to in-house micro-optics construction facilities and state-of-the-art optics testing.

Physical, Chemical, & Biomolecular Sciences Center - FY04 Budget

Physical, Chemical, & Biomolecular Sciences Center FY04 Budget - By Customer

Capital ($1.6M)

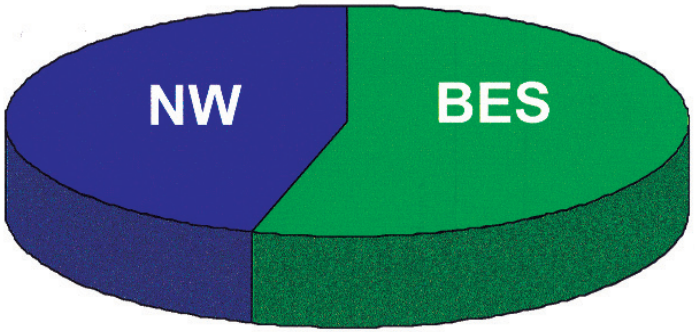

Operating ($36.9M)

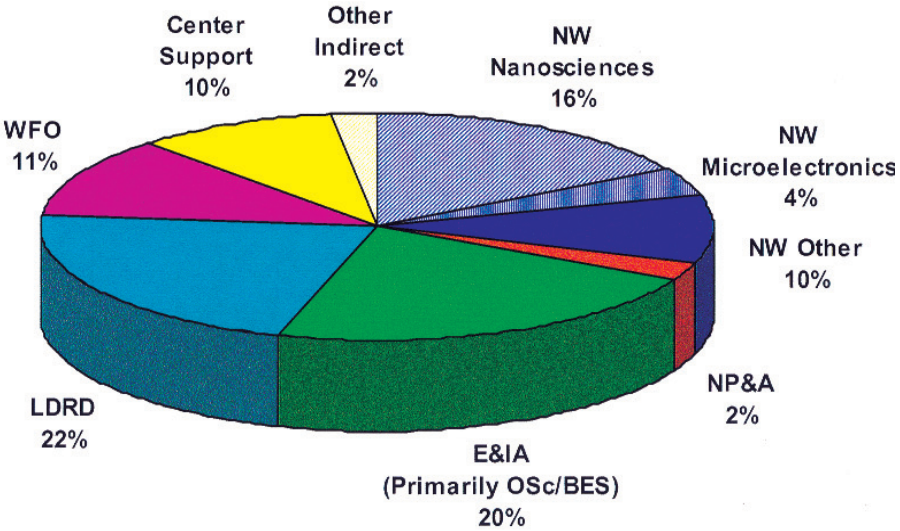

NW	Nuclear Weapons	NP&A	Nonproliferation & Assessments	E&IA	Energy & Infrastructure Assurance	OSc	Office of Science
BES	Basic Energy Sciences	LDRD	Laboratory Directed Research & Development	WFO	Work for Others		

SAND2004-5969P: *Research Briefs* for the Physical, Chemical, & Biomolecular Sciences Center is published by Sandia National Laboratories, a multiprogram laboratory operated by Sandia Corporation, a Lockheed Martin Company, for the United States National Nuclear Security Administration and the Department of Energy under Contract DE-AC04-94AL85000.

Printed 2004